

A review of RANS modeling for hypersonic large cone-flares

Jimmy-John O.E. Hoste,¹ Nick Gibbons,² Tobias Ecker,³ Chiara Amato,³ Doyle Knight,⁴ Artemii Sattarov,⁵ Olivier Thiry,⁵ Jean-Pierre Hickey,⁶ Fahri Erinc Hizir,⁷ Tolga Köktürk,⁷ Neil Castelino,⁸ Valerio Viti,⁸ Megan A. Roldan,⁹ Steven Qiang,⁹ James G. Coder,⁹ Robert A. Baurle,¹⁰ and Jeffery A. White¹¹

¹⁾Independent Researcher, currently Destinus SA, Switzerland

²⁾University of Queensland, Australia

³⁾DLR Göttingen, Germany

⁴⁾Rutgers - The State University of New Jersey, USA

⁵⁾Cadence Design Systems, Belgium

⁶⁾University of Waterloo, Canada

⁷⁾ASELSAN, Turkey

⁸⁾ANSYS Inc., USA

⁹⁾The Pennsylvania State University, USA

¹⁰⁾AFRL USAF, USA

¹¹⁾NASA Langley, USA

(Dated: 19 October 2024)

This work assesses the status of RANS' predictive capability for axi-symmetric hypersonic geometries. An in-depth literature review on the topic is provided including relevant developments in the field of RANS for these type of setups. Furthermore, as part of the AVT-352 on hypersonic turbulence, a code-to-code comparison on two large-cone flare geometries, experimentally studied at CUBRC, has been performed in order to evaluate the variability in predictions for freestream Mach numbers ranging between 5 and 13 at low enthalpy conditions. The nature of the physics found in cone-flare geometries is known to be extremely challenging for RANS CFD codes, a fact that is confirmed in this work.

I. INTRODUCTION

In order to advance the fundamental understanding of hypersonic flows, diverse experimental setups have been devised since the late 1950's¹. The experiments aimed at isolating effects occurring on actual hypersonic vehicles and provide data to assess, validate, and further develop empirical correlation as well as numerical tools (CFD). An important focus of these experiments has been on shock-wave boundary-layer interactions (SWBLIs), both in laminar^{2–4} and turbulent conditions^{5–7}. Such interactions are typically found in control surface deflections, flared junctions, or intakes and require careful considerations in aerothermal design. A hypersonic vehicle, such as the National Aerospace Plane (NASP), is expected to encounter turbulent boundary layers in its flight path, as illustrated in Figure 1 of⁸. Specifically in the context of NASP, a set of experimental setups for shock wave turbulent boundary layer interactions (SWTBLI) was identified^{9,10} in order to guide the development of turbulence modelling for CFD. An inventory of SWTBLI experiments as of 1994 was given by Settles and Dodson^{8,11}. The authors assessed the quality of existing datasets that would allow for improvements in turbulence modelling. Among the setups, there was an axisymmetric cylinder-flare which was introduced by Holden et al.^{6,7}. The motivation for a cone/flare type axisymmetric configuration resulted from the desire to understand the complexity of SWTBLI's without possible endwall effects observed in nominally two-dimensional planar SWTBLI⁶. These early experiments were performed at Calspan's shock tunnel facilities, now commonly known as CUBRC facilities. Since then, many sets of experimental data on cone/flare interactions have been collected, including some more recent works performed in the last two decades^{12–15}. Moreover, Marvin *et al.*¹⁶ provided a comprehensive experimental database for SWBLIs

that includes baseline CFD solutions for the various test cases compiled. More recently, a comprehensive survey of SWTBLI experiments, Direct Numerical Simulation (DNS) and Large Eddy Simulation (LES) as of 2023 was presented in Knight and Kianvashrad¹⁷.

SWBLIs have been the go-to type of test cases for validation of hypersonic CFD codes, driven by the desire to leverage numerical predictive capability in hypersonic vehicle design. In turbulent conditions, Reynolds-Averaged Navier-Stokes (RANS) modelling has always been the primary method of choice for engineering design. Anno 2024 this fact has (unfortunately) not changed, as the more accurate scale-resolving methods still remain out of reach for such purposes. Moreover, the availability of computational power at an affordable cost, as well as the advent of open-source CFD codes, allows any researcher to run (RANS) CFD test cases and obtain solutions in a relatively short time frame. It is therefore more important than ever to focus on uncertainties in numerical predictions which can emanate from a CFD solver (numerical discretization and models) or its user (setup, meshing, modelling constant choices). The above advancements have translated into an increase in CFD usage in general vehicle design. Furthermore, this growing role, understood by academia, research centres and industry, has led to the compilation of the CFD Vision 2030 Roadmap, contracted by NASA¹⁸. The roadmap intended to identify current (as of 2014) shortcomings and bottlenecks of CFD and provide strategic key points to guide the path forward. This also includes CFD-related topics such as meshing, multi-disciplinary design optimization (MDO), and the rapidly evolving hardware architecture of computers and High Performance Computing (HPC). From a physics point of view, accurate turbulence modelling has been identified as a large shortcoming of CFD, a topic that is also very

relevant in supersonic and hypersonic environments. In 2024, Morton and Cummings¹⁹ issued a hypersonic grand challenge linked to the CFD vision 2030 aiming at pushing forward all modelling aspects relevant to such vehicles. Relevant to the latter, in (turbulent) hypersonic CFD, wide prediction uncertainties have typically been encountered for SWBLI physics. This entails separation location, evolution of wall pressure, skin friction or heat flux including peak values. The latter set of quantities are key in the aero-thermal and -structural design of vehicles in the hypersonic regime and remain a challenge for RANS models as is made clear in the following paragraph introducing previous work related to the topic.

Knight and Degrez²⁰ reported in the late 1990s on a set of comparative CFD simulations performed by different participants on SWBLI setups; single and double fins as well as hollow cylinder-flares. Twelve of the thirteen cases were turbulent and received contributions from participants with various turbulence models ranging from zero-dimensional (Baldwin-Lomax) to full Reynolds stress models. Other turbulence models included Spalart-Allmaras-Edwards and among the two-equation models a set of $k-\epsilon$ types and one $k-\omega$. A clear scatter in the predictions was shown with discrepancies from experimental measurements depending on the type of interaction, i.e. three-dimensional vs. nominally two-dimensional. Moss *et al.*²¹ and Gnoffo²² numerically predicted hollow cylinder/flare and sharp double-cone geometries at high freestream Mach numbers (> 9.5) in laminar conditions and with some level of thermal non-equilibrium depending on the experimental conditions. Gnoffo²² observed an increase in separation extent with increased Reynolds number but a limited influence of the Mach number. The sharp double-cone setup, at the selected conditions, demonstrated to be more challenging from a numerical settings perspective, which is linked to the strong shock interaction. Other noteworthy points of interest include gas modelling effect (perfect gas, thermal-equilibrium and non-equilibrium) as well as flow-unsteadiness linked to numerical settings. Moreover, both Moss *et al.*²¹ and Gnoffo²² indicate a strong sensitivity to computational grids which is also valid for turbulent setups (see also²⁰). Bedarev *et al.*²³ studied a Mach 6 sharp cone-flare geometry numerically and experimentally in laminar conditions. Specific interest is the transitional state from laminar to turbulent, which occurs on re-entry type vehicles (e.g. NASP or Hermes) and was studied numerically by defining a laminar zone and a turbulent zone. In 2002, Candler *et al.*²⁴ studied the impact of nozzle flow non-equilibrium of the nitrogen test gas on the computational predictions of laminar hypersonic sharp double-cone and hollow cylinder/flare flows. Vibrational non-equilibrium effects were able to explain some of the previous discrepancies in CFD predictions but not for all cases considered. The authors emphasize the complexity of experimental studies in hypersonic conditions, where a multitude of effects occur concomitantly, which must be kept in mind when used for CFD validation. In 2006, Holden¹ presented a review on hypersonic SWBLI studies aimed at numerical validation as well as developing empirical and analyt-

ical models. It is made clear that the rapidly evolving computational capabilities (CFD) will be key in advancing the design capabilities of the highly multi-physics problems encountered in SWBLIs.

In the same year, Roy and Blottner²⁵ published a review describing turbulence modelling activities on experimental validation test cases in the context of hypersonic SWTBLI. One of the motivations was to build up on the work of Settles and Dodson^{8,11} and provide an update on test cases as well as CFD modelling practices. They limited their focus to one- and two-equation RANS turbulence models adopted to study the described set of experimental setups, of 2D and axi-symmetric nature, without the use of wall functions whose applicability are highly debatable in hypersonic separated flows. An important advice by the authors is that the development of turbulence models based on hypersonic flow conditions should also be tested on incompressible flows to validate their generalizability. Eighteen different turbulence models, applied in the literature, are assessed in this review by the authors which contains most of the still commonly adopted models except for the latest version of the Wilcox' $k-\omega$ model²⁶. Based on the seven selected experimental test cases, it is observed that only a limited number of these models have been applied to all of them, and the discussion will focus on these. The widely used Menter's $k-\omega$ SST model was not part of this, as it had only been used on three of the experiments. The general conclusions were a poor predictive capability for heat fluxes and mixed results in terms of wall pressures. No detailed comment on skin friction coefficients could be given as most of the experiments did not measure such important information. The authors advocate for newly, carefully performed experimental campaigns with a more extensive set of data including fluctuating properties. From the RANS modelling point of view, a lot of work still needs to be done and aspects such as compressibility, turbulent Prandtl number variations and shock unsteadiness need to be looked at in more detail.

Holden²⁷ and Holden *et al.*¹² revised the experimental activities on hypersonic geometries in the LENS facilities of CUBRC which can be used for CFD code-to-code validation purposes. Various CFD predictions are also shown. Holden²⁷ focuses more on the low-density high Mach type of configurations which do not require turbulence modelling. Holden *et al.*¹² is concerned with the turbulent aspects with, among others, the HIFiRE 1 flight configuration setup which was tested in the LENS facilities. The authors observe that tuning a turbulence model for one configuration does not guarantee its successful application to other setups. A new set of experimental data on hypersonic large cone / flare and hollow cylinder / flare configurations are mentioned, specifically tailored for turbulence model validation. These results are discussed in further detail in^{13,14}.

In 2012, Knight *et al.*²⁸ presented the results of a large effort in simulating laminar hypersonic SWBLI configurations (a double cone and a cylinder) with thermo-chemical non-equilibrium models. In 2015, Candler²⁹ presented another overview of the status of CFD for hypersonic flows. This entails the results of predictions on the double cone, hollow cylinder / flare as well as large cone-flare setups deviced for

blind code validation^{13,14}. The blind code-to-code validation demonstrated that CFD results tend to be closer to one - another than with experimental data. Moreover, the numerical settings and models were very similar, i.e. there is a lack of variety. The role of DNS in providing a basis for turbulence modelling improvement in such SWBLI's is also mentioned. A large part of the discussion is then focused on what could be improved in terms of physical modelling and numerical modelling, including the turbulence modelling specific to hypersonic flows with cold walls and supersonic internal flows encountered in hypersonic propulsion flow paths. In 2017, Knight *et al.*³⁰ presented another code-to-code comparison on a double wedge setup at two different total enthalpies and gas compositions. The majority of the partners considered thermo-chemical non-equilibrium models to tackle the setup at the highest total enthalpy (8 MJ/kg). Differences between predictions and experiments were observed when an unsteady approach was adopted, leading to a recommendation for a more accurate description of tunnel start-up transience. Furthermore, discrepancies between 2D and 3D simulations invite future work to consider full 3D setups for nominally 2D geometries. More recent simulation work on SW(T)BLIS have been discussed in^{31–35} as well as some experimental work^{15,36}. A general observation is the limited usage of commercial CFD software in such hypersonic validation cases, or code-to-code comparison campaigns (GASP in²⁸, GASPEx in^{30–33} and StarCCM+ in³⁵). However, commercial codes are expected to play an important role in enabling a wider industrial community to perform hypersonic design tasks. This has become apparent in their development over the last years.

Hypersonic cone/flare, hollow cylinder/flare and double-cone configurations have been popular for RANS code validations, as exemplified by^{22,23,32,34,35,37–39}. The interest varies from chemical and thermal non-equilibrium flow physics to laminar, transitional or fully turbulent flows. Such test cases have also been popular in blind validation of CFD codes^{24,27–30}. These have typically been performed within the context of NATO Science and Technology Organization (STO) Applied Vehicle Technology (AVT) working groups^{30,40}. The present work emanates similarly from a NATO AVT group, the AVT-352 on hypersonic turbulence. Given the topic of interest, a RANS code-to-code validation has been initiated on hypersonic turbulent cone-flare geometries gathering a wide variation of participants and CFD solvers. The turbulence models considered in this work include one-equation types (Spalart-Allmaras), two-equation types ($k-\omega$ families), explicit algebraic Reynolds Stress Models (EARSM), as well as full Reynolds Stress Models (RSM).

This work is structured as follows. Section II covers the geometries and flow conditions selected for the code-to-code comparison, including a description of the typical cone-flare physics. Section III discusses the previous CFD literature on the currently selected setups as well as the wider RANS modelling evolution and challenges for the physics currently en-

countered. The simulation strategy from the participants are detailed in Section IV and the results are compared in Section V. Finally, conclusions and future work are discussed in Section VI.

II. PROBLEM DESCRIPTION

Two hypersonic turbulent cone-flare geometries, with experimental campaigns carried out under various conditions, have been selected for code-to-code comparative studies amongst the participants. A first setup (Subsection II B) was experimentally studied at Mach 11 and 13 while the second setup (Subsection II C) at Mach numbers between 5 and 8, both with air as the working fluid. Both sets of experimental data have been obtained in the LENS' hypersonic facilities at CUBRC (reflected shock tunnels)^{12,13,16}. The geometries and flow conditions have specifically been tailored in order to ensure a turbulent boundary layer forms prior to the cone-flare junction, which is the main area of interest. For case 2, this rapid transition from laminar to turbulent state is demonstrated by the experimental heat flux traces provided by CUBRC. This fact, together with the simplicity of the setup for CFD validation purposes, has been the major motivation for selecting these geometries.

In a first Subsection II A, the physics encountered in cone-flare like configurations are introduced, followed by a description of the two test cases in Subsections II B and II C, respectively.

A. Cone-flare related physics

The overall flowfield structure for a typical cone-flare configuration is shown in Figure 1 for CUBRC Run 28 at Mach 4.96⁴¹. The forward cone half-angle is 7° and the aft flare angle is 40°. The streamlines are deflected by the attached incident conical shock⁴². A bow shock is generated by the flare followed by a rapid expansion around the corner formed by the flare-cylinder junction. The incident shock-bow shock interaction occurs further downstream.

Details of the flowfield structure in the vicinity of the cone-flare junction are illustrated in Figure 2 for CUBRC Run 28 at Mach 4.96⁴¹. The adverse pressure gradient due to the bow shock causes separation of the boundary layer on the cone surface and the formation of a separation region and shear layer. The deflection of the cone turbulent boundary layer by the separation streamline results in a separation shock which intersects the bow shock forming a triple point and transmitted shock. The surface pressure rises upstream of the separation point, reaches a plateau within the separation region, and rises again near the reattachment. The surface skin friction vanishes at the separation point, reverses direction within the separation region, and rises rapidly downstream of reattachment. Similarly, the surface heat transfer decreases within the

separation region compared to the undisturbed boundary layer upstream, and rises rapidly immediately after reattachment.

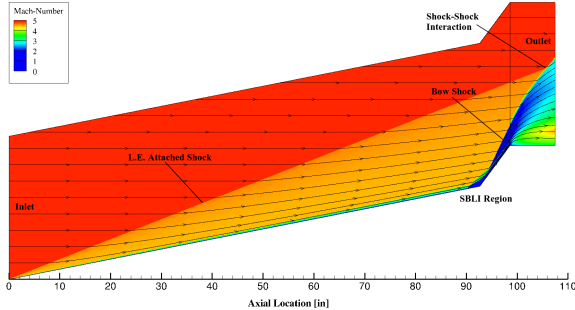


FIG. 1: Overall flowfield structure on large-cone flares for CUBRC Run 28

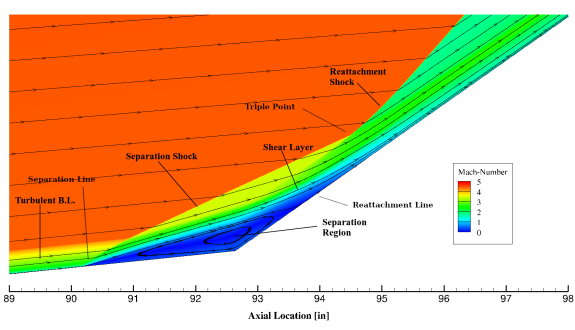


FIG. 2: Details of flowfield structure on large-cone flares for CUBRC Run 28

B. Case 1: 6/42 Degree Cone-Flare at Mach 11 to 13

The first test case is a 6/42 degree large cone-flare as shown in Figure 3 and documented in^{12–14,16}. The flow conditions for two runs have been selected and listed in Table I. The experimental data for Run 4 are tabulated in the following references^{12,13,16}. As mentioned by Marvin *et al.*¹⁶, it must be noted that the tabulated x-coordinate is a distance taken along the surface of the first ramp, at an angle of 6 degrees. In the present work, the x-coordinate represents the axial location and the experimental data are transformed accordingly. Experimental accuracy on pressure and heat transfer measurements of $\pm 3\%$ and $\pm 5\%$, respectively are reported in¹⁶. For Run 6, the experimental information can be found in¹¹.

Free-stream total enthalpies are 1.46 MJ/kg and 2.02 MJ/kg for runs 4 and 6, respectively.

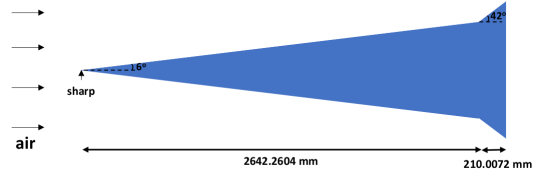


FIG. 3: Cone-flare geometry used for conditions summarized in Table I

Run number	Mach	ρ_∞ (kg/m ³)	T_∞ (K)	u_∞ (m/s)	p_∞ (Pa)	T_{wall} (K)
Run 4	11	0.03235	67	1807	626	300
Run 6	13.1	0.03095	57	1968	506	300

TABLE I: Flow conditions of Run 4¹⁶ and Run 6¹¹.

C. Case 2: 7/40 Degree Cone-Flare at Mach 5 to 8

The second test case is a 7/40 degree large cone-flare as shown in Figure 4 and was part of a newer campaign for blind code validation¹². The presently selected conditions of interest are runs with dry air, summarized in Table II. Some of the experimental data has been presented in^{13,14} and is publicly available from the CUBRC website⁴². The length of the cone was devised to ensure that the transition occurs very close to the tip with transition locations reported by Holden *et al.*¹³ (Table 22). Free-stream total enthalpies vary between 0.21 and 2.11 MJ/kg in ascending order for Runs 33, 14, 37, 28, 34, 45, 41.

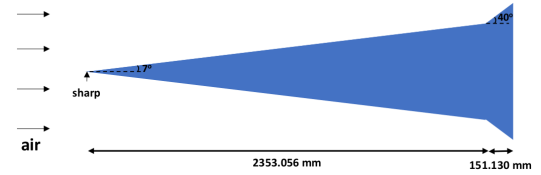


FIG. 4: Cone-flare geometry used for conditions summarized in Table II

Run number	Mach	ρ_∞ (kg/m ³)	T_∞ (K)	u_∞ (m/s)	p_∞ (Pa)	T_{wall} (K)
45	5.90	0.11132	244	1852	7808	300
28	4.96	0.14173	220	1477	8944	300
34	6.03	0.07112	170	1578	3468	300
33	6.17	0.07370	57	931	1195	300
14	7.18	0.05721	67	1177	1094	300
41	8.10	0.02355	167	2103	1128	300
37	8.21	0.04370	60	1282	758	300

TABLE II: Flow conditions for 7 / 40 cone-flare^{13,33}.

Case	Run #	Participant	CFD solver	Turbulence model
6/42	4	Hizir, Köktürk	Ansys Fluent	k- ω SST*, Spalart-Allmaras*
		Hoste	STAR-CCM+	k- ω SST
		Gibbons	Eilmer	k- ω 2006 klim-V
		Roldan,Qiang,Coder	OVERFLOW	k- ω SST
		Hickey	SU2	k- ω SST
		White, Baurle	VULCAN	Spalart-Allmaras, k- ω SST
		Sattarov, Thiry	Cadence	k- ω SST, EARSM
		Hizir, Köktürk	Ansys Fluent	k- ω SST
		Gibbons	Eilmer	k- ω 2006 klim-V
		Sattarov, Thiry	Cadence	k- ω SST, EARSM
7/40	45	Hoste	STAR-CCM+	k- ω SST
		Sattarov, Thiry	Cadence	k- ω SST, EARSM
		Hizir, Köktürk	Ansys Fluent	k- ω SST
		Gibbons	Eilmer	k- ω 2006 klim-V
		Ecker	TAU	EARSM, RSM, Spalart-Allmaras, k- ω
		Amato	HyperCoda	Spalart-Allmaras
		Castelino, Viti	Ansys Fluent	GEKO
		Roldan,Qiang,Coder	OVERFLOW	k- ω SST
		Hickey	SU2	k- ω SST
		White, Baurle	VULCAN	Spalart-Allmaras, k- ω SST
		Hoste	STAR-CCM+	k- ω SST
		Knight, Alviani	GASPEx	k- ω 2006
		Gibbons	Eilmer	k- ω 2006 klim-V
28	Hizir, Köktürk	Ansys Fluent	k- ω SST*	
		Hickey	SU2	k- ω SST
		Hoste	STAR-CCM+	k- ω SST
		Knight, Alviani	GASPEx	k- ω 2006
34	Gibbons	Eilmer	k- ω 2006 klim-V	
		Hickey	SU2	k- ω SST
		Hoste	STAR-CCM+	k- ω SST
		Knight, Alviani	GASPEx	k- ω 2006
33	Gibbons	Eilmer	k- ω 2006 klim-V	
		Hickey	SU2	k- ω SST
		Hoste	STAR-CCM+	k- ω SST
		Knight, Alviani	GASPEx	k- ω 2006
14	Gibbons	Eilmer	k- ω 2006 klim-V	
		Hickey	SU2	k- ω SST
		Hoste	STAR-CCM+	k- ω SST
		Knight, Alviani	GASPEx	k- ω 2006
41	Gibbons	Eilmer	k- ω 2006 klim-V	
		Hickey	SU2	k- ω SST
		Hoste	STAR-CCM+	k- ω SST
		Castelino, Viti	Ansys Fluent	GEKO
37	Knight, Alviani	Eilmer	k- ω 2006 klim-V	
		Hoste	STAR-CCM+	k- ω SST
		Gibbons	GASPEx	k- ω 2006
		Gibbons	Eilmer	k- ω 2006 klim-V

*Results obtained in thermal equilibrium and non-equilibrium.

TABLE III: Overview of participants. Please refer to Section IV for further details regarding variations of the selected turbulence models.

D. Participants and Run Information

Table III provides a summary of the cases ran by the different participants, as well as the CFD codes and selected turbulence models. Section IV will provide further details about the strategy followed by each of the participants including information about the applied turbulence model (version, modeling constants).

III. PREVIOUS WORK AND CHALLENGES FOR RANS

This section discusses previous attempts to simulate the setups described in Section II (see III A) as well as other relevant cases (see III B) where various RANS models have been adopted for predictive purposes. Finally, some RANS-related developments specific to the physics encountered here are discussed in III C.

A. Hypersonic turbulent large cone-flare studies

Previous CFD work related to the geometries described in II B and II C is covered in this subsection.

1. 6/42 large cone-flare

Horstmann^{25,43} performed numerical validations on various hypersonic geometries, including the Mach 11 cone-flare case (Run 4). Various formulations of the k- ϵ model were used and behaved similarly in terms of wall pressure predictions. However, large discrepancies in heat flux predictions between the models, as well as with the experiments, were observed.

Holden et al.^{12,13} reports pressure and heat flux CFD data obtained with the DPLR code^{44,45} for Run 4 of Table I. Simulations were performed with the k- ω SST (1994)⁴⁶ and an empirical shear-stress limiter coefficient (C_{lim}) following⁴⁷. An optimal value for this coefficient of 0.9 was first found on the HiFIRE 1 (cone-cylinder-flare) setup and subsequently applied to Run 4. Separation onset was over-predicted by the model (CFD x ≈ 86 inches, experiment x ≈ 102 inches). The predicted peak heat flux and pressure values are similar to the experimental measurements, but their location further downstream.

Marvin et al.¹⁶ reviewed a set of experimental setups relevant for SWTBLLI CFD predictions. They provide a baseline CFD solution obtained with LAURA^{48,49} for Run 4 (see Table I) of the 6/42 cone-flare geometry. This baseline prediction is obtained with the Wilcox' k- ω 2006 model and a compressibility correction with $M_{\infty}=0.5$. It predicts very closely the onset of separation as seen by the pressure trace (CFD x ≈ 101 inches, experiment x ≈ 102 inches) as well as pre- and post-interaction heat flux and pressure values. Peak pressure and heat flux locations are accurately predicted, however, peak values are over-predicted. The baseline result follows from an extensive comparison between the turbulence models by Gnoffo et al.⁵⁰. Their work was motivated by NASA's Fundamental Aero Program (FAP) and aimed at reducing uncertainties in predictions of hypersonic flows by 50 %. Run 4 was used to compare multiple turbulence modelling approaches, adopting a calorically perfect gas model for air and relying on Sutherland's law for the molecular properties. The applied turbulence models were Cebeci-Smith, Baldwin-Lomax, Spalart-Allmaras, Menter's SST and the k- ω 2006. In general, the authors observed a strong grid sensitivity of the results. Specific study of the compressibility correction's impact on the k- ω 2006 model is reported with results demonstrating

separation or not depending on its value. The $k-\omega$ 2006 model with $M_{\infty}=0.5$ prove to be the best overall choice for this setup, as aforementioned.

More recently, Cross and West³⁵ used the commercial software STAR-CCM+ to simulate the 6/42 cone-flare geometry for the Run 4 conditions with a structured grid. Menter's SST, Wilcox' $k-\omega$ 2006, Spalart-Allmaras and Realizable $k-\epsilon$ model were considered with strong variations in heat flux and pressure along the wall, including separation onset. A real-gas model in thermochemical equilibrium, implemented inside the solver is applied to represent the air. In a subsequent attempt, many variations of turbulence model parameters were explored, including the compressibility correction, the a_1 constant for the SST model (see also⁵¹) and the use of a quadratic constitutive relation (QCR, see Spalart⁵²). A beneficial combination appears to be the omission of the first, adapting the second parameter to 0.355 and to activate the QCR. This resulted in a separation onset predicted at $x \approx 100.4$ inches (experiment $x \approx 102$ inches).

2. 7/40 large cone-flare

This second geometry was originally considered as part of a blind code-to-code validation as explained by Holden^{13,14}. Candler²⁹ assessed the state-of-the-art in CFD for hypersonic flows. In this discussion, results for the aforementioned blind code-to-code validation at Run 45 conditions are presented. Strong variations in predictions, as expected, are observed. Results with Spalart-Allmaras (LAURA) and SST from various codes (GASP, DPLR, US3D) are shown. In addition to uncertainties due to grids and numerical methods which have to be assessed to some extent, Candler points out the need for experimental uncertainty quantification which could be achieved by using the same geometry in multiple experimental facilities.

Holden *et al.*⁵³ briefly discusses additional results from the blind code-to-code validation for Run 28. In addition, the impact of wall temperatures is presented by comparing Run 33 and Run 45 results. Unfortunately, the graphs are of very low quality, making them difficult to read.

In a presentation, published on the CUBRC website, Wadham *et al.*⁵⁴ presents results for Runs 28, 33, 45, 37 and 41 of Table II with the US CFD codes DPLR, FUN3D, US3D, GASP and LAURA. Most of the submissions were obtained with the SST turbulence model. For the two-equation turbulence models, peak pressures and heat fluxes on the flare are located in the vicinity of each other. This observation does not hold for the one-equation turbulence model results. Significant variations in the predictions are observed for the different cases. Furthermore, the two-equation models have a tendency to predict separation onset in spite of experimental measurements indicating no likely incipient separation.

Alviani³³ studied the setup with Wilcox' $k-\omega$ 2006 version, reporting detailed results for run 28, run 34, run 33, run 14, run 41 and run 37. These simulation results will be considered in the present endeavour.

Cross and West³⁵ also considered the 7/40 degree cone-flare

setup (Figure 4) for the conditions of Run 33 and Run 45 in their STAR-CCM+ study. Simulations with both the Spalart-Allmaras and Menter's SST model are presented. For Run 33, the former turbulence model predicts a better separation onset ($x \approx 89.8$ inches, experiment $x \approx 90.5$ inches) as well as post-interaction values. In the separation zone itself, the heat flux is more appropriately predicted by Menter's SST model. Similarly, for the Run 45 comparison, the Spalart-Allmaras model predicts a better separation, but flare heat flux values are underpredicted. Menter's SST overpredicts the flare heat flux values. Moreover, some sensitivity on the gas modelling assumptions is shown by comparing a single-species gas with temperature dependent thermophysical properties, to a build-in thermal non-equilibrium gas model.

Roy *et al.* studied this cone-flare configuration for the conditions of Run 37, Run 33 and Run 14^{55,56}. They coupled the shock-unsteadiness model^{57,58} with Wilcox' $k-\omega$ turbulence model and a variable turbulent Prandtl model which is active in shock regions. General improvements of heat flux predictions on the ramp are illustrated for all cases.

Other results found in the open literature include a presentation from Prabhu⁵⁹ which shows some sample results for Run 37 with DPLR and Menter's SST (ideal gas, Sutherland law, Prandtl = 0.71).

Finally, Ali *et al.*⁶⁰ also simulated this cone-flare configuration for the conditions of Run 33 (dubbed Case-3), Run 14 (dubbed Case-2) and Run 37 (dubbed Case-1) listed in Table II. They used a modified Spalart-Allmaras model which includes shock-unsteadiness (SU) related physics⁵⁸. In comparison to the standard Spalar-Allmaras, the new model demonstrates a general improvement for the pressure traces (separation onset) but heat flux predictions remain challenging.

A summary of the relevant simulation results from the literature for the cases and conditions presented in Subsections II B and II C are listed in Tables IV and V. The results are digitized from graphs and therefore prone to small errors. In some of the cases, no details on the CFD solver can be found, which is denoted with "?". The same is true for the exact details of some of the turbulence models. For Run 6 and Run 34, no information could readily be found in the literature.

Table VI summarizes the absolute variations between the various predictions compiled in Tables IV and V. It is clearly shown that even if variations in separation onset predictions are limited (at least for the 7/40 cone-flare geometry), variations in peak quantities are non-negligible. Relying on predictions would result in strong differences in thermo-structural design of such a geometry in practical applications.

Case	Run #	reference	CFD solver	Turbulence model	Separation onset (cm)	Peak pressure location (cm)	Peak pressure (kPa)	Peak heat flux location (cm)	Peak heat flux (MW/m ²)
6/42	4	12,13	DPLR	k- ω SST 1994 ($C_{lim} = 0.9$)	218.4	284.5	140.96	284.5	2.37
	16		LAURA	Wilcox' k- ω 2006 ($M_{t0} = 0.5$)	256.5	268.4	173.00	268.2	4.73
	35		STAR-CCM+	k- ω SST 2003, $a_1=0.355$, QCR, no compressibility correction	255.0	270.8	158.80	270.7	3.79
6	?								
7/40	45	29,54	US3D	k- ω SST	230.9	240.9	273.20	240.7	4.86
		29,54	DPLR (MacLean)	k- ω SST	233.0	239.1	256.90	238.2	4.34
		29,54	DPLR (Prabhu)	k- ω SST	227.5	242.9	301.97	243.1	4.96
		29,54	GASP	k- ω SST	230.8	240.9	276.98	240.6	5.42*
		29,54	LAURA	Spalart-Allmaras	234.8	238.7	248.58	248.2 ⁺	2.81
		35	STAR-CCM+	k- ω SST 2003, $a_1=0.355$, QCR, no compressibility correction, 1-species air	231.2	240.1	274.52	239.9	5.24
		35	STAR-CCM+	Spalart-Allmaras, 1-species air	235.1	239.8	250.57	243.2	2.98
28	54	54	US3D	k- ω SST	230.4	241.7	206.45	241.4	2.31
		54	DPLR (MacLean)	k- ω SST	232.4	239.4	209.40	238.7	2.29
		54	DPLR (Prabhu)	k- ω SST	230.3	242.7	202.82	241.8	2.24
		54	GASP	k- ω SST	229.4	242.6	210.36	242.1	2.54
		54	LAURA	Spalart-Allmaras	232.4	239.4	196.91	248.8	1.58
34	?								
14	60	?		Spalart-Allmaras	231.7	240.3	63.03	NA	NA
		60	?	Spalart-Allmaras SU	230.0	241.5	68.70	NA	NA
		55,56	?	Wilcox k- ω SU	229.5	239.8	77.96	241.4	0.430
		55,56	?	Wilcox k- ω SU and variable Pr_t	229.5	239.8	77.96	240.2	0.350

TABLE IV: Part 1. Quantities of interest from previous CFD studies of hypersonic turbulent cone-flares for conditions in Tables I and II. Distances taken from the nose of the cone in the axial direction. Values prone to digitization errors. NA = not available.

* not considering spike in heat flux similar to³³ probably linked to a spike in TKE

+ hard to discern exact location but heat flux level correct

Case	Run #	reference	CFD solver	Turbulence model	Separation onset (cm)	Peak pressure location (cm)	Peak pressure (kPa)	Peak heat flux location (cm)	Peak heat flux (MW/m ²)	
7/40	33	54	US3D	k- ω SST	NIP	243.9	52.93	243.7	0.172	
		54	DPLR (MacLean)	k- ω SST	229.9	239.9	46.09	239.6	0.175	
		54	DPLR (Prabhu)	k- ω SST	226.1	243.2	51.73	242.8	0.183	
		54	GASP	k- ω SST	NIP	244.3	52.22	243.7	0.192	
		54	LAURA	Spalart-Allmaras	229.4	241.2	49.21	247.9	0.104	
		35	STAR-CCM+	k- ω SST a ₁ =0.355, no compressibility correction	2003, QCR,	225.1	244.3	53.98	243.7	0.186
		35	STAR-CCM+	Spalart-Allmaras	228.1	241.9	52.92	243.1	0.113	
		60	?	Spalart-Allmaras	229.3	242.7	50.91	NA	NA	
		60	?	Spalart-Allmaras SU	229.8	242.1	50.25	NA	NA	
		55,56	?	Wilcox k- ω SU	229.1	240.8	49.19	240.8	0.170	
		55,56	?	Wilcox k- ω SU and variable Pr _f	229.1	240.8	49.19	240.8	0.135	
41	54	US3D	k- ω SST	228.8	242.0	96.33	241.8	3.00		
		54	DPLR (MacLean)	k- ω SST	232.9	239.0	80.19	238.6	2.40	
		54	DPLR (Prabhu)	k- ω SST	229.4	241.1	94.94	241.1	2.81	
		54	GASP	k- ω SST	230.7	240.3	90.79	240.1	3.42	
		54	LAURA	Spalart-Allmaras	234.8	239.2*	80.41*	242.6	1.42	
37	54	US3D	k- ω SST	226.6	242.7	73.26	242.6	0.787		
		54	DPLR (MacLean)	k- ω SST	231.5*	239.1	63.45	238.7	0.783	
		54	DPLR (Prabhu)	k- ω SST	228.6	240.9	68.96	240.9	0.746	
		54	GASP	k- ω SST	228.3	241.3	70.45	241.1	0.902	
		54	LAURA	Spalart-Allmaras	232.6	238.9	59.98	243.4	0.420	
		60	?	Spalart-Allmaras	234.4	239.6	56.35	241.7	0.539	
		60	?	Spalart-Allmaras SU	230.7	240.8	66.72	246.4	0.608	
		55,56	?	Wilcox k- ω SU	231.1	240.1	61.85	239.9	0.950	
		55,56	?	Wilcox k- ω SU and variable Pr _f	231.1	240.1	61.85	239.9	0.766	

TABLE V: Part 2. Quantities of interest from previous CFD studies of hypersonic turbulent cone-flares for conditions in Tables I and II. Distances taken from the nose of the cone in the axial direction. Values prone to digitization errors. NIP = not in picture, NA = not available.

* Very hard to discern the exact location

Case Run #	Δ onset (cm)	Sep- aration (cm)	Δ pressure location (cm)	Peak pressure (kPa)	Δ heat flux location (cm)	Peak heat flux (MW/m ²)	Δ peak flux (cm)	Peak flux (MW/m ²)
6/42 4	47.1	16.1		32.04	16.3	2.36		
7/40 45	7.6	4.2		53.39	10.0	2.61		
28	3.0	3.3		13.45	10.1	0.96		
14	2.2	1.7		14.93	1.2	0.08		
33	4.8	4.4		7.89	8.3	0.088		
41	6.0	3.0		16.14	4.0	2.0		
37	7.8	3.8		16.91	7.7	0.53		

TABLE VI: Absolute variations in predictions based on data available in the literature.

B. Hypersonic turbulent RANS validation studies

In addition to the cone-flare geometry, discussed above, other canonical flow geometries have been used to validate RANS turbulence models^{11,20,25,61,62}. Roy and Blottner²⁵ categorize seven canonical hypersonic flow setups, some of which have the relevant physical flow features of the cone-flare geometry. The two-dimensional compression corner and the cylinder flare share many of the characteristic features of the cone-flare, namely the pressure gradient and shock-boundary layer interaction. These flow features cause shock-induced flow separation, which is particularly challenging for RANS-based turbulence models. These challenges become even more important when heat flux is considered (see summary of results in²⁵).

The impinging hypersonic shock has the benefit of isolating shock-induced boundary layer separation from the geometry of the flare setups. The experimental setups consist of a shock generator in the freestream above a fully turbulent hypersonic boundary layer. RANS investigations of this setup reveals that the velocity profiles are insensitive to the turbulence models but the eddy viscosity-based models uniformly overpredict the peak thermal loading⁶³. This thermal loading error can be corrected by an anisotropic SST turbulence that accounts for the shock interaction physics⁶⁴.

More closely related to the cone flare is the two-dimensional compression corner. Wagner et al.⁶⁵ conducted a combined experimental and RANS-based numerical study on a heated compression corner with and without gap. The work highlighted the sensitivity of the transition location, and thus the characterization of the boundary layer, on the separation bubble, shock position, and maximum heat loading location.

The cylinder flare at a freestream Mach number of 7.05⁹; this setup shares many of the same features as the conical flare studied herein. The RANS turbulence models studied by Zhang et al.⁶³ show significant variability peak pressure, heat load, and bubble separation size.

Many of RANS-based works rely on classical turbulence models and assumptions from low-speed equilibrium tur-

bulence applications such as Boussinesq approximation or gradient-based molecular and turbulent diffusion models, the applicability of which in hypersonic conditions may be questionable⁶⁶. A number of efforts have been underway to correct RANS models to better account for the particularities of hypersonic flows. Some works have focused on developing strategies to account for variable turbulent Prandtl numbers⁶⁷. The focus on the turbulent Prandtl number is at the heart of the modelling strategy of Roy and Sinha⁶⁸ to improve the heat flux predictions in a compression corner. Other works have focused on the shock-turbulence interaction⁶⁶. Subsection III C discusses trends in hypersonic-specific RANS developments relevant to cone-flare and related setups described above.

C. RANS models and developments applied to hypersonic flows

As pointed out in^{25,29,69} turbulence modelling for compressible flows are adaptations from incompressible modelling by considering Favre averaging. These models are then applied to hypersonic flow studies. Compressibility corrections have been formulated^{25,29,70} targeting various fluid dynamic phenomena. One of the widespread corrections relies on the turbulent Mach number to modify model coefficients in the destruction terms of the $k-\omega$ model⁷⁰. It originates from Sarkar and Zeman's pressure-dilatation compressibility correction originally developed for free-shear flows. Rumsey⁷⁰ demonstrated the influence of the latter correction types on hypersonic boundary layers with significant variations between cold- and hot-wall cases and significant deviations from expected skin-friction and heat flux values. It is unclear whether they should be used or not. Sensitivity studies in hypersonic cone-flare geometries have also demonstrated such corrections to significantly impact the SWBLI behavior^{16,35,50}. Tu et al. studied the effect of multiple compressibility corrections for the Spalart-Allmaras and SST models on two compression corners configurations with 15° and 34° deflection angles at Mach 9.22⁷¹. The addition of the blended Catris's and Shur's compressibility correction is found to significantly improve the prediction of the SA model. Certain improvements in prediction have also been attained by adding Catris's correction to the SST model.

In various references discussed in Subsections III A and III B, a key feature which RANS has difficulty to handle adequately, is the boundary layer recovery after separation. Coackley et al.^{69,72} investigated this issue for two-equation models in two-dimensional flows (flat plates and SWBLI). The baseline models were not able to predict reattachment heat transfer. Corrections to these models were investigated by the authors which involved modifications to algebraic length scale for the turbulent viscosity as well as rapid compression modifications or rapid strain corrections affecting damping functions and modelling constants in the turbulence models, respectively. Improvements could be seen, but no conclusive modelling strategy, valid for all tested cases, could be devised.

Another common feature of RANS modelling for hyper-

sonic flows is the use of a production limiter which effectively limits the ratio of production to destruction terms⁵⁰. It targets specifically shock waves and the occurrence of unrealistically high values of TKE behind a shock. Canonical shock-turbulence interaction studies⁷³ have demonstrated some level of amplification of turbulence when passing through the shock. Actual amplitudes depend strongly on the shock strength, turbulence strength, and the nature of the turbulence itself. An example of unlimited predictions is shown by³³ with the Wilcox' k- ω turbulence model. An anomalous spike has been observed in heat transfer predictions for all the presented hypersonic cone-flare simulations. It has been linked to a strong increase in TKE at the exact same location. The same behavior has also been shown for the GASP predictions in⁵⁴ with Menter's SST model and can probably be related to this limiting.

Another method to deal with TKE amplifications through shock waves is to account for the actual physics governing the interaction. This is what Sinha *et al.*⁵⁷ have done by incorporating shock-unsteadiness into the k- ϵ turbulence model yielding clear improvements. In a subsequent work, Sinha *et al.*⁵⁸ extended the idea to SWBLI and applied it to one- and two-equation turbulence models. They apply the modelling to supersonic compression ramps and observe better prediction of separation onsets. However, post-ramp reattachment are delayed. The shock-unsteadiness (SU) model has not seen a widespread adoption in the hypersonic RANS community. For hypersonic cone-flare test cases, Ali *et al.*⁶⁰ showed some level of improvements by incorporating SU with a Spalart-Allmaras turbulence model. It is worth pointing out that a qualitatively similar effect to the SU model is present in Menter's SST 2003 model⁷⁴. The model limits the turbulent viscosity based on the strain rate and the F2 blending function. As a result, in a shock, where S goes to infinity, the eddy viscosity will tend to zero in regions of the boundary layer where F2 is non-zero. As a result, production of TKE is strongly attenuated.

RANS modelling introduces various constants that have to be specified. Among these constants, the turbulent Prandtl number, introduced by modelling the Reynolds' heat flux term has shown to have some level of impact in predictions of supersonic combustors⁷⁵. Moreover, a constant value of 0.89 is typically assumed, while it should vary spatially. In canonical shock-turbulence interaction, scale-resolving simulations have shown that the turbulent Prandtl number (Pr_t) reduces through a shock wave^{76,77}. Building on this observation, Roy *et al.*⁶⁸ have devised a variable Pr_t which is activated in shock regions through a shock function. They successfully demonstrated improvements in heat flux predictions in shock-generator type SWBLI cases as well as other hypersonic geometries^{55,56} including cone-flare setups. The shock-unsteadiness modified k- ω model with Pr_t following⁵⁶ has been applied by Ali *et al.* to Mach 9.22 2D wedge-compression corner cases revealing a drastic improvement of the heat flux prediction compared to the standard k- ω model⁷⁸. The model validation has been performed for four 2D wedge-compression corner configurations with deflection angles from 15 to 38 degrees at Mach 9.22 as well as for

the cases of Reynolds number variation and wall temperature variation.

Specifically related to Menter's (1994) SST model⁴⁶, Georgiadis and Yoder⁵¹ demonstrate improved separation behavior and experimental agreement for SWTBLI by changing the a_1 constant, used in the turbulence viscosity evaluation, from 0.31 to 0.355. It is pointed by the authors that the recommendation's validity applies to the cases considered in their work (two SWTBLIs and HiFIRE 2) but no generality can be ensured.

Some intrinsicalities of the present SWTBLI can't be represented through linear eddy viscosity models. Instead, non-linear eddy viscosity models (NLEV), explicit algebraic Reynolds Stress Models (EARSM) or full Reynolds Stress Models (RSM) are required to account for the dominating anisotropies. This was already pointed out by Baurle⁷⁵ in an overview on the modelling for hypersonic propulsion flow paths in 2004. In recent years, some work^{64,79-81} has explored this area. Vemula and Sinha⁷⁹ explored three existing RSM to simulate the canonical homogeneous STI problem⁷³. In general, the post-shock amplifications in the non-stream-wise directions were poorly captured by the models when compared to the DNS data. They then modified the Gerolymos *et al.*⁸² model by introducing SU damping from⁵⁷. This new model was able to correctly capture the canonical STI amplifications (for solenoidal incoming turbulence) for shock Mach numbers up to 6. Post-shock turbulence decay also showed improvements with respect to the unmodified model. In a subsequent work, Vemula and Sinha⁸¹ explored the use of an SU modified EARSM. After demonstrating similar behavior to the SU modified RSM⁷⁹ for the canonical STI, the authors showed superior predictions with respect to other turbulence models on a two-dimensional SWBLI problem. Karl *et al.*⁸⁰ introduced a correction for RSM, derived from the same canonical STI problem. They applied the correction on two RSM models retrieving the DNS behavior for the canonical STI. The model does still require further development as it violates Galilean invariance. Raje and Sinha⁶⁴ modified the SST model to account for anisotropies including SU physics. The new model, dubbed SUQ-SST, was applied to three two-dimensional SWTBLI configurations with some level of improvement in terms of separation onset and heat flux prediction with respect to the standard SST model⁴⁶ and similarly to better predictions with respect to a reference EARSM.

The various developments listed above have only been applied to a limited number of test cases. In order for a wider community to adopt new models, a larger set of validations is required, and if undesirable features are identified, shielding modelling mechanisms should be devised. This problem has also been pointed out by Roy and Blottner²⁵ and is key to advancing the field of hypersonic RANS modelling. The remainder of this work (Section IV and Section V) discusses the newly performed code-to-code comparison, assessing widespread and newer RANS turbulence models on cone-flare geometries.

IV. COMPUTATIONAL SETUP

This section describes the general guidelines given to the participants (IV A) followed by a brief description of the CFD solvers and associated settings used.

A. General Approach

The aim of this endeavour is to establish as of 2024, the capability of CFD solvers to simulate representative hypersonic flows with RANS approaches. A balance between commercial and research CFD codes (open-source and non open-source) have been adopted by the participants (see Table III). Throughout the literature (see also Section III), a general observation is the limited usage of commercial CFD software in simulating such hypersonic validation cases, or code-to-code comparison campaigns (GASP in²⁸, GASPEx in³⁰⁻³³ and STAR-CCM+ in³⁵). Nevertheless, commercial codes are expected to play an important role in enabling a wider industrial community to perform hypersonic design tasks. This has become apparent in their development over the last years. It is therefore not surprising to see some of the participants to rely on commercial software.

Unlike typical code-to-code comparison studies, no mesh is provided nor any domain discretization approach imposed. Each participant is free to choose whichever computational domain and meshing strategy is most suited. An important requirement to the participants is to demonstrate grid independence in the provided results. By allowing more freedom, the idea is to approach this comparison campaign from a more industrial / application-oriented perspective. It is up to the researcher / engineer to use their skills to the best of their capacity.

Participants are free to choose which RANS model to adopt, but it is encouraged to have at least a two-equation turbulence model. In the end, the aim is to assess the variation in predictions by comparing similar families of turbulence models. A brief description from each participant's strategy is given here-after.

A consensus regarding the adequate simulation of these geometries is the stringent requirement of very fine grids in spite of the 2D axi-symmetric nature that can be leveraged to lower computational cost. This characteristic becomes even more problematic when three-dimensional simulations of similar physics should be considered, for example, in a three-dimensional conical intake⁸³.

B. Star-CCM+ (Destinus SA)

In the current effort, with STAR-CCM+⁸⁴ version 2210, the desire was to step away from a structured grid approach described in³⁵ and instead rely on a strategy which would be feasible with any type of geometry, regardless of its complexity. This is achieved by using a combination of unstructured cells and a prism layer setup. An increased cell count is introduced in the cone-flare junction in order to more accurately capture

the shock structures as well as along the leading edge shock. In terms of prism layers, y^+ values below 3 were achieved by all meshes with the finer meshes ensuring values below 1 across both ramps (minimum allowed first cell distance of 5e-7 m). Grid sizes varied between 0.5M (coarsest) to 1M cells (finest). Mesh independence is achieved and results for the finest grids are presented (1.15 M cells for Case 1 and 1.02 M cells for Case 2). Note that the amount of cells required to predict the physics associated with hypersonic cone-flares is very high, especially for a two-dimensional axi-symmetric simulation. It is unfortunately a known limitation of finite volume codes developed for practical problems.

The governing equations were solved using an implicit time stepping approach with inviscid fluxes treated with the AUSM+ flux-vector splitting. The spatial discretization is performed through a third-order MUSCL scheme with order reduction in the vicinity of strong shocks. Other solver settings were left at their default values. Simulations were performed with a maximum CFL number of 1 which was an important requirement to converge the solutions in conjunction with the cell aspect ratios.

The two-dimensional axi-symmetric solver is selected in conjunction with Menter's SST 2003 turbulence model⁷⁴. The default model version used in STAR-CCM+ (based on the available technical implementation guide) contains the "controlled decay"⁸⁵, the rotation/curvature correction as well as Durbin's realizability constraint⁸⁶ for the turbulent viscosity. The " $2/3 \rho k$ "-term is considered in the production term of TKE. Based on the NASA Turbulence modeling resource naming guidelines⁸⁷, the model should be referred to as SST-2003RC-sust + Durbin's realizability.

Following the detailed turbulence sensitivity study by Cross and West³⁵, the following turbulence solver settings were changed: usage of a quadratic constitutive relation (QCR)⁵², deactivation of the compressibility correction (turbulent Mach number based) and the modification of the a_1 model coefficient to 0.355 (default of 0.31)⁵¹. The working fluid, air, is treated as a thermally perfect gas. A constant turbulent Prandtl number of 0.89 is used. Freestream turbulence values were set according to the study of the Aselsan partners. That is, turbulence intensity of 1 % and turbulent viscosity ratio of 1 for the first test case. Settings of 5 % and 10 for the same parameters, respectively, were applied for the second case.

Convergence of simulations were evaluated by monitoring the sum of the heat fluxes and skin friction on each of the ramps separately and ensuring no changes larger than 1 %. Moreover, it was ensured that the separation location did not move any more which was actually ensured by the heat flux monitoring method. Other monitors included the mass imbalance, integrated aerodynamic forces and wall shear stress (also for separation location).

C. Eilmer (University of Queensland)

Eilmer is an open-source compressible flow simulation code developed at the University of Queensland for study-

ing high-speed and hypersonic flow problems⁸⁸. In this work, Eilmer has been used to simulate all of the runs on both flow geometries, using high-order structured-style reconstruction and the LDFSS2⁸⁹ flux calculator, along with the production-limited, vorticity-source term, 2006 k-omega turbulence model (Wilcox2006-klim-V)²⁰, accelerated using a Newton-Krylov steady state solver⁹⁰. The flow was modelled as a single-temperature, non-reacting, thermally perfect gas with temperature dependant specific heats, computed using the NASA Glenn Thermodynamic database⁹¹. The vorticity-source k-omega model was found to have better stability at high CFL numbers than its standard counterpart (Wilcox2006-klim), though both produced similar results in terms of wall pressure and heat transfer. A constant turbulent Prandtl number of 0.89 was used for all simulations.

A pair of two dimensional quadrilateral structured meshes were created using Eilmer's built-in grid generation software, one for each model geometry. These meshes were then clustered using a geometric cluster function that begins with a first cell height Δ , and run using axisymmetric source terms to affect a perfectly sharp leading point. Testing revealed that the clustering level on the cone flank was the most critical driver of resolution requirements, and so a formal resolution study was conducted using the parameters in table VII.

Geom 1	Cells	Total	Δ	Flare	y^+	Flare
Loose	3328×256	851,968	0.36 μm	0.41		
Nominal	3328×256	851,968	0.14 μm	0.17		
Tight	3328×294	978,423	0.07 μm	0.08		

Geom 2	Cells	Total	Δ	Flare	y^+	Flare
Loose	2558×385	984,830	0.55 μm	1.39		
Nominal	2558×385	984,830	0.27 μm	0.71		
Tight	2558×385	984,830	0.14 μm	0.36		

TABLE VII: Eilmer grid configuration summary.

With three solutions of each run available, it is possible to estimate the exact converged value q of the heat transfer to the cone flank using equation the Richardson extrapolation (equation 1).

$$q = \frac{q_1 \Delta_2 \Delta_3 (\Delta_2 - \Delta_3) + q_2 \Delta_1 \Delta_3 (\Delta_3 - \Delta_1) + q_3 \Delta_1 \Delta_2 (\Delta_1 - \Delta_2)}{(\Delta_1 - \Delta_2)(\Delta_1 - \Delta_3)(\Delta_2 - \Delta_3)} \quad (1)$$

Equation 1 has then been used to estimate the convergence of the nominal meshes for each case, which are shown in table VIII.

Runs were parallelised using block decomposition over 72 (Geom 1) or 96 (Geom 2) cores using UQ's Bunya supercomputer. Deep convergence of the residual dU/dt (at least 10 orders of magnitude drop) was obtained in the range of 186–393 CPU/hrs (see figure 5), with some cases taking longer than others due to slow settling times of the corner separation.

A complete archive of the Eilmer simulations conducted for this project, including converged flow fields and postprocessing code, is available here.

Run	Mach	h (MJ/kg)	Cone		Flare	
			W/cm ²	Error	W/cm ²	Error
33	6.17	0.5	0.83	0.2 %	14.4	0.8 %
14	7.18	0.8	2.49	0.1 %	43.6	0.9 %
37	8.21	0.9	2.74	0.1 %	53.1	1.3 %
04	11.0	1.7	6.99	0.3 %	183.2	0.4 %
06	13.1	2.0	8.86	0.1 %	230.2	1.9 %
41	8.10	2.4	12.90	0.2 %	203.5	1.2 %
34	6.03	1.4	13.41	0.4 %	166.1	1.9 %
28	4.96	1.3	22.37	0.5 %	214.4	2.6 %
45	5.90	2.0	37.77	0.5 %	416.7	2.7 %

TABLE VIII: Wall heat transfer and estimated spatial convergence error, nominal grids, all Eilmer runs.

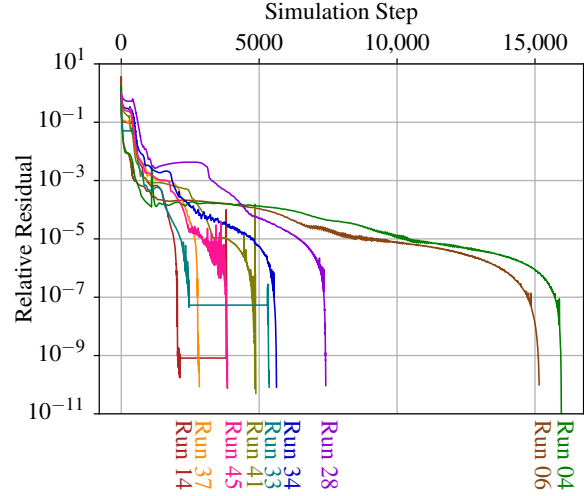


FIG. 5: Eilmer steady-state convergence plot.

D. TAU (DLR)

DLR TAU is a hybrid structured/unstructured Navier-Stokes solver developed by DLR and in use for over 25 years. The hybrid structured/unstructured DLR Navier-Stokes solver TAU^{92,93} is validated^{94,95} for a wide range of steady and unsteady sub-, trans⁹⁶- and hypersonic⁹⁷ flow cases. The TAU code is a second order finite-volume solver for the Euler and Navier-Stokes equations in the integral form using eddy-viscosity, Reynolds-stress or detached- and large eddy simulation for turbulence modelling. An improved Advection Upstream Splitting Method (AUSMDV⁹⁸) flux vector splitting scheme was applied together with Monotonic Upstream-centered Scheme for Conservation Laws (MUSCL⁹⁹) gradient reconstruction to achieve second order spatial accuracy. TAU allows for the computation of flows in thermal and chemical equilibrium and non-equilibrium. For cases with chemical non-equilibrium (e.g. in a rocket combustion chambers¹⁰⁰) the reacting flow can be modeled using finite rate chemistry¹⁰¹ or flamelet modelling.

In order to determine required grid sizes a study on hybrid (unstructured / structured) grids generated by the Centaur mesh generator were used in conjunction with the Menter k-w SST turbulence model in the 2003 formulation⁷⁴. The 2D grid sizes ranged from 100k points to about 800k points. Fine grids

at about 600k points were needed to obtain the same heat flux slope. The first grid point was varied between 1e-3mm and 1e-4mm between the different grids, coarser first grid point spacing lead to overestimation of the heat fluxes. The use of QCR did not lead to any significant changes in the results. Both the Thornber modification¹⁰² as well as shock turbulence correction were used. The turbulence models and their corresponding NASA nomenclature (where available) are summarized in table IX.

For the gas model, perfect gas with $\gamma = 1.4$ and the appropriate Sutherland viscosity fit for air were used. The laminar Prandtl number is 0.72 and the ratio of the laminar to turbulent Prandtl number was 0.8.

TAU turbulence model	no-eq.	NASA nomenclature	reference
SAO	1	SA-noft2	
SA-neg	1	SA-neg	
Wilcox k- ω	2	Wilcox1988	
Menter SST.2003	2	SST-2003	
Menter BSL	2	BSL	
Wilcox k- ω + SST	2	NA	
EARSM WJ3D+TNT	2	NA	¹⁰³ and ¹⁰⁴
EARSM WJ+Hellsten	2	NA	¹⁰⁵
SSG/LRR-w.2010	7	NA	¹⁰⁶
Wilcox RSM.2010	7	NA	

TABLE IX: Overview TAU turbulence models. NA: not available on NASA turbulence modeling resource.

E. HyperCODA (DLR)

HyperCODA^{107–109} is the expansion of the physical and numerical modeling capabilities for high enthalpy flows and gas mixtures of a new generation CFD code called CODA (CFD for ONERA, DLR, and Airbus). This next-generation CFD solver is capable of solving large sparse linear systems derived from the implicit time integration of the RANS equations with the assumption of a single perfect gas on three-dimensional structured and unstructured grids using either second-order finite-volume or higher-order Discontinuous-Galerkin (DG) discretization. CODA¹¹⁰ has been extensively used to solve subsonic and transonic flow regimes because the code has been designed mainly for avionics applications at sub to low supersonic Mach numbers. Thus, as has been done for TAU, DLR has been internally developing an extension for hypersonic applications, HyperCODA, used here for the following calculations.

For this analysis, we are using an axial symmetric grid whose shape was built taking into account the theoretical value of the conical oblique shock wave angle derived using the Taylor-Maccoll function. Thus, the obtained CFD grid is as tailored as possible to the predicted shock. Furthermore, the outflow region was extended to allow the expected expansion fan to develop around the corner, as well as the interaction between the shock generated at the stagnation point and the second shock wave caused by the flare.

In HyperCODA, the simulation was run using a second-order finite volume discretization method of the RANS equations in combination with the negative Spalart-Allmaras¹¹¹ one-equation turbulence model (RANS SA-neg, according to the NASA Turbulence modeling resource naming guidelines⁸⁷) and the AUSM+M¹¹² (Advection Upstream Splitting Method) convection scheme. The governing equations were solved with implicit time stepping and Switched Evolution Relaxation (exponential) ramping of the CFL based on the maximum residual of the state variables. The final converged solution was obtained with a second-order reconstruction with the Venkatakrishnan's limiter function of the primitive variables and their gradients, which were computed using the standard Green-Gauss method. The initial conditions are the ones reported in Tab. II for the Run 45. The turbulent Prandtl number was set to $Pr_t = 0.9$.

F. GASPEx (Rutgers University)

GASPEx¹¹³ is multi-physics package that primarily solves the RANS equations. All details are provided in³³ with the most relevant information given below.

The axi-symmetric character of the experimental setup was used and quadrilateral structured grids generated. Grid sizes ranging from 0.7 to 10.2 M cells are considered (2 nodes in the spanwise direction). Grid independence is demonstrated and the finest grid results are employed.

Inviscid fluxes are treated with a third order ROE scheme and Min-Mod flux limiter for the reconstruction. Temporal integration is achieved through an inner-iterative Gauss-Seidel scheme. CFL numbers between 0.1 and 5 were adopted. Sutherland's law is adopted for both the dynamic viscosity and thermal conductivity. Wilcox' k- ω 2006 model (Wilcox2006 naming following⁸⁷) is selected for turbulence modeling without any limiting or compressibility correction.

G. Fidelity DBS (Cadence Design Systems)

Cadence's Fidelity is a CFD environment covering all the main CFD workflow stages, including geometry preparation, mesh generation, simulation, and result analysis. In this study, Fidelity Hexpress mesh generator and Fidelity density-based solver (DBS) are used.

An unstructured mesh is generated with Fidelity Hexpress. A surface-to-volume approach¹¹⁴ is selected since it is a conventional approach for the aerospace industry thanks to its anisotropic surface meshing capabilities, which are particularly useful for aircraft leading and trailing edge meshing. In this approach, the surface mesh is generated as a first step, followed by the boundary layer extrusion, octree-based volume mesh generation, and reconnection between the boundary layer frozen surface and the volume mesh.

A 2D axisymmetric meshing strategy is adopted, with 1 cell in the third direction covering 2 degrees of the geometry and using the symmetry boundary conditions on the periodic boundaries. Mesh convergence studies have been done,

confirming consistency and good grid convergence properties. The results presented in this paper are based on the finest mesh from these mesh convergence studies. The mesh sensitivity studies comparing the first cells sizes revealed that it is necessary to keep the maximum y^+ on the flare part below 1. The mesh settings for the presented results ensure the maximum y^+ of around 0.3, average y^+ below 0.05, and the cell size in the shock region of 0.000625 m. The boundary layer is generated using the first cell size of 1.5E-7 m, 2 equal height cells at the wall, and 89 layers for Case 1 and the first cell size of 2.5E-7 m, 2 equal height cells at the wall, and 89 layers for Case 2. An approach with uniform refinement in the downstream shock region is employed due to its simplicity and ability to study multiple experimental setup operating points with different Mach angles. The total cell count is equal to 1459047 cells for Case 1 and 2214034 for Case 2. An optimal mesh based on a tailored refinement box following the shock and shock-induced separation regions or solution-based adaptive remeshing can be used to drastically reduce the cell count.

The Fidelity density-based solver (DBS) is employed to solve the governing system of equations for flow and turbulence. The flow solver applies a cell-centered finite volume method with local time-stepping for the integration of the governing flow equations. The convergence is accelerated by using the in-house CPU Booster technique and geometric multigrid techniques. Several spatial discretization techniques are available, namely the second-order central Jameson, Schmidt, and Turkel scheme with scalar and matrix dissipation formulations, Roe-type upwind scheme, and AUSM-type Low-Diffusive Flux Splitting Scheme (LDFSS). Pseudo-time integration is performed using an explicit multi-stage Runge–Kutta scheme. The solver features multiple RANS turbulence models together with more advanced Large Eddy Simulation and hybrid RANS/LES models. The turbulent heat flux vector is modeled by introducing a turbulent thermal conductivity connected to the eddy-viscosity through a turbulent Prandtl number.

The results presented in this paper are obtained using the second-order LDFSS scheme with Barth limiter, Menter's SST 2003 turbulence model with the a_1 coefficient set to 0.355 and SSC-EARSM turbulence model¹¹⁵. The Turbulent Prandtl number is set to 0.86 following the literature review done in²⁵ and experimental measurements in supersonic flows by Van Driest¹¹⁶. A single-temperature non-reacting gas model based on viscosity, thermal conductivity, and specific heat capacity (C_p) properties as a function of temperature following Lemmon¹¹⁷ for Mach 5.9 and blended law following Lemmon¹¹⁷ for temperatures below 500K and Gupta's model¹¹⁸ for 500K and higher for the Mach 11 and 13.1 cases. The Gupta's model that takes into account such hypersonic real gas effects as vibrational excitations, dissociation, ionization, and recombination. To avoid the dependency of the transport properties on the pressure, the pressure for Gupta's model is assumed to be equal to 1 atmosphere. The comparison of different fluid property models is given in Table X. The comparison is shown for 1500K, which is close to the maximum temperatures observed in the cases run by Cadence in Fidelity DBS. The maximum temperatures observed for Mach

5.9, Mach 11, and Mach 13.1 are 1250K, 1130K, and 1500K, correspondingly. The fluid properties based on Sutherland's law presented in the table are estimated using the Sutherland's expressions for dynamic viscosity and thermal conductivity and calculating specific heat capacity assuming that Prandtl number is equal to 0.72.

T = 1500K	C_p (J/kgK)	Viscosity (Pa·s)	Conductivity (W/mK)
Sutherland's law	1010.8	5.261E-05	7.387E-02
Lemmon's model	1211.6	5.588E-05	9.583E-02
Gupta's model	1237.2	5.465E-05	9.373E-02

TABLE X: Fluid properties calculated by different fluid models at static temperature equal to 1500 K and static pressure equal to 101325 Pa.

Multiple sensitivity studies have been performed, confirming the choice of the settings in the final setup presented in this paper. The second-order upwind LDFSS and Roe schemes give practically equivalent results with maximum discrepancies not exceeding 1%, even for the coarsest mesh from the grid refinement study as assessed for the Mach 13.1 case. The upwind scheme limiter impacts both the pressure and heat flux distribution to a larger extent, with a similar impact from the limiter change observed for the LDFSS and Roe schemes. In general, the Barth limiter has an advantageous impact on the simulation accuracy compared to the Venkatakrishnan limiter due to lower numerical diffusivity. This finding is in line with conclusions obtained in other validation cases, such as sonic boom prediction.

A more advanced law for viscosity and thermal conductivity based on the 11-species equilibrium Gupta's model¹¹⁸ that takes into account the dependency of properties on both pressure and temperature was explored. The model has been implemented in a module for user-defined functions called OpenLabs. Compared to the baseline approach using the Gupta's model viscosity and conductivity profiles with no pressure dependency, using the model has practically no impact on the heat flux on the cone and leads to a ~0.1 % higher peak heat flux on the flare for the Mach 11 case. Such a small difference can be attributed to the fact that the dependency of viscosity and conductivity on pressure is more pronounced at higher temperatures compared to the temperature range predicted in the considered cases.

The variable turbulent Prandtl number model presented in¹¹⁹ has also been assessed. The model is an algebraic law based on the best fit to Direct Numerical Simulation data and is defined as follows:

$$\text{Pr}_t = 0.85 + \frac{0.012}{Pr} \quad (2)$$

The law leads to an asymptotic turbulent Prandtl number of 0.85 for large values of Prandtl number. In present simulations, higher values of the turbulent Prandtl number lead to higher heat flux predicted on the cone and flare part. Using the variable Pr_t model leads to a ~0.1% higher heat flux on the cone and the peak heat flux value on the flare for the Mach 11 case. For all the tested cases, the impact of the model on

the heat flux remained below 1%. The small difference is attributed to the fact that the tested variable turbulent Prandtl number improves the modeling for low Prandtl number cases while the variation of the Prandtl number in the flow in the considered cone-flare cases is relatively limited. For the Mach 11 case, the predicted Prandtl number range is from 0.498 to 0.721.

In addition to results obtained using the SST and SSC-EARSM turbulence models presented in this paper, predictions for a cone-flare case obtained using the SBSL-EARSM turbulence model are shown in¹²⁰.

H. SU2 (University of Waterloo)

SU2 is an open-source computational analysis suite for the solution of the Navier-Stokes equations and other partial differential equations in computational physics¹²¹. It has a broad user base in computational physics, with a strong emphasis in aerospace, and recent developments have added capabilities in non-equilibrium thermodynamics for applications in high-Mach number flows¹²². Despite the relevance of these advances to the present work, the classical equilibrium thermodynamic model—but with variable thermophysical properties—is used herein in order to use a variety of turbulence models.

The simulations are run in SU2 (Harrier, v. 8.01) with the Menter SST Two-Equation Model (SST 2003m). The steady-state simulations are run using a first-order scheme for stability, robustness, and to allow for the use of higher CFL numbers. The RANS equations are closed with an ideal gas equation of state. The fluid viscosity is temperature dependent using Sutherlands law; the molecular and turbulent Prandtl number set to 0.72 and 0.9, respectively.

A two-dimensional, fully structured, axisymmetric mesh was generated in Gmsh. The stretching ratio of the grid in the wall normal direction was set to 1.05 for all cases. A mesh independence study was undertaken on Run 4, with three different grid resolutions from 166,500 (coarse) to 1,354,500 (fine) elements. The wall normal position of the first grid point played a determining role in the accuracy of the peak heat flux estimation. For the grid independence study, we used: 6.6E-5 m (coarse), 5.8E-6 m (medium), 4.4E-8 m (fine). The fine mesh with the first grid point at 4.4E-8 m is used throughout as the baseline. The y^+ is maintained below unity over all the domain, except on the flare, where the local y^+ peak value is 13.5 (coarse), 6.2 (medium) 0.1 (fine). As a comparison, on the leading cone, the y^+ for the coarsest mesh is below 2.5. To avoid numerical instabilities at the sharp leading edge, a blunt nose, with a radius of 0.5 mm was used as baseline, although this represents a rather blunt leading edge, the sensitivity of the results to the nose radius is explored later.

The convergence was evaluated based on the stabilization of the friction factor and integrated heat flux. Both quantities needed to stabilize to below 0.005% variation over at 20 iterations while having at least a three decade drop in the other residuals. The residuals at convergence remained low (e.g. below 10^{-8} for density), but other quantities did not show the same reduction (especially omega) as typically encountered

in low-speed calculations, irrespective of mesh and solver settings. Most simulations required between 80,000 and 200,000 iterations to reach a sufficiently converged state. The heat flux was the most sensitive parameter; often, the pressure and velocity profiles rapidly reached the final, converged state while the heat flux was continually decreasing until a final converged state was reached. Each of the fine simulation cases was typically run for between 12 and 20 hours on 40 processors on the Niagara cluster at SciNet, a member of the Digital Research Alliance of Canada.

I. Ansys Fluent (Aselsan)

Two-dimensional axi-symmetric simulations are performed with a structured quadrilateral mesh for Runs 4, 6, and 28, and with an unstructured combined quadrilateral and triangular mesh for Run 45. Present simulations were run on grids generated with ICEM CFD for Runs 4 and 6 and Ansys Meshing software for Runs 28 and 45. Grid sizes between 1M and 19M cells were used for Runs 4 and 6, while those ranging from 0.9M to 8M cells were utilized for Run 28. For Run 45, a pressure-gradient and density-gradient mesh adaption was used to limit the cell count resulting in grid sizes between 0.4M and 0.8M cells. Results presented herein are obtained on 10M, 19M, 8M, and 0.8M element grids for Runs 4, 6, 28, and 45, respectively. Mesh independence was achieved, and values of y^+ below 1 were ensured on all four grids.

The density-based solver is utilized with an implicit formulation and inviscid fluxes are treated with an AUSM+ flux-vector splitting scheme in Ansys Fluent 2021R2, 2022R2, and 2023R2 for Runs 4, 6, and 28, respectively. The pressure-based coupled solver in Ansys Fluent 2021 R1 is used for Run 45. The Green-Gauss Node Based method is applied for gradient reconstruction and second order (upwind) spatial discretization is employed for all cases. A steady-state formulation and thermally perfect gas assumptions are adopted. A constant turbulent Prandtl number (Pr) of 0.85 is used. The freestream turbulence parameters were set at a turbulence intensity of 1% and turbulence viscosity ratio of 1 for Runs 4, 6, and 28. Values of 5% and 10 were used for the same parameters in the Run 45 simulations. Note that insignificant changes were observed by prescribing 1% and 1 in Run 45 for these freestream quantities.

Predictions with the standard Menter k- ω SST model⁴⁶ are presented for all the selected runs with the a_1 model coefficient left at its default value of 0.31 and the production limiter⁴⁶ activated. Additional results obtained by setting the a_1 coefficient to 0.355 are presented for Run 28. Predictions with the Spalart-Allmaras model without f_{12} term (SA-soft2)¹²³⁻¹²⁵, employing the first order upwind scheme for the spatial discretization of the modified turbulent viscosity equation, are presented for Run 4. Simulations of Runs 4 and 28 are performed under both thermal equilibrium and non-equilibrium conditions. A two-temperature model is used to take into account the thermal non-equilibrium effects due to the hypersonic air flow over cone-flare geometries. In this model, the translational and rotational energy modes are as-

sumed to be in equilibrium with a translational-rotational temperature (T_{t-r}), while the vibrational and electronic energy modes are assumed to be in equilibrium with a vibrational-electronic temperature (T_{v-e}). In the mathematical formulation, this requires the solution of an additional equation for the vibrational-electronic energy¹²⁶, where the relaxation source term is modeled using the Landau-Teller theory and the relaxation time is modeled by Millikan and White's curve fits and Park's correction¹²⁷, and the description of the air properties in terms of T_{t-r} and T_{v-e} (specific heat, thermal conductivity, and viscosity based on NASA piecewise polynomials, Eucken relation, and Blottner curve fit, respectively).

Convergence of simulations was ensured by running the simulations until the wall pressure and heat flux values stabilized, checking that the residuals met default convergence criteria, and tracking mass-flux imbalances.

J. Ansys Fluent (Ansys Inc)

All the numerical simulations for the present section were run using the commercial CFD code Ansys Fluent 2024 R2. The Fluent solver offers the option to solve the Navier Stokes equations using either a pressure-based implicit solver (PBNS)^{128,129} or a density-based implicit or explicit solver (DBNS)^{130,131}, either in steady-state or unsteady mode. For this study, we utilize a 2D axisymmetric structured quad mesh. The mesh is created using Ansys SpaceClaim 2024 R2, and it is designed such that the cells in the boundary layer have a y^+ below 1. The present case is solved using the coupled steady-state DBNS solver. An Implicit, Roe Forward-Difference-Scheme (Roe-FDS) was used for the calculation of the convective fluxes. A second-order upwind spatial discretization is achieved using the Green-Gauss Node Based (GGNB) gradient formulation. High Speed Numerics (HSN), High-order Term Relaxation and Convergence Acceleration for Stretched Meshes (CASM) were used to improve convergence. Runs 14, 33 and 45 are simulated using non-reacting ideal gas air. Specific Heat, Thermal Conductivity and Viscosity are modelled using nasa-9-piecewise-polynomial, Kinetic theory and Sutherlands law respectively. Turbulence is modelled using a Generalized K-Omega (GEKO) model¹³². GEKO is based on the K-Omega formulation and provides users with four free parameters which can be adjusted over a wide range of applications. The default formulation of the GEKO turbulence model gives a close approximation to the Standard Menter SST Two-Equation Model, 1994⁴⁶. For all Runs, Coefficient of Separation (C_{SEP}) in the GEKO model is set to 1.50 due to late separation predictions. The turbulent Prandtl Number is set to a constant value of 0.85 for each case.

Each case is initialized with field values from the pressure far-field boundary. This is followed by a Full Multi-Grid (FMG) Initialization. Viscous terms are enabled for this FMG initialization step. Each simulation is run until residuals drop by 6 orders of magnitude. Variables such as maximum and minimum of pressure and temperature as well as average heat transfer over the wall were monitored. Stabilizing values of these parameters were considered as an additional acceptable

convergence condition. Mass imbalance is also monitored. A mesh independence study was conducted to evaluate the effect of the mesh on the pressure and surface heat transfer rates. Three meshes with 0.76 million (medium), 3.05 million (fine) and 12.23million (very fine) elements were constructed. y^+ values lesser than 1 were ensured on all grids. Results from these grids showed no impact of the grid resolution on the pressure and heat transfer rates predicted at the wall. Results for the medium mesh with 0.76 million cells and a minimum first cell height of 8E-7 m are presented in further sections.

K. OVERFLOW (Penn State University)

OVERFLOW¹³³ is a three-dimensional, structured, overset CFD solver developed at NASA for various flow problems. To evaluate the performance of the SST turbulence model in hypersonic applications, OVERFLOW was used to compare pressure and heat flux calculations with experimental values for run 4 of the 6/42 cone and run 45 of the 7/40 cone. Convergence studies and grid independence studies were performed to evaluate the performance of different turbulence models at hypersonic speeds in comparison to the experimental results. The 2D structured meshes were generated using Pointwise® mesh generation software. Consequently, the axisymmetric grid was created in Chimera Grid Tools (CGT)¹³⁴, a NASA meshing tool. GRIDED was used to generate the axisymmetric volume grid. SRAP was used to control the wall-normal spacing. For the 6/42 case results, the grid consists of 1025 points along the cone surface and 97 in the wall-normal direction. In the 7/40 case, results for a grid with 1921 points along the cone surface and 193 in the wall-normal direction are presented.

OVERFLOW version 2.4b was used in this work with the HLLE++¹³⁵ upwinding scheme with SSOR¹³⁶ to handle the inviscid fluxes together with a MUSCL spatial discretization scheme. OVERFLOW relies on a switch to locally reduce the spatial order of accuracy in shock regions. The sensitivity of this shock sensor depends on a parameter internally referred to as DELTA (see also¹³⁵). Its value has been set to 5 and 10 for Case 1 and Case 2, respectively. The flow was solved with the SST turbulence model and the SST-RC correction term was used as well as the Secundov/Sarkar compressibility correction. A constant wall temperature of 532 Rankine was assumed over the cone surface. Ambient conditions for the experiments were assumed at the farfield boundary. For the exit plane of the grid, an axisymmetric condition is used along with setting the derivative to zero at the axis. The conditions at the leading edge extrapolate from the input conditions. The default turbulent prandtl of 0.9 was used. Each case was initialized with 1000 iterations at speed Mach = 0.8. Thereafter, an additional 200k iterations at the correct flow conditions were performed. Convergence is evaluated through a drop in residual exponential order (typically dropping in the range of [-3, -4]) as well as by monitoring the quantities of interest (separation) throughout the iteration process.

L. VULCAN (NASA Langley)

VULCAN-CFD offers a comprehensive set of capabilities to enable the simulation of continuum flowfields from subsonic to hypersonic conditions using structured multiblock meshes or fully unstructured meshes. For the simulations performed here, structured quadrilateral grids were generated using the Pointwise¹³⁷ grid generation package for each axisymmetric cone flare geometry. The grids were clustered at the surface to provide a nominal surface cell centroid y^+ value of 0.2 with a nominal stretch rate of roughly 5% for most of the computational domain. The streamwise spacing was fixed at 670 microns along the surface for Case 1 (6/42 degree cone-flare at Mach 11), and the maximum wall normal spacing outside of the boundary layer varied between one third (inflow region) and two times (flare juncture region) the streamwise distance. The total number of grid cells for this geometry was 4400×432 . For Case 2 (7/40 degree cone-flare at Mach 5.9), the streamwise spacing was also fixed at 670 microns along the surface, and the maximum wall normal spacing outside of the boundary layer varied between a one half (inflow region) and three times (flare juncture region) the streamwise distance. The total number of grid cells for this geometry was 3812×448 . The farfield boundary for each geometry was angled to approximately align the grid with the expected conical shocks shock structure.

Even though the grid was crafted to approximately align with the expected conical flow structure, numerical artifacts (in the form of flowfield disturbances) were present due to some misalignment of the cone shock with the grid lines. The “stair-stepping” of the conical shock as it transitioned between grid lines was clearly evident in the surface pressure distribution. Given this observation, the bow shock adaptation capability in VULCAN-CFD was enabled to both align and cluster the grid to the upstream conical shock wave. In order to utilize this feature, the sharp cone tip had to be replaced with a blunt leading edge to separate the shock from the surface. The bluntness radius was chosen as 0.144 mm (Case 1) and 0.168 mm (Case 2) based on the works of Lau et al.¹³⁸ and Kara et al.¹³⁹ that examined the nose radii requirements to essentially recover sharp leading edge boundary layer development. The boundary layer adaption feature was also enabled to optimize the wall-normal boundary layer distribution by enforcing an acoustic cell Reynolds number of 1.0 at the surface. The boundary layer adaption based on acoustic cell Reynolds number produced a smooth y^+ distribution with a wall spacing that is roughly half that from the hand-generated grid.

All axisymmetric simulations were advanced in pseudo-time via an incomplete LU factorization scheme with planar relaxation. The inviscid fluxes were evaluated using the Low-Diffusion Flux Splitting Scheme (LDFSS) of Edwards¹⁴⁰ with cell interface variable reconstruction achieved via the Monotone Upstream-centered Scheme for Conservation Laws (MUSCL) with a κ value of 1/3. The Venkatakrishnan slope limiter¹⁴¹ was utilized to mitigate spurious oscillations during this reconstruction process. This limiter often allows deep convergence for shock laden flows that is often

elusive for simulations that employ Total Variation Diminishing (TVD) limiters. The Venkatakrishnan limiter has a free coefficient that controls the level of limiting (higher values provide less limiting). A value of 100 provided good iterative convergence properties for the Mach 11 freestream conditions of Case 1, while a value of 10 was used for the Mach 5.9 conditions of Case 2. The viscous fluxes were evaluated using 2nd-order accurate central differences with the viscosity of air computed from a Sutherland law expression. Several variations of the 2003 Menter Shear Stress Transport (Menter-SST) and Spalart-Allmaras (SA) models were used to close the Reynolds stress tensor for this effort. A Courant-Friedrichs-Lewy (CFL) number of 10,000 was used for simulations that employed the Menter-SST model. The CFL number was set to 50 for simulations that used the SA model. The molecular and turbulent Prandtl numbers were set to 0.72 and 0.9, respectively, for all simulations.

The most compelling proof of iterative convergence is achieved when the residual norms have been reduced to machine accuracy. Unfortunately, this could not be achieved for all the simulations performed in this effort. When this criteria could not be realized, the residual L₂ norm was monitored until it stalled. At this point, the variability of the percent mass flow error, $100 \times (\dot{m}_{\text{out}} - \dot{m}_{\text{in}})/\dot{m}_{\text{in}}$, was monitored as was the integrated surface heat load to assess whether satisfactory convergence has been achieved. With the exception of one simulation, the following iterative convergence statements were satisfied:

- The value of the residual L₂ norm was reduced by at least 8 orders of magnitude.
- The percent mass flow error was constant at every streamwise grid plane to at least 5 significant digits.
- The integrated surface load time histories remained unchanged to at least 5 significant digits.

The outlier was the Menter-SST simulation for Case 1 that used the standard strain-based form for turbulence production. The residual L₂ norm for this simulation became oscillatory after dropping 4 to 5 orders of magnitude with a corresponding percent mass flow error oscillation of $\pm 0.2\%$.

V. RESULTS

This Section is structured as follows. Various code-specific comparisons are first introduced which include the influence of conical geometry nose bluntness (V C), thermal non-equilibrium (V B), turbulence model versions (V D) as well as specific modeling parameters (V A). An advantage of code-specific comparisons is the removal of grid influence on the predictions. Finally, Subsection V E provides a case-by-case and run-by-run comparison of the available predictions from the participants. As the aim of this work is to assess general predictive uncertainty, absolute variations are extracted and tabulated. All surface data is presented as function of the axial distance along the symmetry axis.

A. Influence of turbulence model variants with VULCAN

Several variants of the 2003 Menter-SST turbulence model were examined in this effort as was a variant of the Spalart-Allmaras with and without the Quadratic Constitutive Relation (2013 QCR version). The specific Menter-SST variants included the choice of turbulence production term treatment as well as the impact of removing the $2/3\rho k$ portion of the Boussinesq Reynolds stress closure. These variations represent popular implementations of 2-equation models, and the specific implementation choice can often be impactful when strong shocks are present. The Spalart-Allmaras model was chosen for evaluation given its popularity for external flow simulations, and to investigate the impact of a nonlinear eddy viscosity implementation (in this case the 2013 QCR formulation) for shock separated flows.

From the setups detailed in Section II, Run 4 of Case 1 and Run 45 of Case 2 are considered and no specific reference to the run numbers is used in the following discussions.

Figures 6 and 7 compare the impact of the particular choice used for the functional form of the turbulence production terms.

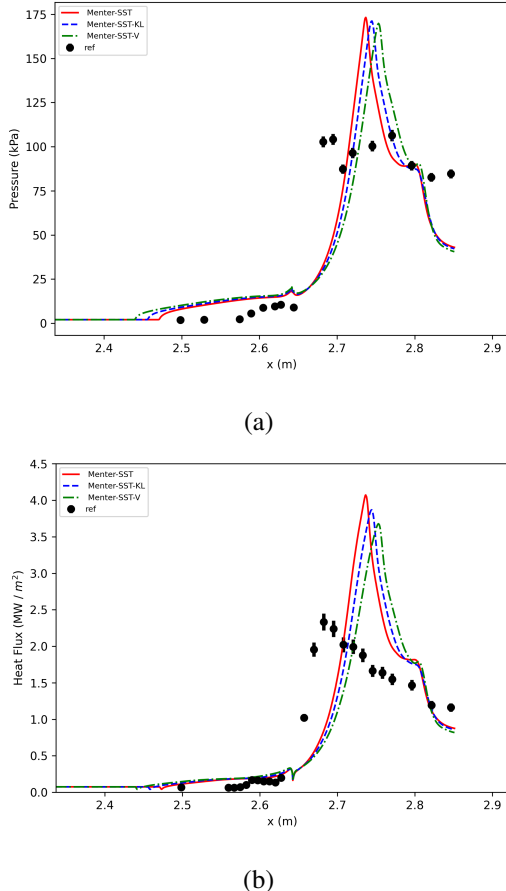


FIG. 6: Surface pressure (a) and heat flux (b) distributions obtained using various Menter-SST turbulence production term options for Case 1 (Run 4).

Figure 6 compares the surface properties for Case 1, and shows that the standard strain-based production term (Menter-SST) provides a delayed separation than when the vorticity-based production term (Menter-SST-V) is used. The Kato-Launder form (Menter-SST-KL) provides a separation bubble extent that is bounded by those obtained using the strain-based and vorticity-based forms, which is expected given that this variant is based on the inner product of the strain rate and vorticity tensors. Overall, the flow structure formed by the flare shock / boundary layer interaction is not overly sensitive to the particular form of turbulent production used. The same trends are observed in the results for the Case 2 configuration shown in Fig. 7.

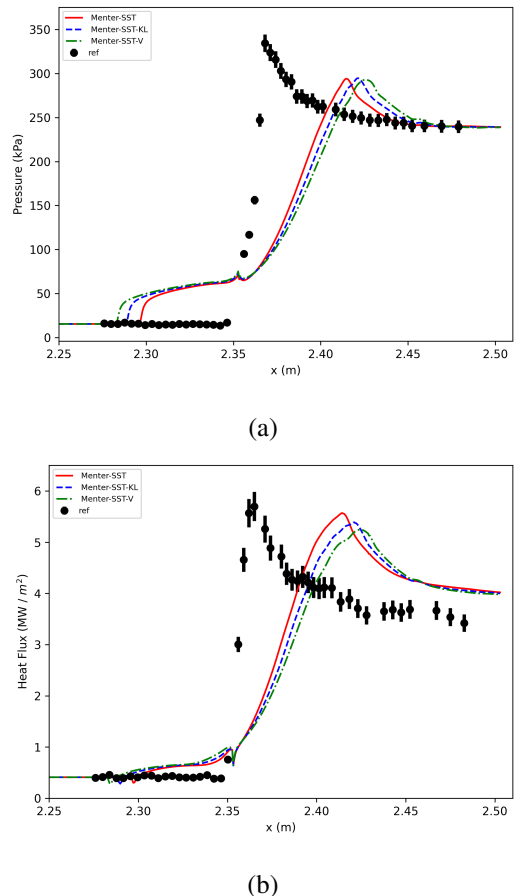


FIG. 7: Surface pressure (a) and heat flux (b) distributions obtained using various Menter-SST turbulence production term options for Case 2 (Run 45).

The impact of neglecting the $2/3\rho k$ terms that appear in the Boussinesq Reynolds stress closure for the normal stress components is shown in Figs. 8 and 9. The Menter-SST-V model was chosen as the base model for this comparison, with the Menter-SST-V_m label used to denote the neglection of the $2/3\rho k$ term in this model. The separation bubble extent is shown to be sensitive to this common approximation made to the Reynolds stress closure. In particular, the neglection of the $2/3\rho k$ term results in a considerably smaller separation bub-

ble size, which is more consistent with the measured results (albeit still substantially larger than the measured separation zone extent). The delayed point of incipient separation (i.e., smaller separation zone) leads to a more rapid pressure rise as the flow reattaches along the flare surface.

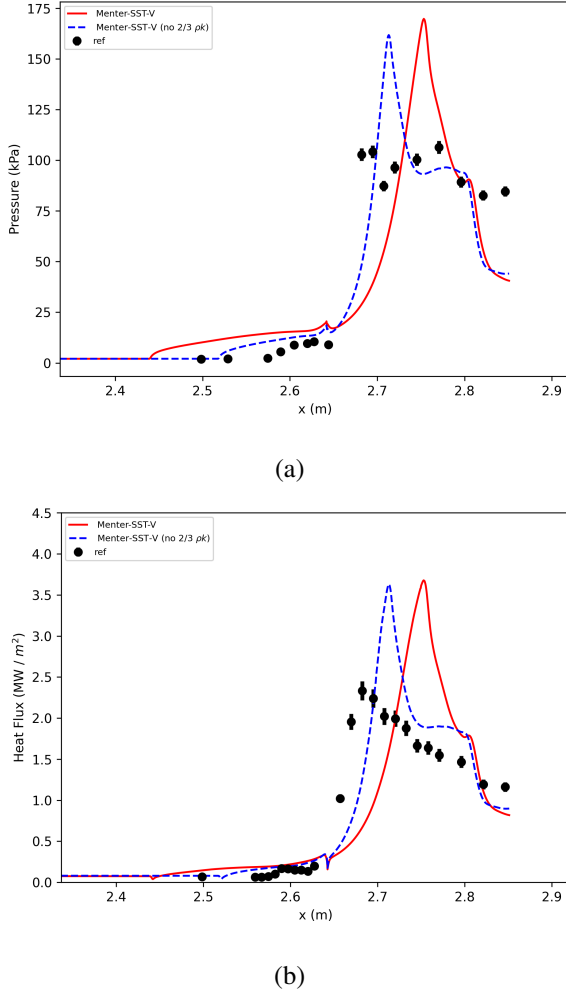


FIG. 8: Surface pressure (a) and heat flux (b) distributions obtained using the Menter-SST-V model with and without the $2/3\rho k$ normal stress term for Case 1 (Run 4).

The results for Case 2 shown in Fig. 9 also show a significant impact when the $2/3\rho k$ term is neglected, once again leading to a significantly delayed incipient separation point.

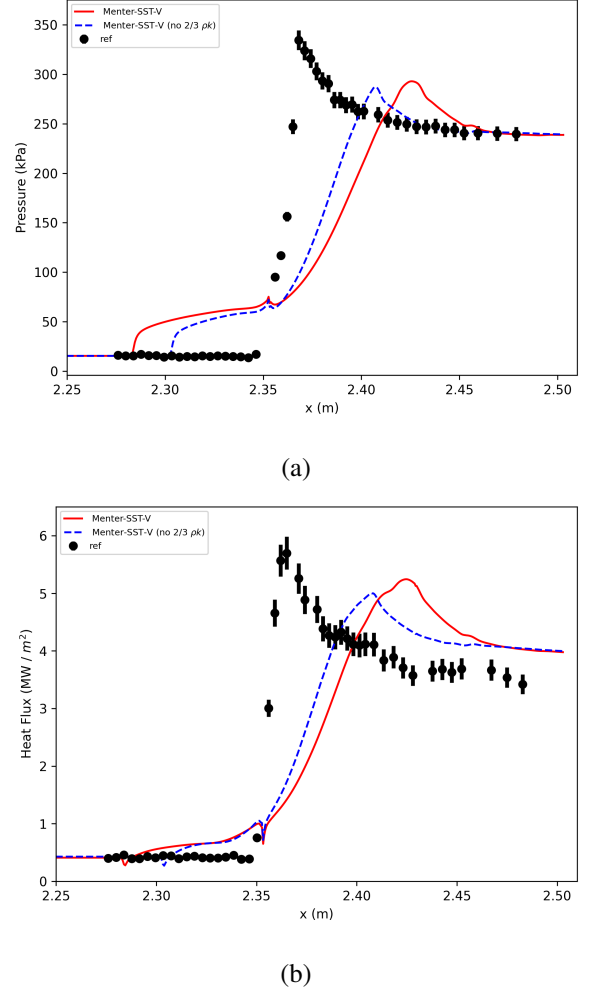


FIG. 9: Surface pressure (a) and heat flux (b) distributions obtained using the Menter-SST-V model with and without the $2/3\rho k$ normal stress term for Case 2 (Run 45).

Finally, the predictive capability of the Spalart-Allmaras model for these hypersonic flow configurations is provided in Figs. 10 and 11. Figure 10 shows the pressure and heat flux distribution comparisons for Case 1.

In contrast with the Menter-SST results shown previously, the SA model with the standard linear stress/strain constitutive relationship predicted no appreciable separation at the flare juncture. However, the use of the 2013 version of the QCR model predicts a significant level of flow separation that somewhat overpredicts the measured separation zone extent. Although not shown here, additional simulations were performed with the original 2000 version of the QCR formulation that produced results almost identical to those when the linear constitutive relationship is used. The only difference between the 2000 and 2013 QCR variants is the addition of a term that mimics the $2/3\rho k$ term that is present in models that contain a transport equation for the turbulence kinetic energy. Hence, it is the addition of this term, rather than the nonlinear constitutive relationship, that leads to the larger separation zone

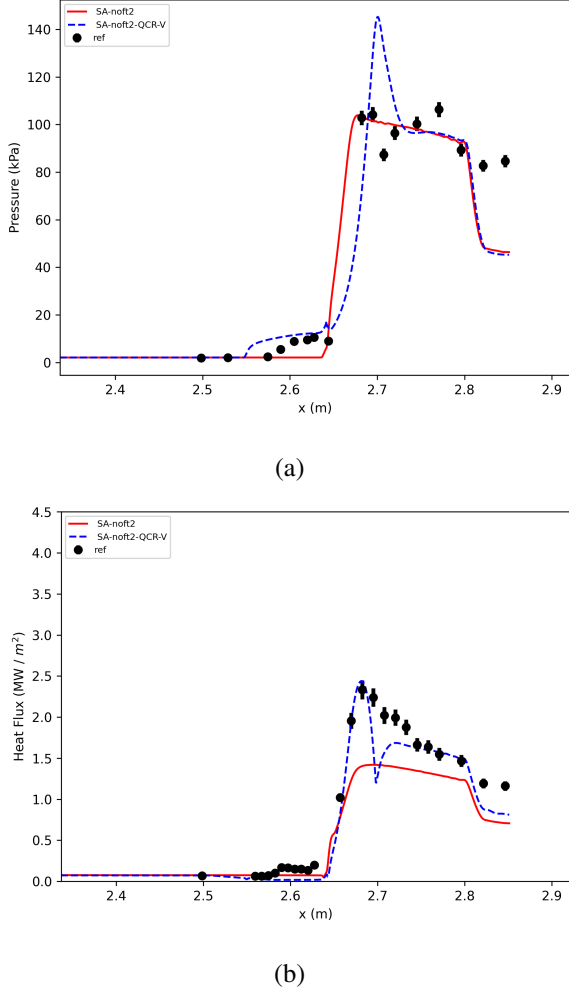


FIG. 10: Surface pressure (a) and heat flux (b) distributions obtained using the SA model with and without QCR for Case 1 (Run 4).

size. The trend of increased separation zone size with the addition of this modeled $2/3\rho k$ term is consistent with the trends shown in Fig. 8 discussed previously. Overall, the SA-noft2-QCR-V results compare more favorably with the heat flux measurements than the other models evaluated for this configuration. The same trends held when the SA models were applied to Case 2. However, in this instance the SA-noft2 model predicted minimal separation (consistent with the measurements), while the use of the 2013 QCR-V model produced too much separation (albeit considerably less separation than what was observed with the Menter-SST results).

In summary, the results shown here highlight the importance of clearly documenting the specific implementation of a given 2-equation turbulence closure model for hypersonic flow simulations. Many popular variations to the original published versions of the models, which often have inconsequential effects in low speed flows, were shown to be impactful when strong shock waves are present. Unfortunately, all too often the specific implementation details are not communi-

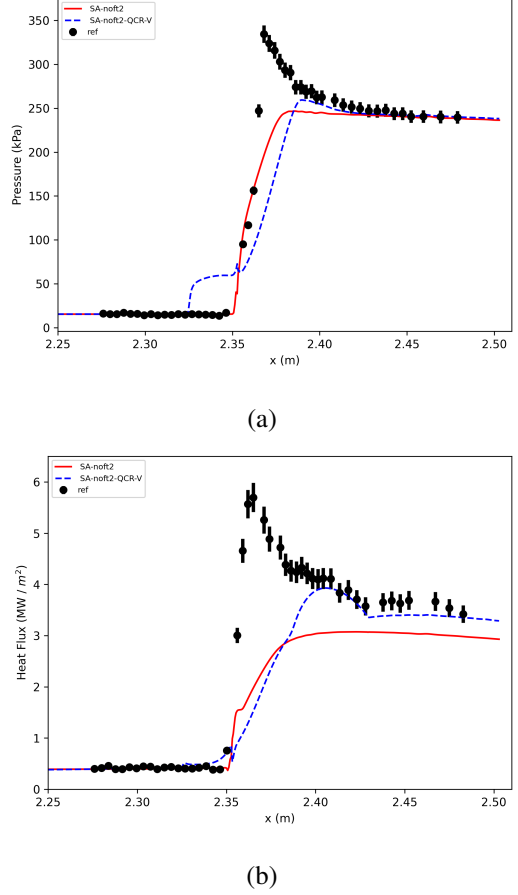


FIG. 11: Surface pressure (a) and heat flux (b) distributions obtained using the SA model with and without QCR for Case 2 (Run 45).

cated in published results (or for some commercial solvers, the specific implementation may not be known). This can lead to inconsistent conclusions being drawn concerning how a given model might perform for certain classes of flows. Of the 2-equation model implementation variations evaluated here, the omission of the $2/3\rho k$ term proved to have the largest impact on the flare juncture flow structure, and consistently drove the predictions closer to the measurements. The effect of using the Spalart-Allmaras model with the 2013 QCR formulation for these hypersonic flow configurations showed a significant impact when compared to results that used the standard linear stress/strain constitutive relationship. However, upon further examination, the impact was primarily driven by the inclusion of the effective “ $2/3\rho k$ ” term that differentiates the 2013 QCR version from the original 2000 version. The effect of including this term was qualitatively similar to that observed when the $2/3\rho k$ term is retained in the linear Boussinesq form of the Menter-SST Reynolds stress closure for these hypersonic flow applications.

B. Influence of thermal non-equilibrium with Ansys Fluent

Thermal non-equilibrium can impact the characteristics of a hypersonic flow field. Previous work on laminar sharp double-cones²⁸, for instance, has considered appropriate modeling for higher enthalpy freestream conditions. Presently, the freestream total enthalpy is moderate for all runs. Nevertheless, the impact of choosing to model thermal non-equilibrium effects through two temperatures, in conjunction with varying turbulence model, is presently assessed. Results have been obtained for Run 4 and Run 28 but only the former will be discussed below. In Test Case 1 – Run 4, when the Spalart-

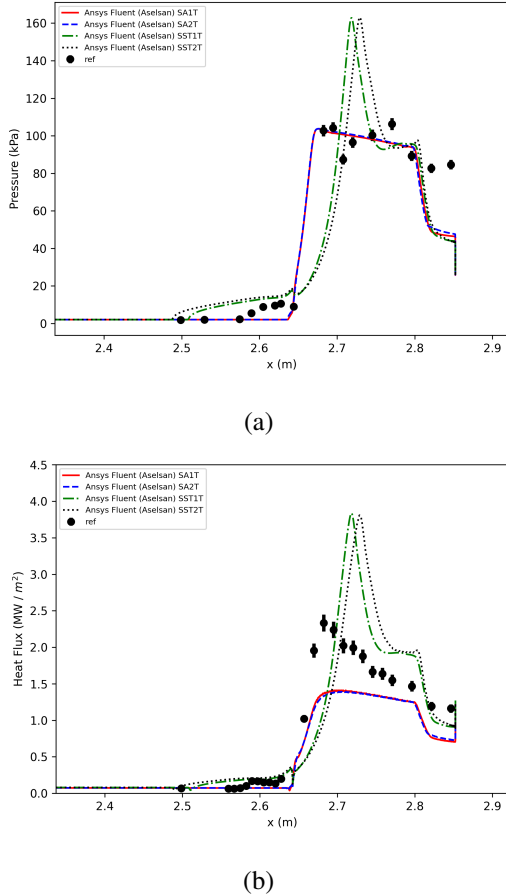


FIG. 12: Simulation results for Test Case 1 – Run 4 obtained using the SST $k-\omega$ turbulence model with one- (SST1T) or two temperature model (SST2T); Spalart-Allmaras turbulence model with one- (SA1T) or two temperature model (SA2T) in Ansys Fluent software presented in comparison with the experimental data. (a) Surface pressure and (b) surface heat flux distributions with respect to the axial distance from the nose of the cone.

Allmaras turbulence model is used, the one-temperature and two-temperature model results show insignificant differences. When the SST $k-\omega$ turbulence model is employed, the peak pressure and heat flux values obtained using both approaches are nearly identical (less than 0.7% difference). However, the

size of the separation bubble is larger in the two-temperature model simulations (Figure 12).

Thermal non-equilibrium effects shift the separation point approximately 20 mm upstream and the peak pressure and heat flux locations about 10 mm downstream. They also lead to increases of about 0.8% and 1.8% in the integrated wall pressure and heat flux, respectively. Figure 13 shows the contours of T_{t-r} , T_{v-e} , and $T_{t-r} - T_{v-e}$ in the Spalart-Allmaras and SST $k-\omega$ simulations.

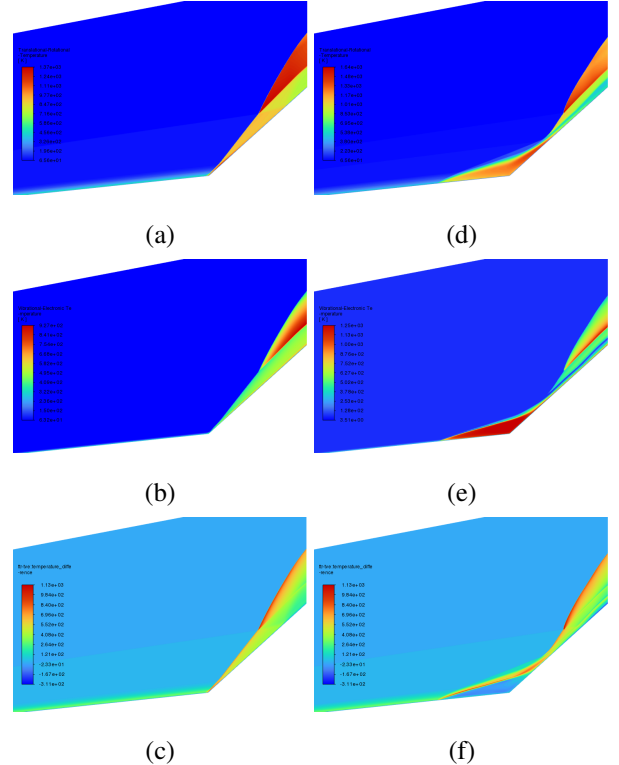


FIG. 13: Contours of (a) T_{t-r} , (b) T_{v-e} , and (c) $T_{t-r} - T_{v-e}$ in the simulations using the Spalart-Allmaras turbulence model and the two-temperature model, and contours of (d) T_{t-r} , (e) T_{v-e} , and (f) $T_{t-r} - T_{v-e}$ in the simulations using the SST $k-\omega$ turbulence model and the two-temperature model for Test Case 1 – Run 4.

The absolute magnitude of $T_{t-r} - T_{v-e}$ can be considered as an indicator of the degree of non-equilibrium in the flow. The shock waves generated by the cone-flare geometry disturb the state of thermal-equilibrium in the freestream. While the boundary layer separates and reattaches in the SST $k-\omega$ simulations, it remains attached in the Spalart-Allmaras simulations. This causes flow topologies, and consequently the degree and effects of non-equilibrium, to differ between the SST $k-\omega$ and Spalart-Allmaras simulations. Similar observations were seen in Run 28 with the SST $k-\omega$ model.

This exercise indicates that considering thermal non-equilibrium can alter the predictive results to some extent but its overall quantitative impact remains limited for a relatively low (for a hypersonic regime) freestream total enthalpy condition.

C. Impact of nose bluntness

The bluntness of the leading edge is known to play a critical role in defining the extent of flow separation, heat flux, and pressure distribution numerical¹⁴² and experimental⁶⁵ compression ramps. These effects are related to the change in stability characteristics arising due to the modification of the entropy layer for different nose radii^{139,142}. The change in stability characteristics can modify the transitional state of the flow, thus indirectly impacting first-order statistics far downstream of the leading edge. As the present RANS simulations do not account for neither transitional flows nor unsteadiness, the impact of the nose bluntness is investigated for run 4 within SU2 to assess its sensitivity. To better understand the effects of

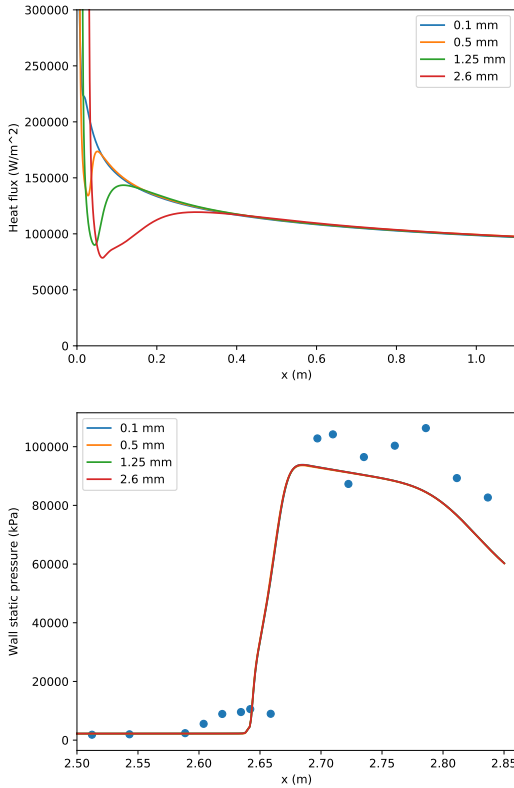


FIG. 14: Effect of the nose bluntness (for run 4) on the wall heat flux on the leading conical wall (top) and pressure profile at the flare (bottom).

the nose bluntness, we compare the flow statistics for 4 different leading edge radii: 0.1 mm, 0.5 mm, 1.25 mm, and 2.6 mm. All grids correspond to the same fine mesh resolution with the first grid point away from the wall at 4.4E-8 m with 15 grid points along the quarter circumference blunt leading edge. The largest variation among the bluntness is seen in the heat flux at the leading edge. The heat flux for all four cases collapses around 35 cm from the leading edge, see Figure 14(top). At the flare corner, the pressure distribution is not affected by the bluntness at the leading edge, whereas the peak heat flux at the flare varies at most by 9%.

D. Influence of turbulence model variants with TAU

For this study several different types of turbulence models available in TAU (one equation SA, variants of two equations k- ω model and explicit algebraic Reynolds stress model (EARSM) as well as 7-equation Reynolds stress model (RSM) were used to calculate Run 45. The results of the comparison for these different turbulence models for run 45 is shown in figures 15 and 16 .

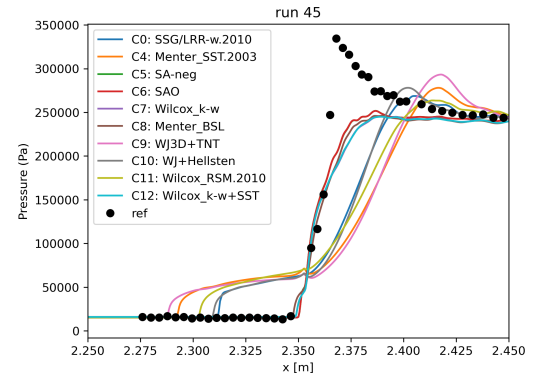


FIG. 15: Pressure distribution for run 45 using different classes of turbulence models.

For the different turbulence models only the k- ω models (Wilcox k- ω , Wilcox k- ω + SST, and Menter BSL) and the one-equation turbulence models (SAO and SA-neg) correctly predict the location of the separation bubble. For the heat flux no turbulence correctly predicts the location of the peak heat flux. While most of the k- ω models correctly predict the starting slope of the heat flux and the plateau values ($x > 2.4$ m), only Menter SST and the EARSM models gets close in predicting the peak values, but not the location. The RSM models have a similar performance in terms of peak values but also do not predict the location correctly.

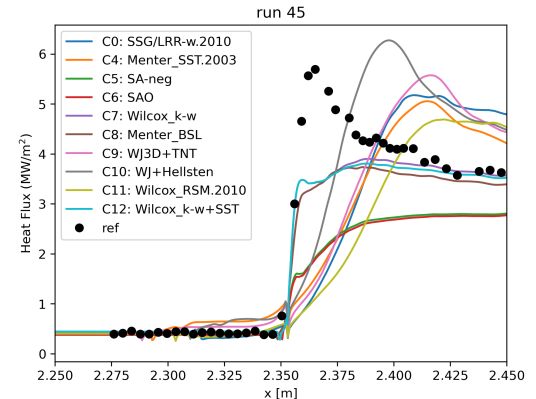


FIG. 16: Heat flux distribution for run 45 using different classes of turbulence models

E. Comparison between codes

This subsection discusses the results obtained by the current CFD simulations. As depicted in Table III, most of the participants provided data for run 4 and run 45. Therefore, a more extensive discussion is provided for these runs. For all runs, a comparative graph of pressure- and heat flux traces along the wall (axial distance) is presented as well as the integrated and peak quantities. The bounds for integration are set as [2.45,2.85] m and [2.24,2.49] m, for the first II B and second II C geometry, respectively. This was motivated by the separation predictions of the different test conditions, focusing on the SWBLI region. The quantitative tabulation of data of interest is intended for comparison purposes in future endeavours in simulating these conditions. Finally, the overview in terms of predictive variability for all cases is summarized in VE 10.

1. Run 4

Figure 17 illustrates the typical behavior with the Mach number field as obtained with Eilmer. Peak heat flux values on the flare are strongly overpredicted by the majority of the CFD results, which is a common observation in the literature for such type of flow features. Note that for this condition, the leading edge shock impinges on the flare. Depending on the accuracy of the model in predicting the separation onset, this impingement can be observed as a small bump in the pressure and heat flux traces. See, for instance, the Eilmer and Ansys Fluent results in Figure 18 or Figure 10 comparing two variation of the SST model with VULCAN.

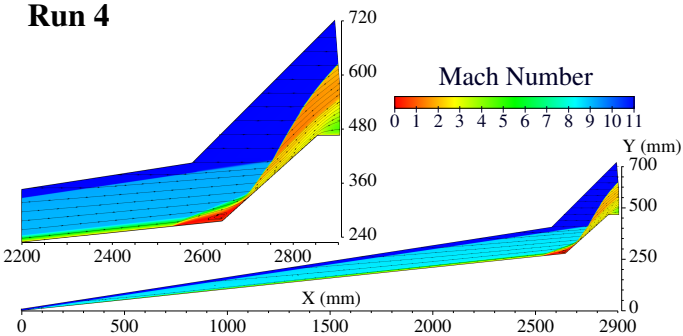


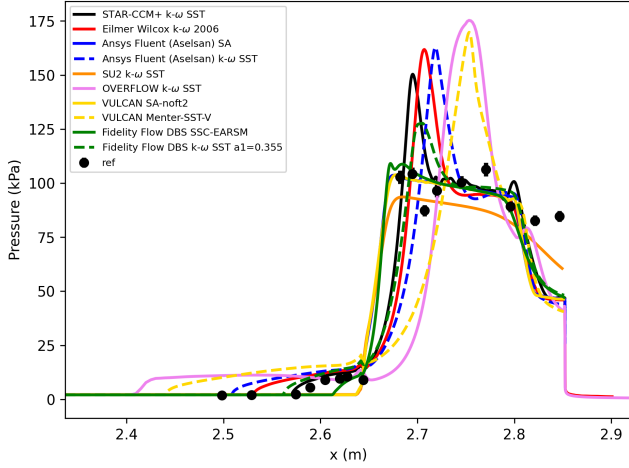
FIG. 17: Mach Number Color Map for Run 4, Computed with Eilmer

Figure 18 shows the pressure- and heat flux predictions along the wall obtained by the participants. Note that for Ansys Fluent (Aselsan), only the one-temperature (1T) model is presented following the limited differences discussed in Subsection V B. For VULCAN, only two of the six results are shown in order to not overload the graph. These results represent the separation bounds obtained by all simulations as seen in Table XII. Subsection V A illustrates the plots for all six simulation results. For this run, predictions with the one-equation Spalart-Allmaras (labeled as SA) model family and

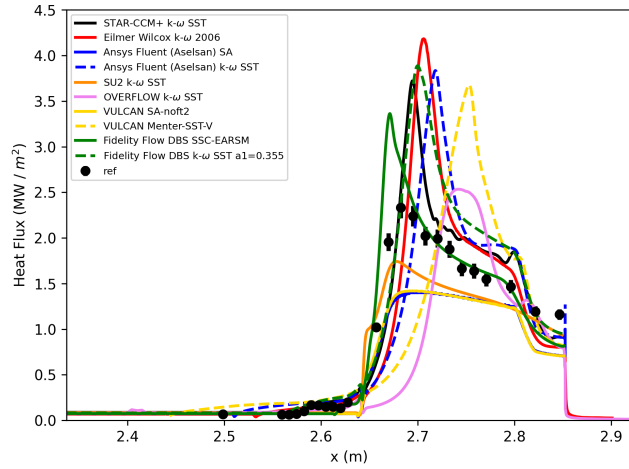
two-equation $k-\omega$ type family were obtained, as well as with an EARSM model. A significant spread in SWBLI behavior is observed as well as a clear difference between both family types. The SA models do not predict (or severely under-predict) a boundary layer separation at the cone-flare junction and is not in line with experimental observations. This, in turn, results in an almost leveled pressure - and heat flux trace on the flare with quantitatively similar predictions with the different solvers (see peak values in Table XII). While the CFD pressure levels are close to the experimental measurements, the latter fail in clearly identifying a peak pressure behavior on the flare induced by the separation shock (see naming in Figure 2) which could be due to the limited number of pressure samples. Heat flux levels on the flare are generally underpredicted by the SA model results. Note that using a QCR variation with the SA, as illustrated in Figure 10 results in a separation prediction and associated spike in flare pressure. However, it is emphasized that this separation was a result of the modelled $2/3 \rho k$ term associated with this QCR variant and was not caused by the nonlinear stress/strain constitutive relationship (see also V A). With the latter variation, the heat flux is in closer agreement with experimental data points and no peak over-prediction is observed. The two-equation $k-\omega$ type predictions do not show a uniform behavior across CFD solvers. Except for the SU2 result, a separation onset is predicted with such turbulence models. Differences in the extent of the separation result in differences of peak pressure and heat flux linked to the reattachment shock locations. The SSC-EARSM separation prediction is larger than for the SA (without QCR) family and smaller than the majority of the $k-\omega$ family.

Figure 19 presents the heat flux predictions on the cone. For this specific geometry, no experimental data is available to gauge the accuracy of the prediction, except for the first heat flux data point (see also Figure 18 (b)). In general, the heat flux values are of similar order of magnitude by the end of this section. The Run 4, Run 45 and Run 6 results reveal that some fully turbulent models (SSC-EARSM) can still predict the laminar region and subsequent laminar-turbulent transition. The behavior has been documented by NASA for the SA-Ia model and the SA-fv3 variant used in OVERFLOW¹⁴³. STAR-CCM+ predictions are on the higher level and do show the largest level of fluctuations which were similarly found in Figure 18 as well as in other run conditions in spite of grid independence and demonstrated steady-state solution convergence. A potential reason for the latter behavior is thought to be grid related, i.e. a failure in aligning grids with shock waves which result in numerical noise as well as a difficulty in handling higher aspect ratio cells at hypersonic flow conditions. Note that a similar behavior is found in the CFD predictions of Cross and West³⁵.

Tables XI and XII provides a quantitative summary for all simulation data provided for this condition. The integrated pressure quantities compared among similar turbulence model families differ by less than 6 %. In terms of heat flux the differences reach up to 54 %. Values are computed relative to the smallest prediction. The largest relative variation is found



(a)



(b)

FIG. 18: Comparative predictions of pressure (a) and heat flux (b) Case 1 (Run 4).

for the two-equation turbulence models.

2. Run 6

Figure 20 presents the quantities of interest at the wall for the $k-\omega$ SST, Wilcox' $k-\omega$ 2006 and the SSC-EARSM model. Predictions of the $k-\omega$ type models are qualitatively similar and relatively small differences in integrated quantities (Table XIII) are observed, except for the heat flux with the a_1 coefficient set to 0.355 which is higher. In this specific case, the latter setting results in a closer match with experiments and smaller peak values (Table XIV) than the other two predictions. Separation onsets and peak values differ slightly between Eilmer and Ansys Fluent. The three predictions also show the effect of the leading edge shock impingement on the wall pressure and heat flux traces (see also Figure 22). The

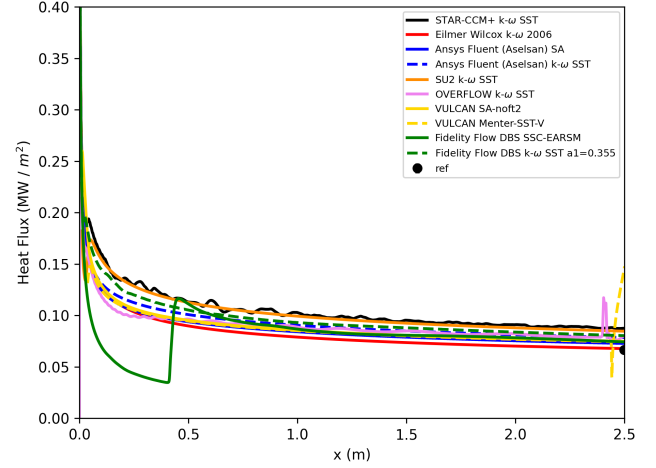


FIG. 19: Heat flux predicted by various solvers on the cone for Run 4

Solver	Turbulence Model	pressure (kPa)	heat flux ($MW/(m^2)$)
STAR-CCM+	$k-\omega$ SST	44.89	0.971
Eilmer	$k-\omega$ 2006	44.16	0.95
Ansys Fluent (Aselsan)	SA	43.73	0.624
	SA 2-T model	43.93	0.621
	$k-\omega$ SST	43.82	0.958
	$k-\omega$ SST 2-T model	44.25	0.98
SU2	$k-\omega$ SST	42.33	0.73
OVERFLOW	$k-\omega$ SST	44.39	0.696
VULCAN	SA	43.71	0.631
	SA 2013 QCR-V	43.88	0.756
	$k-\omega$ SST	44.05	0.959
	$k-\omega$ SST-KL	44.19	0.939
	$k-\omega$ SST-V	44.35	0.919
	$k-\omega$ SST-2/3 rho*k	43.81	0.93
Cadence Fidelity	SSC-EARSM	44.25	0.919
	$k-\omega$ SST $a_1=0.355$	44.38	1.075

TABLE XI: Integrated wall quantities for run 4 . Values are scaled by $\int dx$.

EARSM model predicts a smaller separation, which is consistent with observations for Run 4 in VE 1. Moreover, no peak heat flux overprediction at the separation shock's flare impingement location is found in the latter model's trace, unlike the $k-\omega$ family. Similar nose heat fluxes values are found prior to the interaction region as shown in Figure 21.

3. Run 45

Run 45 ($M=5.9$) is the highest heat transfer flow condition considered in this work, with a relatively high free stream temperature (244 K) and velocity (1852 m/s). Figure 23 shows the flowfield structure computed with Eilmer, once again coloured by Mach number. A notable difference from Run 4 is that the entire flare shock structure sits inside the shockwave coming off the cone, which reduces the narrow waist of the recompression shock and leads to a much lower spike in heat transfer to the flare. Figure 24 shows the heat flux traces on the cone with very similar trends between the solvers / turbulence models combinations. As mentioned in

Solver	Turbulence Model	x_{sep} (m)	p_{peak} (kPa)	$p_{peak,loc}$ (m)	q_{peak} ($MW/(m^2)$)	$q_{peak,loc}$ (m)
STAR-CCM+	k- ω SST	2.571	150.38	2.695	3.722	2.694
Eilmer	k- ω 2006	2.531	161.82	2.707	4.185	2.706
Ansys Fluent (Aselsan)	SA	2.638	103.67	2.676	1.41	2.702
	SA 2-T model	2.636	103.77	2.677	1.392	2.708
	k- ω SST	2.509	162.8	2.719	3.836	2.718
	k- ω SST 2-T model	2.489	163.05	2.729	3.809	2.729
SU2	k- ω SST	2.639	93.62	2.685	1.743	2.678
OVERFLOW	k- ω SST	2.415	175.32	2.753	2.534	2.742
VULCAN	SA	2.639	103.87	2.678	1.42	2.698
	SA 2013 QCR-V	2.549	145.22	2.701	2.44	2.681
	k- ω SST	2.472	173.18	2.737	4.072	2.737
	k- ω SST-KL	2.457	171.13	2.745	3.869	2.744
	k- ω SST-V	2.441	169.78	2.753	3.679	2.753
	k- ω SST-V no 2/3 rho*k	2.519	161.78	2.713	3.631	2.713
Cadence Fidelity	Fi- SSC-EARSM	2.614	109.1	2.672	3.364	2.671
	k- ω SST al=0.355	2.563	127.7	2.705	3.888	2.7

TABLE XII: Separation, peak values and associated location for run 4

Solver	Turbulence Model	pressure (kPa)	heat flux ($MW/(m^2)$)
Eilmer	k- ω 2006	50.51	1.304
Ansys Fluent (Aselsan)	k- ω SST	50.07	1.317
Cadence Fidelity	SSC-EARSM	50.81	1.227
	k- ω SST al=0.355	50.92	1.456

TABLE XIII: Integrated wall quantities for run 6 . Values are scaled by $\int dx$.

VE 1, a transition-like behavior of the SSC-EARSM can be obtained even if a fully turbulent flow is assumed¹⁴³.

In a separate discussion (see Subsection V D), the variability in turbulence models for a single grid and CFD solver has been covered. Separation onsets up to 6 cm prior to the flare junctions were found. For this specific run, however, the experimental Schlieren (and pressure traces) shows little to no separation⁵⁴. The trend observed in Subsection V D is also seen across the participants.

Presently, results are divided by similar turbulence model families. Figures 25, 26 and 27 provide the wall pressure and heat flux traces for one-equation, two-equation and EARSM / RSM type turbulence models, respectively. Figure 25 illustrates the standard behavior of the Spalart-Allmaras model seen in the literature which is the inability to predict separation (SA-neg, S-noft2 results). As discussed previously in Run 4 VE 1, the QCR variation (with modelled 2/3 ρk term) is able to predict a separation onset, even though the experiments do not indicate any. Heat flux levels on the flare are generally underpredicted and vary between solvers. Based on Run 4 and Run45, it appears that, regardless of the flow conditions, this specific SA-noft2-QCR-V model has a tendency to predict separation. Further runs would be required to confirm this behavior.

The k- ω type two-equation turbulence models in Figure 26 shows similar variability in separation onset to the single solver results with wide range of turbulence model types (Subsection

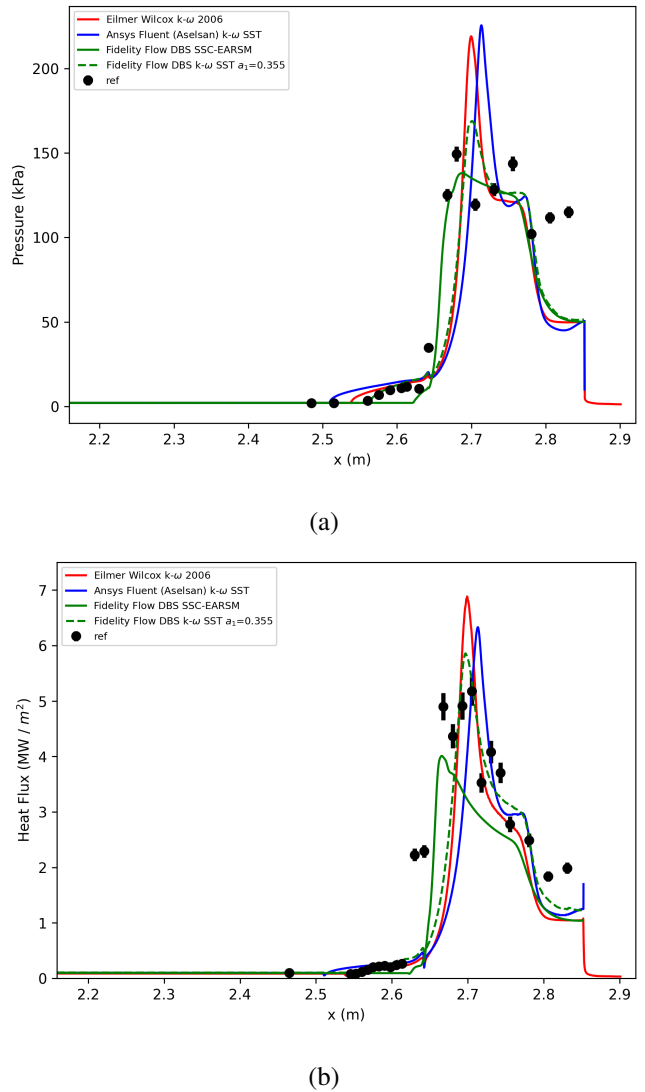


FIG. 20: Comparative predictions of pressure (a) and heat flux (b) Case 1 (Run 6).

Solver	Turbulence Model	x_{sep} (m)	p_{peak} (kPa)	$p_{peak,loc}$ (m)	q_{peak} ($MW/(m^2)$)	$q_{peak,loc}$ (m)
Eilmer	k- ω 2006	2.539	219.08	2.7	6.885	2.699
Ansys Fluent (Aselsan)	k- ω SST	2.51	225.57	2.713	6.33	2.713
Cadence Fidelity	Fi- SSC-EARSM	2.623	138.09	2.687	4.011	2.665
	k- ω SST al=0.355	2.565	168.94	2.701	5.858	2.697

TABLE XIV: Separation, peak values and associated location for run 6

V D). It must be noted that across the Runs presented in this work, the SU2 k- ω SST model variant doesn't predict a noticeable separation region. For this run condition, peak heat flux levels are not over-predicted and a consistent behavior between separation onset location and peak heat flux location is observed.

Finally, Figure 27 shows that all EARSM and RSM models

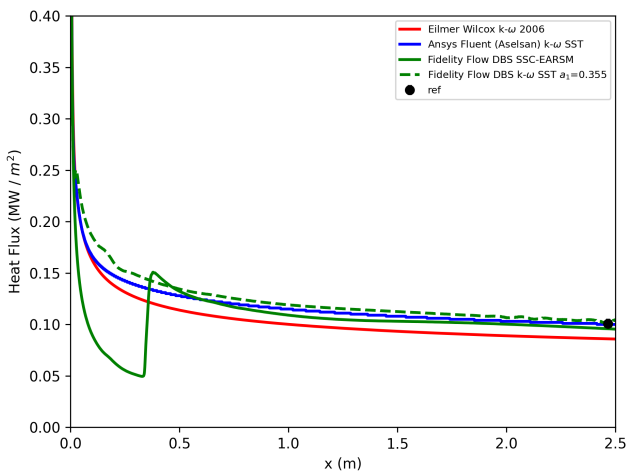


FIG. 21: Comparative predictions of heat flux on the cone for Case 1 (Run 6).

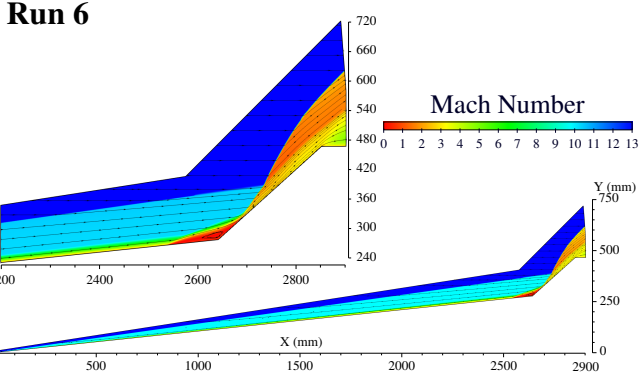


FIG. 22: Mach Number Color Map for Run 6, computed with Eilmer

considered predict a separation onset with the smallest found for the SSC-EARSM simulation. The peak pressure and heat flux behavior on the flare is analogous to the k- ω type two-equation turbulence models. Table XV and XVI quantifies the results for Run 45.

4. Run 28

For Run 28, predictions with k- ω type two-equation turbulence models were collected. Heat flux levels on the nose (Figure 29) are similarly predicted and within the range of experimental measurements. Note that for GASPEx, the numerical data was retrieved from³³, and the heat flux traces in this region were not available for this run and the subsequent runs. Similar separation onset is predicted by both Wilcox' k- ω 2006 models in Figure 28 but slight differences in pressure on the flare are observed. The influence of changing the a_1 coefficient from its default value of 0.31 to 0.355 in the k- ω SST model, as advised by⁵¹, is clearly visible in the separation. Similar behavior has been reported in³⁵ for such type

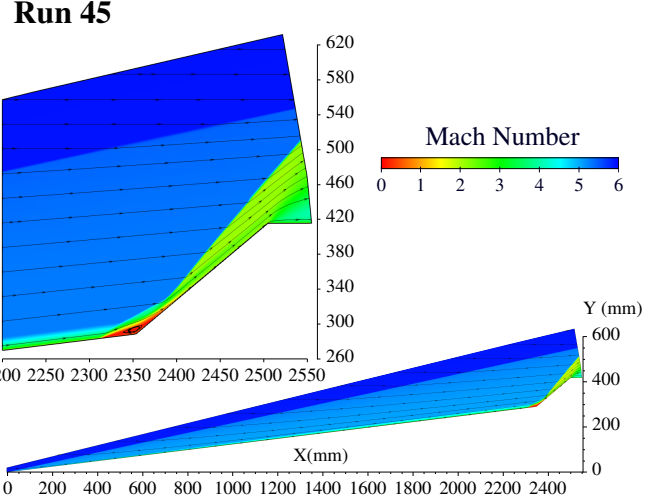


FIG. 23: Mach Number Color Map for Run 45, Computed with Eilmer

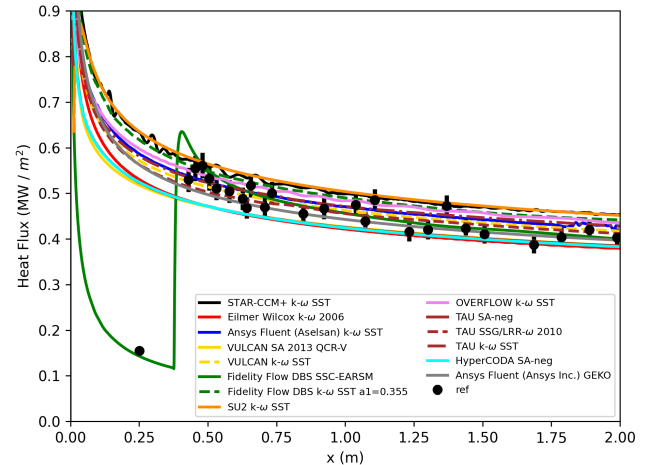
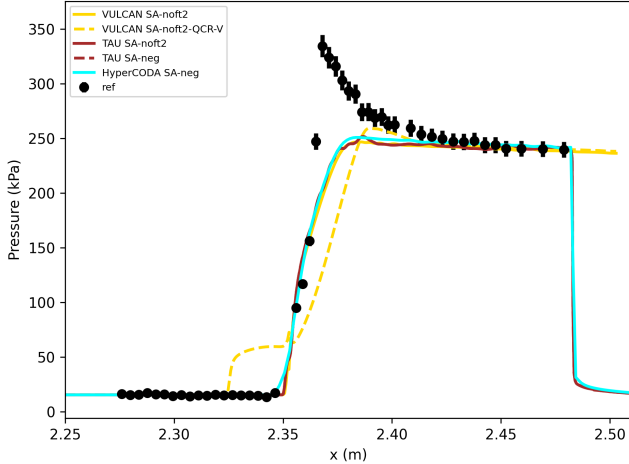
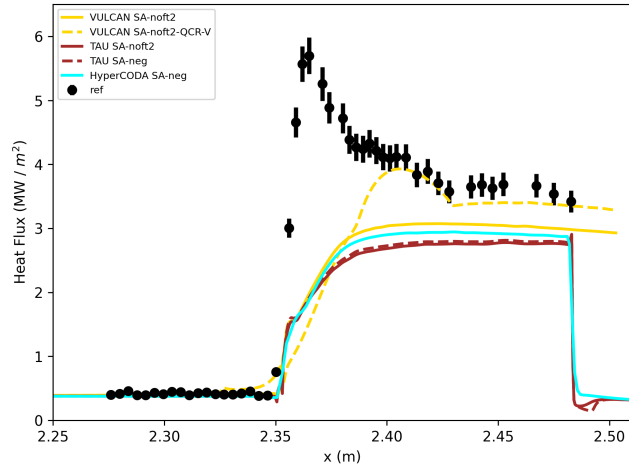


FIG. 24: Heat flux predicted by various solvers on the cone for Run 45

of setups and are in line with the specific study on this parameter by Georgiadis *et al.*⁵¹. The STAR-CCM+ prediction, also with $a_1 = 0.355$, predicts also a smaller separation bubble. SU2's k- ω SST does not predict a separation region which result in lower peak pressure and peak heat flux values. Experimental heat flux values on the flare are overpredicted by all CFD results, with higher overpredictions for the cases where separation is obtained. The GASPEx Wilcox' k- ω 2006 trace indicate an anomalous spike in heat flux on the flare which is linked to a jump in turbulent kinetic energy production (see also³³). A production limiter would most probably remove this behavior as indicated by the Eilmer results (Wilcox2006-klim-V). This spike is present in the GASPEx predictions for different flow conditions. A quantitative overview of the results is provided in Tables XVII and XVIII.



(a)

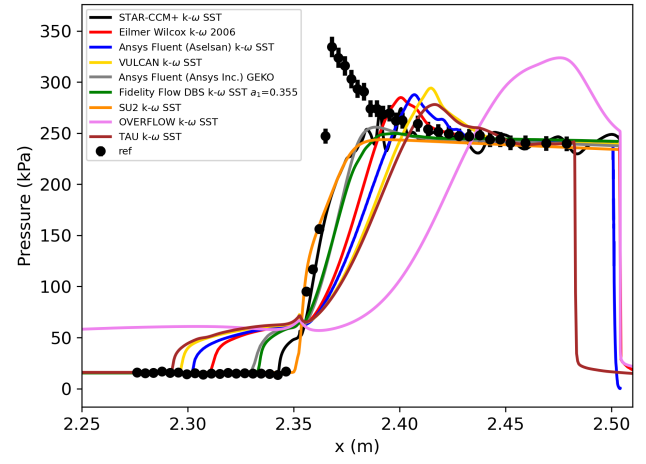


(b)

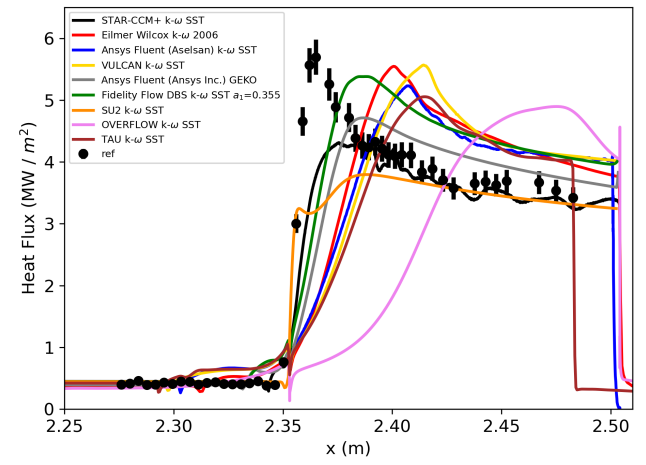
FIG. 25: Traces of wall (a) pressure and (b) heat flux obtained for Run 45 with one-equation turbulence models.

5. Run 34

Similarly to Run 28, participants provided wall pressure and heat flux traces with Wilcox' $k-\omega$ 2006 and Menter's SST model. Cone heat flux traces (Figure 31) are in close agreement with the experimental data after transition to turbulence. The Eilmer predictions are on the lower side, which has been observed for across all the run conditions in this work. The behavior is potentially linked to the Wilcox' $k-\omega$ 2006 model but this needs to be verified through comparison with the same turbulence model with another CFD solver. The same order (in axial position) of separation onset as in Run 28 is observed for the solvers in Figure 30 (a). A smaller separation is obtained with STAR-CCM+ (SST with use of QCR, $a_1=0.355$ and no M_t compressibility correction) compared to Wilcox' $k-\omega$ 2006. This was also observed in the previously discussed flow conditions. SU2 does not predict a separation.



(a)



(b)

FIG. 26: Traces of wall (a) pressure and (b) heat flux obtained for Run 45 with various two-equation turbulence models.

The heat flux prediction on the flare (Figure 30 (b)) is consistent with the separation behavior and separation shock reattachment point. A summary of the results is found in Tables XIX and XX.

6. Run 33

Run 33 has also only been predicted with two-equation type turbulence models. The heat flux on the cone (Figure 33) follows the trends of Run 28 and Run 34. In this run, a larger difference in separation onset between the solvers adopting Wilcox' $k-\omega$ 2006 model is found. The GEKO model's prediction are in closest agreement with the experimental pressure and heat flux traces on the cone and a portion of the flare (Figure 32). Run 33 has the lowest freestream total enthalpy

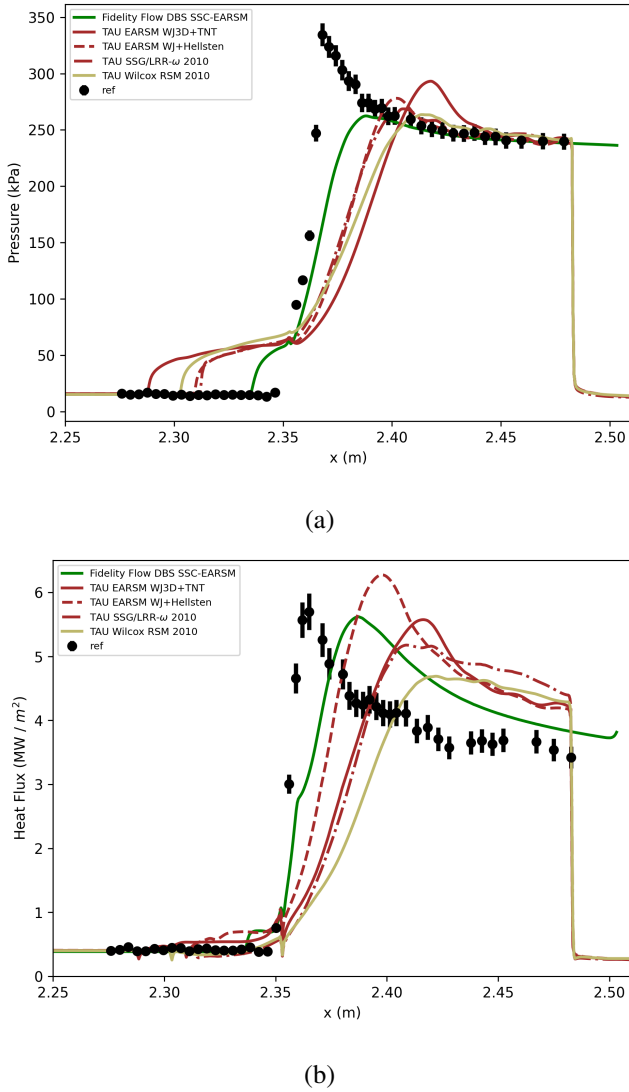


FIG. 27: Traces of wall (a) pressure and (b) heat flux obtained for Run 45 with EARSM and RSM turbulence model.

flow which explains the generally lower wall heat flux levels. Nevertheless, except for SU2 which predicts a very small separation region, the CFD does overpredict the experimental peak heat flux up to $\approx 50\%$ in relative terms (not accounting for the anomalous spike). Note that in Table XXII, as well as similar tables throughout this work, the anomalous spike in heat flux is setting the peak value for GASPEx.

7. Run 14

Run 14 has the second lowest (after Run 33) freestream total enthalpy. In this case, however, all CFD over-predicts the experimental cone heat flux as shown by Figure 35. This indicates a potential issue with the tabulated flow conditions in Table II which correspond to the freestream conditions pro-

Solver	Turbulence Model	pressure (kPa)	heat flux ($MW/(m^2)$)
STAR-CCM+	$k-\omega$ SST	132.95	2.18
Eilmer	$k-\omega$ 2006	133.02	2.405
Ansys Fluent (Aselsan)	$k-\omega$ SST	132.06	2.371
Cadence Fidelity	SSC-EARSM	133.9	2.544
	$k-\omega$ SST	131.66	2.59
TAU	EARSM WJ3D+TNT	126.28	2.304
	EARSM WJ+Hellsten	126.28	2.553
	SA-nofit2	127.91	1.512
	SA-neg	127.93	1.532
	SSG/LRR- ω 2010	126.62	2.258
	$k-\omega$ SST 2003	125.12	2.207
	Wilcox RSM 2010	126.2	2.039
	Menter BSL	126.16	1.99
	Wilcox $k-\omega$ 1988	125.95	2.085
	Wilcox $k-\omega$ + SST	125.95	2.059
HyperCODA	SA-neg	130.1	1.6
Ansys Fluent (Ansys Inc)	GEKO	131.3	2.291
SU2	$k-\omega$ SST	131.63	2.108
VULCAN	SA	132.32	1.727
	SA 2013 QCR-V	132.2	1.903
	$k-\omega$ SST	131.53	2.396
	$k-\omega$ SST-KL	131.47	2.344
	$k-\omega$ SST-V	131.44	2.305
	$k-\omega$ SST-V no 2/3 rho*k	131.65	2.323
OVERFLOW	$k-\omega$ SST	130.4	1.838

TABLE XV: Integrated wall quantities for run 45 . Values are scaled by $\int dx$.

vided by CUBRC online. As for Run 33, a difference in separation onset is found for the Wilcox' $k-\omega$ 2006 predictions. This behavior appears to happen consistently for the test conditions with freestream total enthalpy below 1 MJ/kg (see also Run 33 in VE 6 and Run 37 in VE 9). Peak pressure values on the flare are in close agreement with the experiment for the Wilcox' $k-\omega$ 2006 model as shown in Figure 34 (a). The GEKO results are consistent with Run 33, with good agreement on the cone and a portion of the flare except for the peak heat flux values (see in Figure 34 (b)). Relative to experimental values, peak heat flux overpredictions above 80 % are obtained with the CFD solvers which predict a separation. Integrated quantities are listed in Table XXIII and other quantities of interest in Table XXIV.

8. Run 41

For Run 41, the cone heat flux predicted with Wilcox' $k-\omega$ 2006 and Menter's SST are in relatively close agreement with experiments (Figure 37) with a slight overprediction by STAR-CCM+. For this case, the separation onset for both Wilcox' $k-\omega$ 2006 predictions is similar as well as peak pressure location and value (Figure 36 (a)). Slight variations in peak heat flux are found (Figure 36 (b)). Menter's SST (with STAR-CCM+) predicts a small separation bubble which also result in underprediction of the flare heat flux. All results can be found in Tables XXV and XXVI.

9. Run 37

For Run 37, the various two-equation turbulence models predict a larger separation region than experimentally observed (Figure 38 (a)). Relative differences among the solvers

Solver	Turbulence Model	x_{sep} (m)	p_{peak} (kPa)	$p_{peak,loc}$ (m)	q_{peak} ($MW/(m^2)$)	$q_{peak,loc}$ (m)
STAR-CCM+	k- ω SST	2.343	274.17	2.401	4.368	2.391
Eilmer	k- ω 2006	2.312	284.88	2.401	5.546	2.401
Ansys Fluent	k- ω SST (Aselsan)	2.303	287.65	2.407	5.23	2.407
Cadence	Fi- ω SSC-EARSM	2.336	262.44	2.388	5.619	2.387
	k- ω SST	2.334	249.79	2.398	5.381	2.388
TAU	EARSM WJ3D+TNT	2.289	293.22	2.418	5.573	2.416
	EARSM WJ+Hellsten	2.31	278.06	2.402	6.273	2.398
	SA-noft2	2.35	251.57	2.387	2.872	2.483
	SA-neg	2.35	251.7	2.387	2.907	2.483
	SSG/LRR- ω 2010	2.312	268.66	2.405	5.176	2.409
	k- ω SST 2003	2.293	278.02	2.417	5.054	2.415
	Wilcox RSM 2010	2.303	263.58	2.414	4.689	2.422
	Menter BSL	2.348	246.17	2.39	3.735	2.386
	Wilcox k- ω 1988	2.35	245.12	2.389	3.9	2.389
	Wilcox k- ω + SST	2.35	244.98	2.389	3.805	2.388
HyperCoda	SA-neg	2.348	250.89	2.384	2.944	2.43
Ansys Fluent	GEKO (Ansys Inc)	2.333	255.86	2.389	4.712	2.387
SU2	k- ω SST	2.35	243.66	2.393	3.795	2.388
VULCAN	SA	2.349	246.71	2.386	3.073	2.423
	SA 2013 QCR-V	2.325	259.35	2.39	3.928	2.406
	k- ω SST	2.297	294.16	2.415	5.568	2.414
	k- ω SST-KL	2.29	294.6	2.421	5.386	2.421
	k- ω SST-V	2.284	292.94	2.426	5.243	2.425
	k- ω SST-V no rho*k	2.303	287.37	2.407	5.002	2.407
OVERFLOW	k- ω SST	2.235	323.71	2.476	4.896	2.475

TABLE XVI: Separation, peak values and associated location for run 45

Solver	Turbulence Model	pressure (kPa)	heat flux ($MW/(m^2)$)
GASpex	k- ω 2006	111.12	1.225
Eilmer	k- ω 2006	105.42	1.144
STAR-CCM+	k- ω SST	105.52	1.21
Ansys Fluent (Aselsan)	k- ω SST 2T a1=0.31	104.59	1.188
	k- ω SST a1=0.31	104.53	1.173
	k- ω SST a1=0.355	104.74	1.208
SU2	k- ω SST	105.0	1.059

TABLE XVII: Integrated wall quantities for run 28 . Values are scaled by $\int dx$.

are small. Peak values for both Wilcox' k- ω 2006 traces are similar with slight variations in location linked to differences in separation behavior. The cone heat flux (Figure 39) is somewhat underpredicted by Eilmer for this run. Tables XXVII and XXVIII provides a quantitative overview of these predictions.

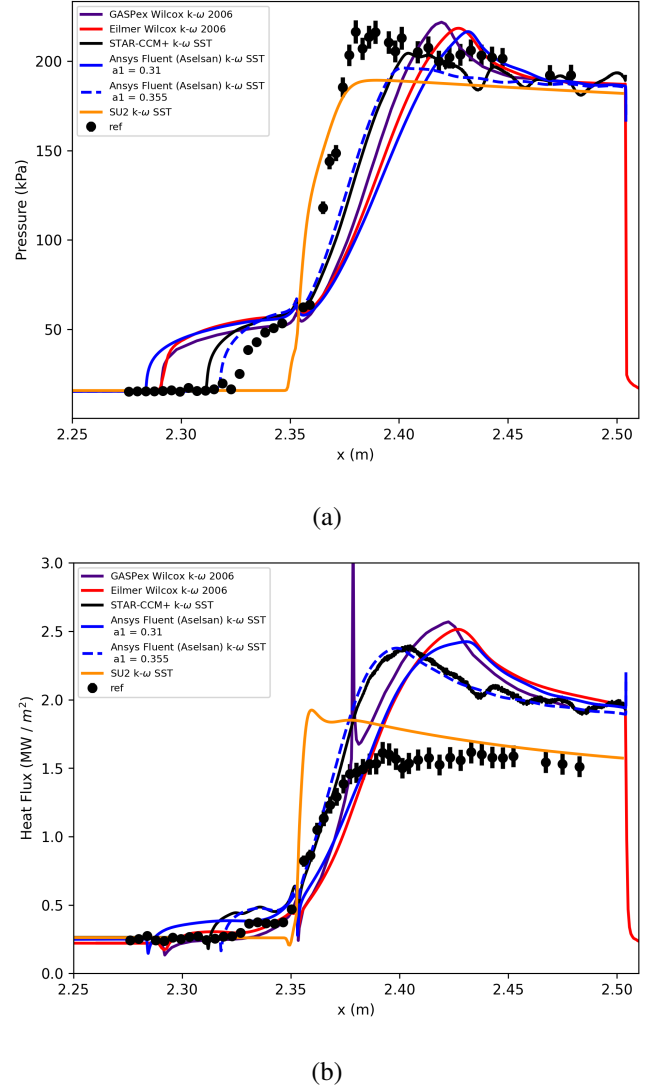


FIG. 28: Comparative predictions of pressure (a) and heat flux (b) Case 2 (Run 28).

Solver	Turbulence Model	x_{sep} (m)	p_{peak} (kPa)	$p_{peak,loc}$ (m)	q_{peak} ($MW/(m^2)$)	$q_{peak,loc}$ (m)
GASpex	k- ω 2006	2.291	221.89	2.42	3.314	2.379
Eilmer	k- ω 2006	2.292	218.48	2.427	2.515	2.427
STAR-CCM+	k- ω SST	2.312	204.51	2.404	2.396	2.405
Ansys Fluent (Aselsan)	k- ω SST 2T a1=0.31	2.277	215.95	2.438	2.449	2.436
	k- ω SST a1=0.31	2.284	216.6	2.432	2.425	2.431
	k- ω SST a1=0.355	2.318	196.27	2.402	2.377	2.399
SU2	k- ω SST	2.35	189.39	2.39	1.925	2.359

TABLE XVIII: Separation, peak values and associated location for run 28

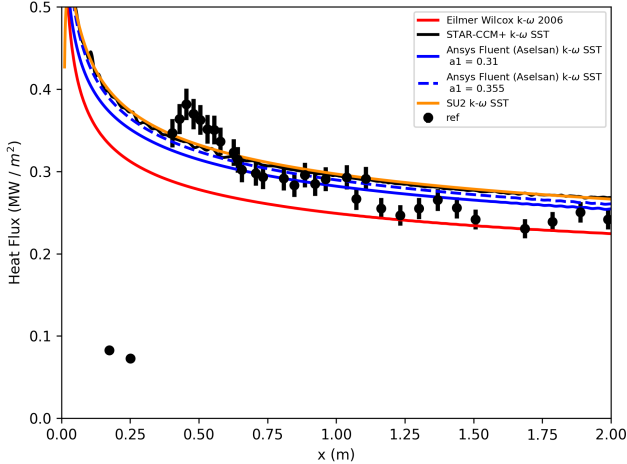


FIG. 29: Comparative predictions of heat flux on the cone for Case 2 (Run 28).

Solver	Turbulence Model	pressure (kPa)	heat flux ($\text{MW}/(\text{m}^2)$)
GASPex	k- ω 2006	65.29	0.98
Eilmer	k- ω 2006	62.25	0.916
STAR-CCM+ k- ω SST		62.52	0.929
SU2	k- ω SST	61.08	0.82

TABLE XIX: Integrated wall quantities for run 34 . Values are scaled by $\int dx$.

Solver	Turbulence Model	x_{sep} (m)	p_{peak} (kPa)	$p_{peak,loc}$ (m)	q_{peak} ($\text{MW}/(\text{m}^2)$)	$q_{peak,loc}$ (m)
GASPex	k- ω 2006	2.295	140.78	2.408	3.235	2.375
Eilmer	k- ω 2006	2.293	140.49	2.415	2.248	2.414
STAR-CCM+ k- ω SST		2.316	128.4	2.406	1.986	2.394
SU2	k- ω SST	2.352	113.8	2.394	1.529	2.386

TABLE XX: Separation, peak values and associated location for run 34

Solver	Turbulence Model	pressure (kPa)	heat flux ($\text{MW}/(\text{m}^2)$)
GASPex	k- ω 2006	22.39	0.076
Eilmer	k- ω 2006	22.67	0.067
STAR-CCM+ k- ω SST		22.89	0.085
Ansys Fluent (Ansys Inc) GEKO		22.35	0.073
SU2	k- ω SST	22.1	0.065

TABLE XXI: Integrated wall quantities for run 33 . Values are scaled by $\int dx$.

Solver	Turbulence Model	x_{sep} (m)	p_{peak} (kPa)	$p_{peak,loc}$ (m)	q_{peak} ($\text{MW}/(\text{m}^2)$)	$q_{peak,loc}$ (m)
GASPex	k- ω 2006	2.259	55.18	2.426	0.244	2.383
Eilmer	k- ω 2006	2.242	54.7	2.448	0.174	2.445
STAR-CCM+ k- ω SST		2.251	51.57	2.445	0.189	2.443
Ansys Fluent GEKO (Ansys Inc)		2.297	50.76	2.409	0.183	2.407
SU2	k- ω SST	2.347	41.61	2.392	0.134	2.378

TABLE XXII: Separation, peak values and associated location for run 33

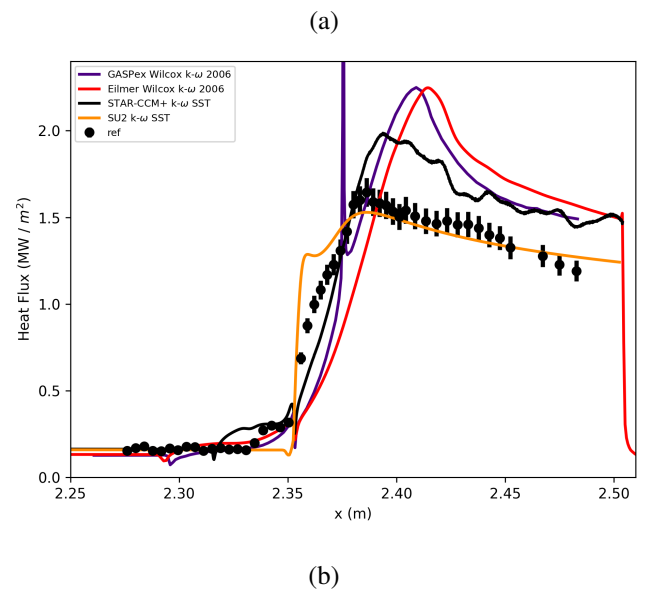
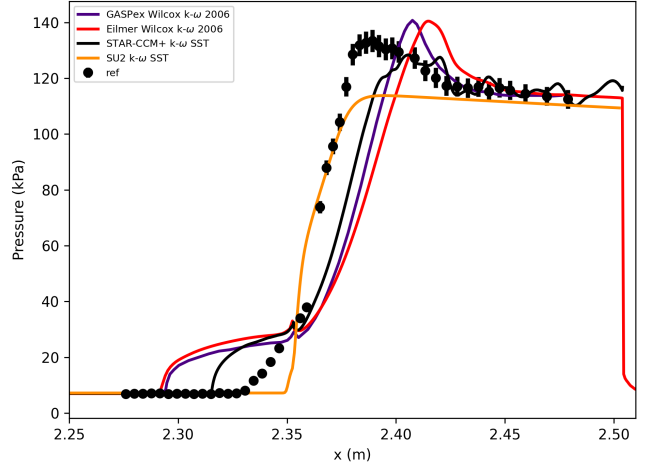


FIG. 30: Comparative predictions of pressure (a) and heat flux (b) Case 2 (Run 34).

Solver	Turbulence Model	pressure (kPa)	heat flux ($\text{MW}/(\text{m}^2)$)
GASPex	k- ω 2006	31.12	0.253
Eilmer	k- ω 2006	29.75	0.231
STAR-CCM+ k- ω SST		29.98	0.249
Ansys Fluent (Ansys Inc) GEKO		29.23	0.23
SU2	k- ω SST	28.54	0.2

TABLE XXIII: Integrated wall quantities for run 14 . Values are scaled by $\int dx$.

Solver	Turbulence Model	x_{sep} (m)	p_{peak} (kPa)	$p_{peak,loc}$ (m)	q_{peak} ($\text{MW}/(\text{m}^2)$)	$q_{peak,loc}$ (m)
GASPex	k- ω 2006	2.278	75.24	2.41	0.73	2.377
Eilmer	k- ω 2006	2.265	76.77	2.425	0.651	2.425
STAR-CCM+ k- ω SST		2.279	70.17	2.422	0.604	2.42
Ansys Fluent GEKO (Ansys Inc)		2.308	66.97	2.399	0.592	2.398
SU2	k- ω SST	2.35	54.72	2.394	0.401	2.383

TABLE XXIV: Separation, peak values and associated location for run 14

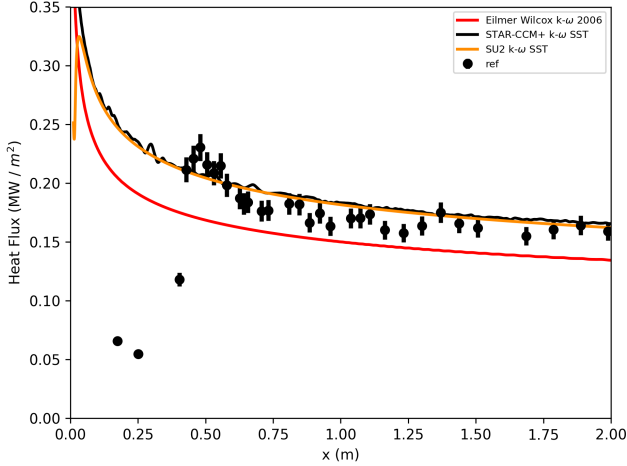


FIG. 31: Comparative predictions of heat flux on the cone for Case 2 (Run 34).

Solver	Turbulence Model	pressure (kPa)	heat flux ($\text{MW}/(\text{m}^2)$)
GASPex	k- ω 2006	42.3	1.324
Eilmer	k- ω 2006	40.25	1.231
STAR-CCM+ k- ω SST		40.33	1.033

TABLE XXV: Integrated wall quantities for run 41 . Values are scaled by $\int dx$.

Solver	Turbulence Model	x_{sep} (m)	p_{peak} (kPa)	$p_{peak,loc}$ (m)	q_{peak} ($\text{MW}/(\text{m}^2)$)	$q_{peak,loc}$ (m)
GASPex	k- ω 2006	2.305	93.56	2.394	4.992	2.371
Eilmer	k- ω 2006	2.307	95.24	2.395	3.506	2.394
STAR-CCM+ k- ω SST		2.345	84.78	2.409	2.005	2.393

TABLE XXVI: Separation, peak values and associated location for run 41

Solver	Turbulence Model	pressure (kPa)	heat flux ($\text{MW}/(\text{m}^2)$)
GASPex	k- ω 2006	29.64	0.319
Eilmer	k- ω 2006	28.61	0.296
STAR-CCM+ k- ω SST		28.85	0.3

TABLE XXVII: Integrated wall quantities for run 37 . Values are scaled by $\int dx$.

Solver	Turbulence Model	x_{sep} (m)	p_{peak} (kPa)	$p_{peak,loc}$ (m)	q_{peak} ($\text{MW}/(\text{m}^2)$)	$q_{peak,loc}$ (m)
GASPex	k- ω 2006	2.284	75.1	2.403	0.914	2.403
Eilmer	k- ω 2006	2.27	77.98	2.417	0.9	2.416
STAR-CCM+ k- ω SST		2.288	68.34	2.415	0.753	2.407

TABLE XXVIII: Separation, peak values and associated location for run 37

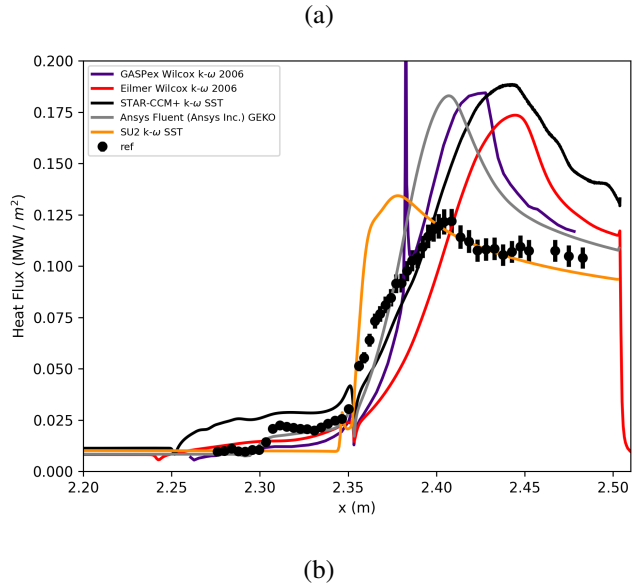
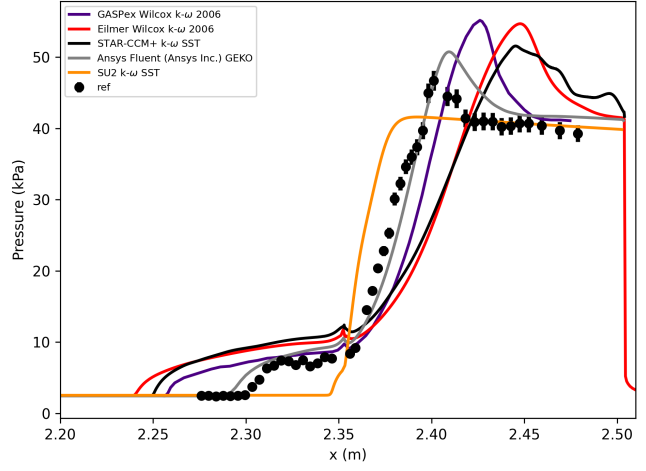


FIG. 32: Comparative predictions of pressure (a) and heat flux (b) Case 2 (Run 33).

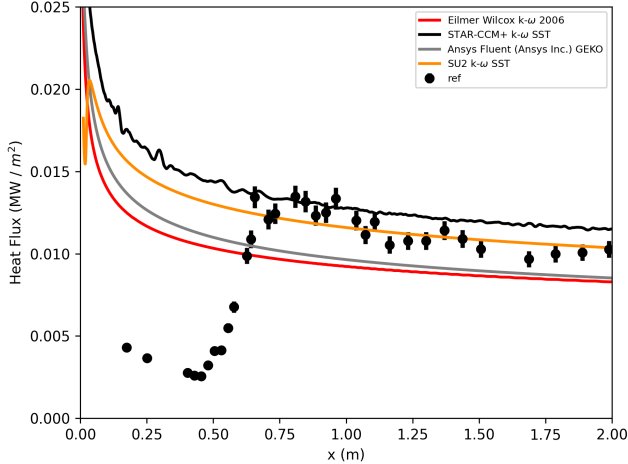
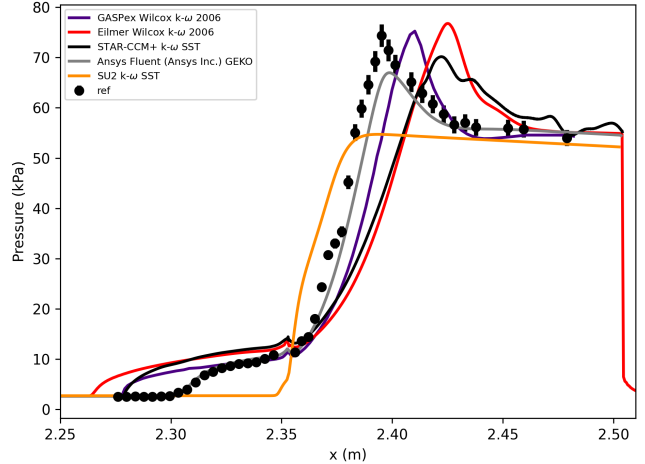
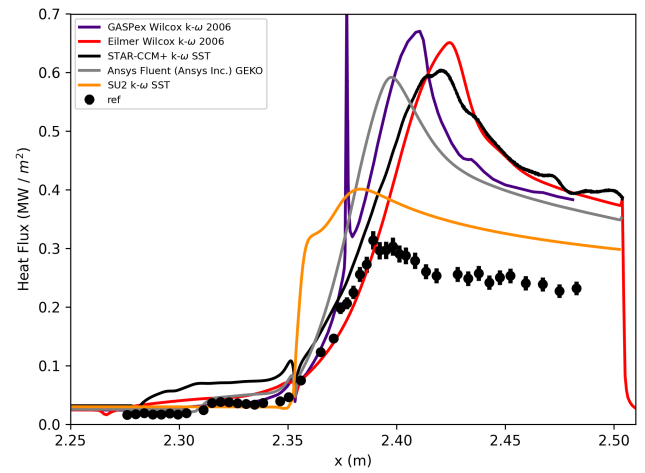


FIG. 33: Comparative predictions of heat flux on the cone for Case 2 (Run 33).



(a)



(b)

FIG. 34: Comparative predictions of pressure (a) and heat flux (b) Case 2 (Run 14).

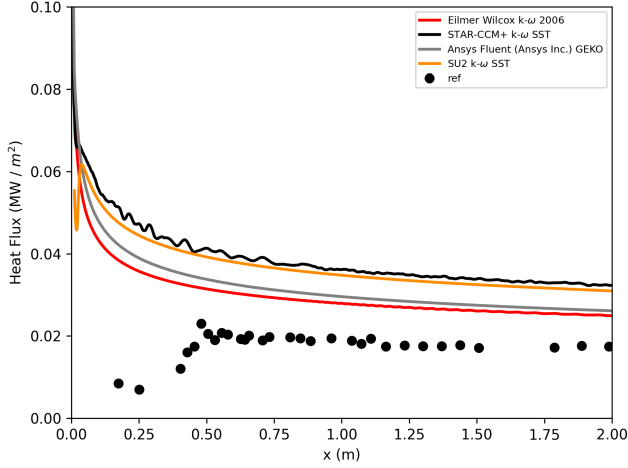


FIG. 35: Comparative predictions of heat flux on the cone for Case 2 (Run 14).

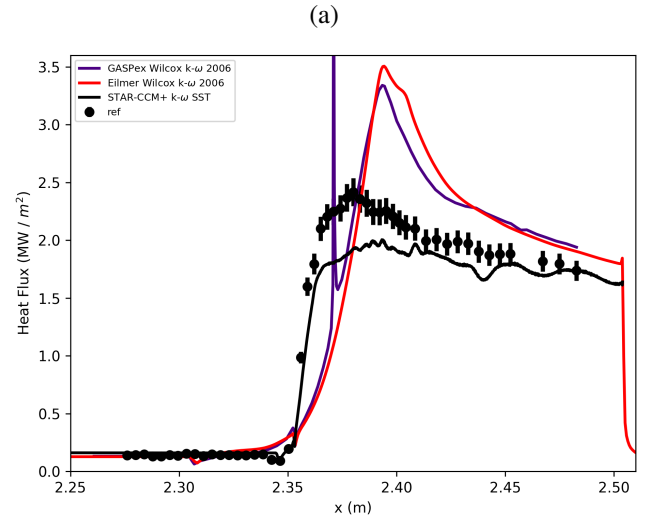
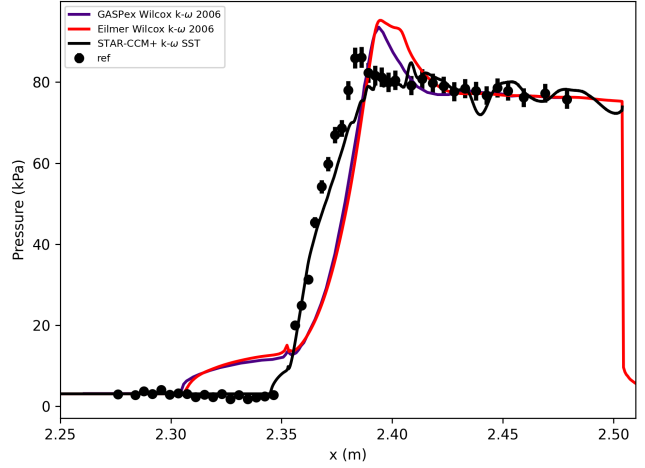


FIG. 36: Comparative predictions of pressure (a) and heat flux (b) Case 2 (Run 41).

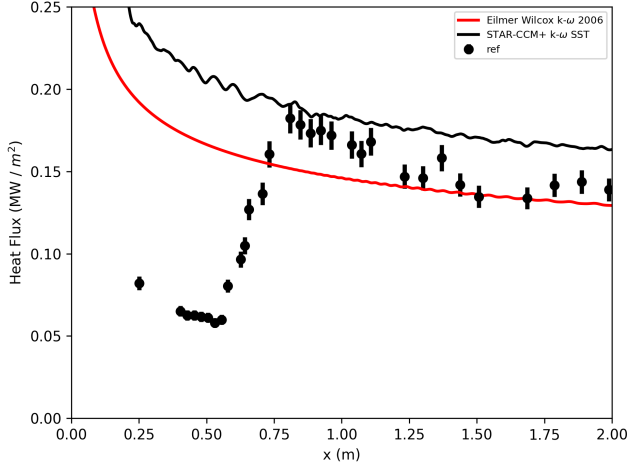
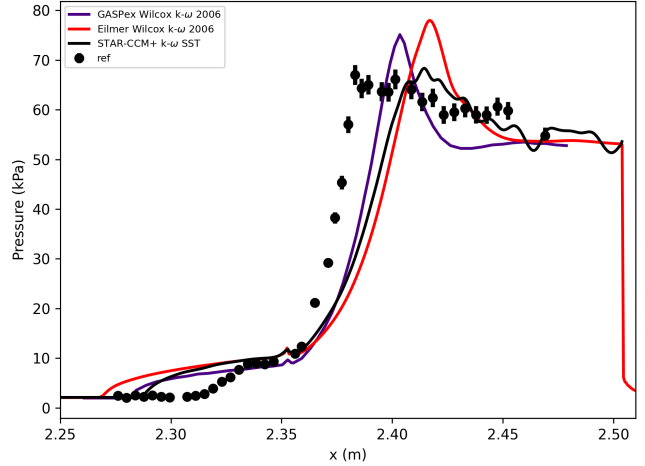
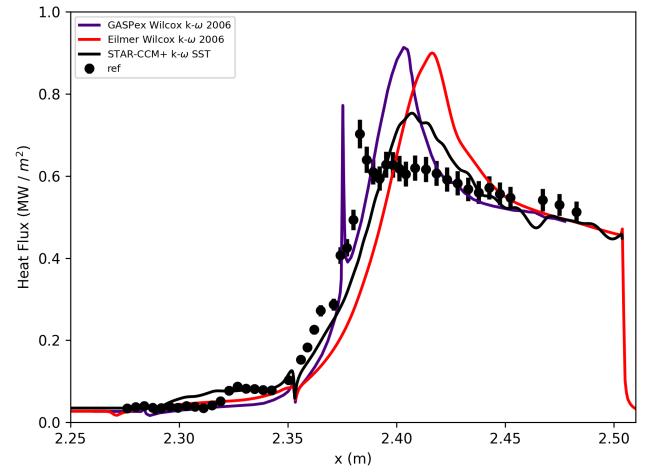


FIG. 37: Comparative predictions of heat flux on the cone for Case 2 (Run 41).



(a)



(b)

FIG. 38: Comparative predictions of pressure (a) and heat flux (b) Case 2 (Run 37).

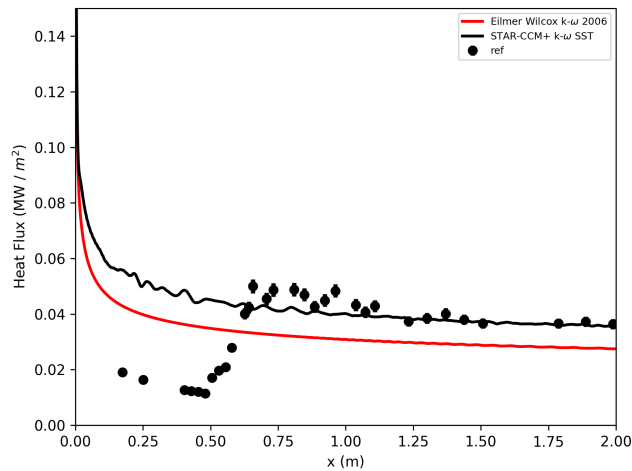


FIG. 39: Comparative predictions of heat flux on the cone for Case 2 (Run 37).

10. Overall variability

Table XXIX summarizes the absolute variations in separation onset, peak values for wall pressure and -heat flux as well as their axial location for all the test conditions. All turbulence models are considered to extract these values. In terms of separation onset, the largest discrepancy is found for Run 4 of the 6/42 cone-flare geometry with separation onsets predicted over a range of ≈ 23 cm from the cone-flare junction. This large variation is also found in the peak pressure (82kPa) and - heat flux (2.8 MW/m^2) values. As indicated in Table VI, previous simulations of Run 4 have also resulted in large absolute differences which were higher in terms of separation onset and peak values location, but lower in terms of peak values.

For the 7/40 cone-flare geometry, the largest variations in peak heat flux are found for Run 45 and Run 41 with differences up to 3.4 MW/m^2 and 3 MW/m^2 , respectively. These conditions represent the highest freestream total enthalpies for this case. CFD predictions from the literature (Table XXIX) also indicate largest absolute variations between codes for those conditions. Currently, smaller differences in separation onset are shown for Runs 41 and Run 37 which are the runs with the least amount of collected CFD predictions. In comparison to predictions found in the literature (see Table XXIX), larger absolute variations in separation onset are found in the present work except for Runs 41 and 37.

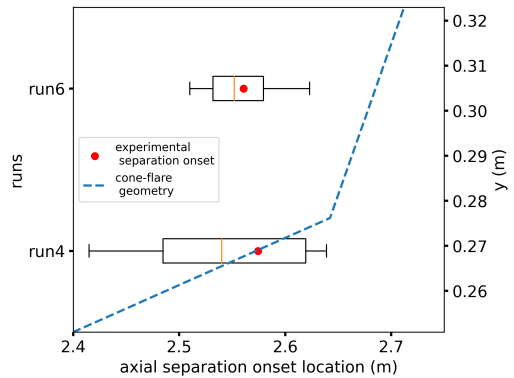
Case	Run #	Δ separation onset (cm)	Δ pressure location (cm)	Δ Peak pressure (kPa)	Δ Peak heat flux location (cm)	Δ Peak heat flux (MW/m ²)
6/42	4	22.5	8.1	81.7	8.2	2.793
	6	11.3	2.6	87.48	4.8	2.874
7/40	45	11.5	9.2	80.05	9.7	3.401
	28	7.3	4.8	32.5	7.7	1.389
	34	5.9	2.1	26.98	3.9	1.706
	33	10.5	5.6	13.57	6.7	0.11
	14	8.5	3.1	22.05	4.8	0.329
	41	4.0	1.5	10.46	2.3	2.987
	37	1.8	1.4	9.64	1.3	0.161

TABLE XXIX: Absolute variations in predictions of separation, peak values and associated location for all present runs.

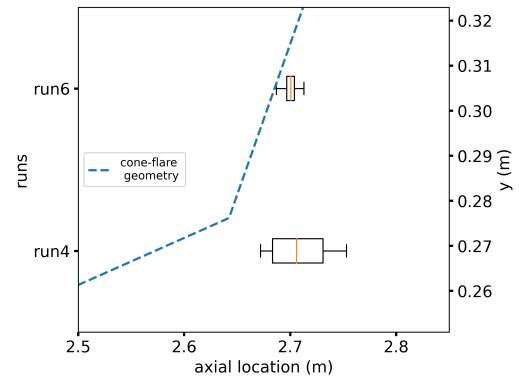
Figure 40 illustrates the predictive variability in separation onset between the current runs, as well as the experimental separation onset, through a box plot representation. Note that the statistics for some of the runs are obtained from a small number of samples. Overall, the tendency of the turbulence models is to overpredict the extend of the separation region, as shown by the median being located in front of the experimental values. Except for Runs 37 and Run 41, all cases show that the experimental separation onset is within the predictive bounds. As observed in Table XXIX, the variability is typically on the order of 2 - 12 cm for the 7/40

cone-flare geometry. Moreover, for the latter setup, most of the conditions are characterized by results with little or no separation to larger separations, depending on the solver / turbulence model combination. From an engineering point of view, this is extremely undesirable, and no robustness in predictive capability can be obtained. Two of the conditions, Run 41 and Run 45, show little to no separation. The only commonality between these conditions is that they are at a somewhat higher freestream total enthalpy than the others (Run 45 = 1.671 MJ/kg , Run 41 = 2.113 MJ/kg). It is not possible to comment on why these conditions do not separate like the others based on the available experimental information. In all conditions of this setup, the leading edge shock does not impinge on the flare. In absolute values, separation onset locations in the literature for Run 4 range between 2.18 and 2.57 (see Table IV based on 3 CFD predictions). Presently, the separation locations for the same run are closer to the flare, starting at $x \approx 2.4 \text{ m}$. In Run 45, the current observation range is more extended than in the literature, with a starting separation onset around 2.23 m (2.28 in literature). The same can be concluded for Runs 28 and 14. Note that for Run 33, the separation onset for some of the prior CFD predictions is unclear but appears to be upstream of 2.26 m. For Runs 37 and 41, the range of absolute values presented in Figure 40 (b) is contained within the range found in the literature.

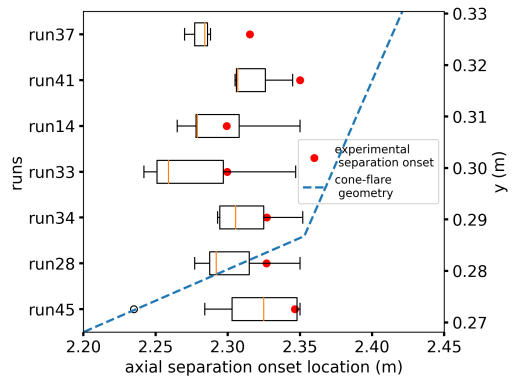
Figures 41 to 44 illustrates the variability of the other quantities from Table XXIX. Peak pressure (Figure 41 (a)) and heat flux (Figure 42 (a)) locations on the flare occur more upstream in Run 4 than previous predictions from the literature which extend up to $x \approx 2.85 \text{ m}$. For the second cone-flare geometry, the ranges for the same parameters (Figures 43 and 44) are very similar to what has been observed in the literature. In terms of peak pressures, the scatter in present results for Run 4 covers a larger range than in Table IV. The peak heat flux results for the same run does not predict as high a value as in the literature but extends the lower predictive bound. In Runs 45, 28 and 33 a larger array of peak pressures are presently obtained. A lower pressure bound extension in the order of 5 hPa is obtained for Run 33 while a general shift to higher values is seen for the remaining runs. Regarding the heat flux, all of the 7/40 cone-flare runs predict a higher minimum peak value as well as higher maximum peak values.



(a)

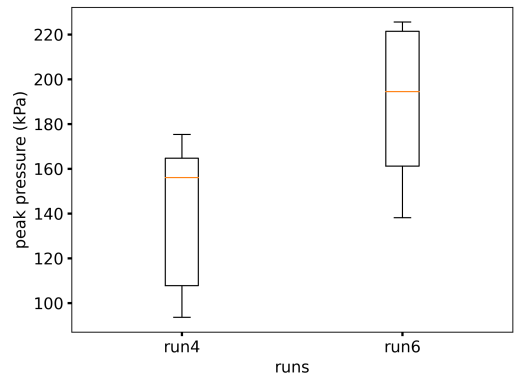


(a)



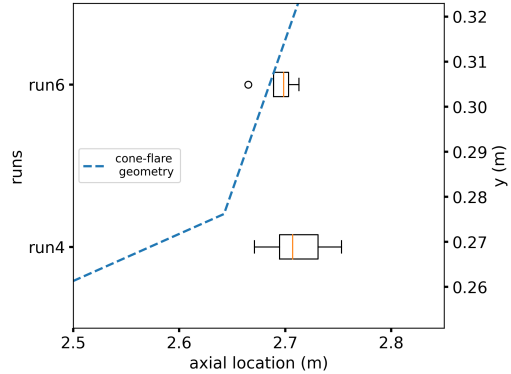
(b)

FIG. 40: Box plot of CFD predictions for (a) Case 1 and (b) Case 2. Empty circles represent outliers.

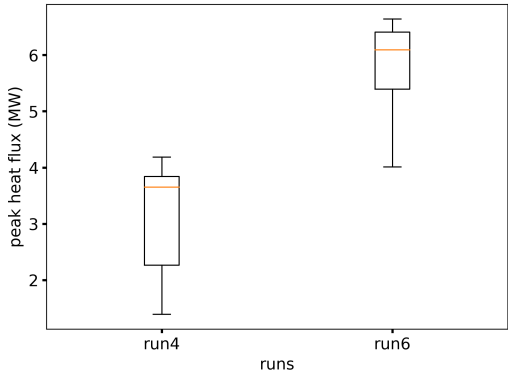


(b)

FIG. 41: Box plot for (a) peak value and (b) peak location of the pressure CFD predictions for Case 1. Empty circles represent outliers.

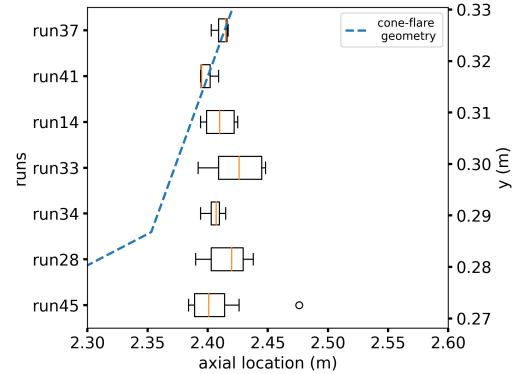


(a)

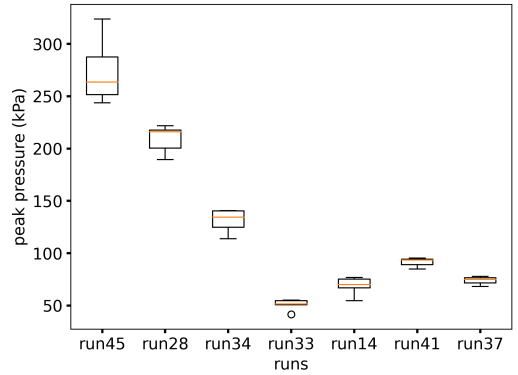


(b)

FIG. 42: Box plot for (a) peak value and (b) peak location of the heat flux CFD predictions for Case 1. Empty circles represent outliers.

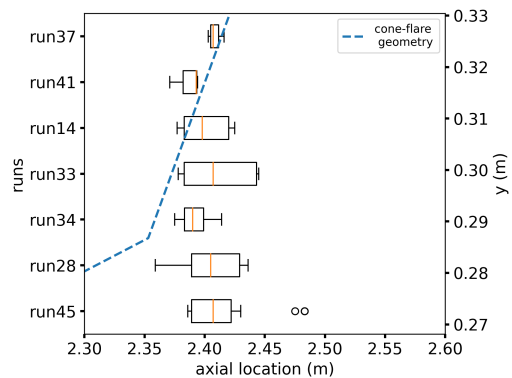


(a)

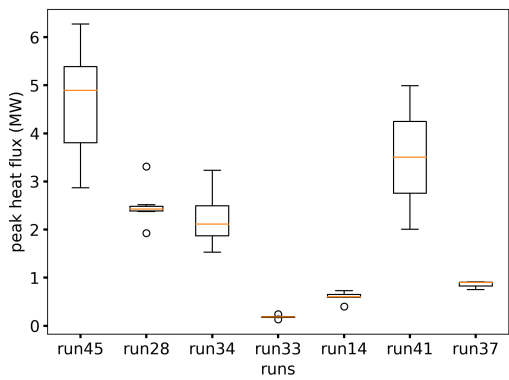


(b)

FIG. 43: Box plot for (a) peak value and (b) peak location of the pressure CFD predictions for Case 2. Empty circles represent outliers.



(a)



(b)

FIG. 44: Box plot for (a) peak value and (b) peak location of the heat flux CFD predictions for Case 2. Empty circles represent outliers.

VI. CONCLUSIONS

A. Conclusions

In this work, an extensive review of the literature on RANS simulations of hypersonic turbulent flow over sharp cone-flares has been performed. Numerical studies of such geometries have typically been motivated by CFD code validations and have been popular in (blind) code-to-code comparisons. The axi-symmetric configuration allows for the isolated study of shock wave turbulent boundary layer interactions with cross-flow effects. The large cone ensures that a turbulent boundary layer develops prior to the cone-flare junction. Multiple sets of experimental data are publicly available for such geometries with different cone and flare angles. Measurements include pressure and heat flux traces along the wall as well as Schlieren visualizations. Accurate and reliable predictions for sharp cone-flare geometries, as well as other similar hypersonic canonical configurations, are known to be challenging for CFD codes and RANS methods. Simulations typically fail in correctly predicting boundary layer separation and strongly overpredict the heat flux on the flare. The various historical developments of RANS modelling, relevant to these hypersonics configurations, have been discussed. These developments include various compressibility corrections and additional modelling terms based on shock-turbulence physics from canonical DNS studies. Unfortunately, the need for case-dependent tuning is typically reported in the literature. A promising approach with regard to improved predictions of turbulent shock wave boundary layer interactions is the variation of the turbulent Prandtl number. It is typically set as a constant, but it does vary across shock waves and accounting for this fact has resulted in less over-predictions of heat flux levels on the flare. However, the latter modelling strategy has not yet been adopted in the larger hypersonic RANS community.

In general, significant variations in the predictive capability of CFD codes for hypersonic turbulent large cone-flare geometries have been observed in the literature. As part of the AVT-352 on hypersonic turbulence, we wish to assess the current uncertainty in simulating such test cases. In this work, we selected two cone-flare geometries, available in the literature, for which experimental measurements have been collected in the CUBRC facilities at various flow conditions.

In terms of computational requirements, the present exercise has indicated the need to rely on very fine grids, despite the two-dimensional character of the flow allowing the use of an axi-symmetric setup. This limitation, which translates into high CPU costs (for such a simple geometry), is driven by the need to accurately predict the thermal loading.

Regarding the predictions, a large scatter has also been observed in this work. For the first setup, where the leading edge shock impinges the flare due to the high freestream Mach number, separation onset variations between 11 and 23 cm are obtained. This includes predictions with variations of Spalart-Almaras, $k-\omega$ and EARSM type turbulence models. Differences in peak heat flux and peak pressures up to 3.4 MW/m^2

and 90 kPa , respectively, are observed. For the second geometry, where no leading edge shock impingement is observed, differences in separation onset between codes smaller than 12 cm are seen. In terms of peak heat flux and pressure values, the variability in the predictions is more dependent on the test condition. Smaller variations for the former parameter are on the order $0.1\text{--}0.5 \text{ MW/m}^2$, while large variations range between $1\text{--}4 \text{ MW/m}^2$. In comparison to previously reported CFD simulations of the same setups, similar variations (predictive range) in location of the peak heat flux and pressure on the flare are found. Differences in peak values are however found with, for instance, a shift of the peak heat flux bounds to higher values for all runs of the 7/40 degree cone-flare setup.

In most of the cases, experimentally documented separation onset locations are found within the predictive ranges. The predictive behavior of the turbulence models could not be linked to the variations in freestream total enthalpy. The peak heat flux and pressure variability is a general problem if one has to rely on RANS CFD for design. The present work has shown that, depending on the adopted turbulence model, differences of several orders of magnitude can be obtained. The latter is strongly linked to the ability to adequately predict the separation onset, but it is not limited to this. In most of the test conditions, it was possible to obtain both a limited-to-no separated state or a separated state. A characteristic spike in heat flux is often found, which appears to be much higher than the experimental values. As stated above, some work from the literature seems to indicate that this over-prediction is linked to the turbulent Prandtl number. Unfortunately, none of the authors had a variable turbulent Prandtl number model readily available in their solver to simulate. One of the authors (see IV G) explored the use of an algebraic expression to vary the turbulent Prandtl number as a function of the laminar Prandtl number. This specific expression, derived based on DNS of channel flows, does have a minimal impact on the results of the current hypersonic setups. The probable explanation for this is the fact that the expression hasn't been derived based on shock wave turbulence interaction physics, unlike the work of Roy *et al.*⁶⁸, and does therefore not address the key changes in Pr_t across shocks.

With regard to the turbulence model behavior, it is difficult to provide conclusions. One of the reasons for this is that, in spite of having similar families of turbulence models (e.g. $k-\omega$ SST), variations of the exact models are found for the various solvers. As pointed out in the conclusions of V A, even based on the literature, the behavior of a turbulence model cannot clearly be established due to a general lack of precise information on the version of a turbulence model, potential changes in modeling constants as well as other associated settings. A consistent behavior presently observed (as well as in previous work in the literature), is the general inability of standard Spalart-Allmaras turbulence models to predict corner separation. However, the SA-noft2-QCR-V version appears to consistently predict a separation onset, a behavior linked to a modeled $2/3 \rho k$ term (see also V A). With respect to the two-equation $k-\omega$ SST model, the impact of changing the a_1 coefficient from its default value of 0.31 to 0.355 results in

a reduction in separation bubble size which is in accordance with the expected behavior from the literature. Among the turbulence models, the SSC-EARSM appears to consistently predict smaller separation bubbles as well as smaller peak pressure values on the flare which are in closer agreement with experimental measurements.

B. Outlook

RANS is, and probably will remain for some time, the principal tool used by engineers in various aerospace designs. Although much of the current research focus has shifted towards scale-resolving simulations, improving RANS modelling (if possible) still has value. Scale-resolving methods play a key role in improving our understanding of physical phenomena and can therefore be relied on to push forward RANS models. This is even more valid in hypersonic flows where experiments are expensive and have limited run times. Moreover, the idea of certification by simulations, which has been around for some years now, will require an increased robustness of the computational methods adopted in design, including uncertainty quantification. The herein presented exercise demonstrates how challenging such a strategy could be in shock-dominated (hypersonic) flows.

Concurrent to the present work, an extensive report detailing the grid independence as well as providing more information on the simulation strategy and convergence evaluation has been prepared as part of the NATO AVT 352. From a reproducibility point of view, this due diligence should be performed and reported by any CFD work. Unfortunately, this is often not found in published research papers which is understandable if one wishes to keep the work succinct. Nevertheless, small habits could be adopted that would limit this issue. A simple starting habit of upcoming research should be a correct referencing, which is often not found, to the turbulence models and variations used. It is advised to follow the naming convention provided by the NASA turbulence modelling resource website⁸⁷. Adopting this habit is a first step towards reproducibility of simulation results.

Another point of interest could be to adopt different grid related strategies. From a practical engineering point of view, three-dimensional geometries could result in massive cell counts for hypersonic flows. In such cases, strategies relying on adaptive or static (metric based) mesh refinement could significantly reduce the CPU cost and improve predictive capability through grid alignment with shock waves. For illustration, presently, the bow shock adaptation capability of VULCAN-CFD was used which does exactly that. Ansys Fluent (Aselsan) simulations did, for instance, consider static mesh refinement through a pressure gradient metric for one of the simulated cases. Such type of methods should be explored more often in canonical test cases and CFD code-to-code comparisons. Hypersonic wall modelling could be another aspect that could help reduce the overall computational costs of RANS-based simulations. The present effort highlighted one important shortcoming in our current approach towards wall-modelling, namely that we need wall models that are gener-

alizable to complex flow conditions. The relatively high CPU cost was driven by the high-resolution requirement at the reattachment point. Yet, it is exactly at this location that many of the underlying wall modelling assumptions break down (e.g. quasi-equilibrium, zero-pressure gradient). The development of wall models that specifically address shock impingement as well as pressure and thermophysical gradients, is sought.

REFERENCES

- ¹M. Holden, "Historical review of experimental studies and prediction methods to describe laminar and turbulent shock wave/boundary layer interactions in hypersonic flows," in *44th AIAA Aerospace Sciences Meeting and Exhibit* (2006) p. 494.
- ²M. Holden, "Experimental studies of separated flows at hypersonic speeds. II-Two-dimensional wedge separated flow studies." *AIAA Journal* **4**, 790–799 (1966).
- ³M. Holden, "Experimental studies of separated flows at hypersonic speeds. I-Separated flows over axisymmetric spiked bodies." *AIAA Journal* **4**, 591–599 (1966).
- ⁴M. Holden, "Theoretical and experimental studies of the shock wave-boundary layer interaction on compression surfaces in hypersonic flow," Tech. Rep. (Cornell Aeronautical Lab Inc Buffalo NY, 1970).
- ⁵M. Holden, "Shock wave-turbulent boundary layer interaction in hypersonic flow," Tech. Rep. ARL TR 75-0204 (Calspan Corporation, 1975).
- ⁶M. Holden, "Experimental studies of quasi-two-dimensional and three-dimensional viscous interaction regions induced by skewed-shock and swept-shock boundary layer interaction," Tech. Rep. 7018.A-2 (Calspan Advance Technology Center, 1984).
- ⁷M. Holden, A. Havener, and C. Lee, "Shock Wave/Turbulent Boundary Layer Interaction in High-Reynolds-Number Hypersonic Flows," Tech. Rep. (CALSPAN UB Research Center Buffalo NY, 1987).
- ⁸G. Settles and L. Dodson, "Supersonic and hypersonic shock/boundary-layer interaction database," *AIAA Journal* **32**, 1377–1383 (1994).
- ⁹M. Kussoy, L. Levy, and F. Menter, "Hypersonic flows as related to the national aerospace plane," Tech. Rep. NACA-CR-187985 (NASA, 1991).
- ¹⁰M. Kussoy, G. Huang, and F. Menter, "Hypersonic flows as related to the national aerospace plane," Tech. Rep. NACA-CR-199365 (NASA, 1995).
- ¹¹G. Settles and L. Dodson, "Hypersonic shock boundary-layer interaction database," Tech. Rep. NACA-CR-177577 (NASA, 1991).
- ¹²M. Holden, T. Wadhams, M. MacLean, and E. Mundy, "Experimental studies of shock wave/turbulent boundary layer interaction in high reynolds number supersonic and hypersonic flows to evaluate the performance of CFD codes," in *40th Fluid Dynamics Conference and Exhibit* (2010) p. 4468.
- ¹³M. Holden, T. Wadhams, and M. MacLean, "Measurements in regions of shock wave/turbulent boundary layer interaction from mach 4 to 10 for open and "blind" code evaluation/validation," in *21st AIAA Computational Fluid Dynamics Conference* (2013) p. 2836.
- ¹⁴M. Holden, T. Wadhams, M. MacLean, and A. DuFrene, "Measurements in regions of shock wave turbulent boundary layer interaction from Mach 3 to Mach 10 for Open and Blind Code Evaluation Validation," Tech. Rep. AFRL-OSR-VA-TR-2013-0134 (CUBRC, 2013).
- ¹⁵C. Running, T. Juliano, J. Jewell, M. Borg, and R. Kimmel, "Hypersonic shock-wave/boundary-layer interactions on a cone/flare," *Experimental Thermal and Fluid Science* **109**, 109911 (2019).
- ¹⁶J. Marvin, J. Brown, and P. Gnoffo, "Experimental database with baseline CFD solutions: 2-D and axisymmetric hypersonic shock-wave/turbulent-boundary-layer interactions," Tech. Rep. NASA TM-2013-216604 (NASA Ames, 2013).
- ¹⁷D. Knight and N. Kianvashrad, *Hypersonic Shock Wave Turbulent Boundary Layers - Direct Numerical Simulation, Large Eddy Simulation and Experiment* (Institute of Physics, Bristol, United Kingdom, 2023).
- ¹⁸J. Slotnick, A. Khodadoust, J. Alonso, D. Darmofal, W. Gropp, E. Lurie, and D. Mavriplis, "CFD vision 2030 study: a path to revolutionary computational aerosciences," Tech. Rep. (2014).
- ¹⁹S. Morton and R. Cummings, "CFD 2030: Hypersonic Modeling & Simulation Grand Challenge," in *AIAA SCITECH 2024 Forum* (2024) p. 0683.
- ²⁰D. Knight and G. Degrez, "Shock wave boundary layer interactions in high mach number flows a critical survey of current numerical prediction capabilities," AGARD Advisory Report Agard Ar **2**, 1–1 (1998).
- ²¹J. Moss and J. Olejniczak, "Shock-wave/boundary-layer interactions in hypersonic low density flows," in *7th AIAA/ASME Joint Thermophysics and Heat Transfer Conference* (1998) p. 2668.
- ²²P. Gnoffo, "Validation studies for hypersonic flow prediction," in *39th Aerospace Sciences Meeting and Exhibit* (2001) p. 1025.
- ²³I. Bedarev, A. Maslov, A. Sidorenko, N. Fedorova, and A. Shiplyuk, "Experimental and numerical study of a hypersonic separated flow in the vicinity of a cone-flare model," *Journal of Applied Mechanics and Technical Physics* **43**, 867–876 (2002).
- ²⁴G. Candler, I. Nompelis, M.-C. Druguet, M. Holden, T. Wadhams, I. Boyd, and W.-L. Wang, "CFD validation for hypersonic flight-Hypersonic double-cone flow simulations," in *40th AIAA Aerospace Sciences Meeting & Exhibit* (2002) p. 581.
- ²⁵C. Roy and F. Blottner, "Review and assessment of turbulence models for hypersonic flows," *Progress in Aerospace Sciences* **42**, 469–530 (2006).
- ²⁶D. Wilcox, "Formulation of the $k-\omega$ turbulence model revisited," *AIAA journal* **46**, 2823–2838 (2008).
- ²⁷M. Holden, J. Harvey, T. Wadhams, and M. MacLean, "A review of experimental studies with the double cone and hollow cylinder/flare configurations in the LENS hypervelocity tunnels and comparisons with Navier-Stokes and DSMC computations," in *48th AIAA Aerospace Sciences Meeting Including the New Horizons Forum and Aerospace Exposition* (2010) p. 1281.
- ²⁸D. Knight, J. Longo, D. Drikakis, D. Gaitonde, A. Lani, I. Nompelis, B. Reimann, and L. Walpot, "Assessment of CFD capability for prediction of hypersonic shock interactions," *Progress in Aerospace Sciences* **48**, 8–26 (2012).
- ²⁹G. Candler, "Next-generation CFD for hypersonic and aerothermal flows," in *22nd AIAA Computational Fluid Dynamics Conference* (2015) p. 3048.
- ³⁰D. Knight, O. Chazot, J. Austin, M. Badr, G. Candler, B. Celik, D. de Rosa, R. Donelli, J. Komives, A. Lani, et al., "Assessment of predictive capabilities for aerodynamic heating in hypersonic flow," *Progress in Aerospace Sciences* **90**, 39–53 (2017).
- ³¹N. Kianvashrad and D. Knight, "Simulation of hypersonic shock wave-laminar boundary layer interactions," *Progress in Flight Physics—Volume 9* **9**, 409–420 (2017).
- ³²N. Kianvashrad and D. Knight, "Simulation of hypersonic shock-wave-laminar-boundary-layer interaction on hollow cylinder flare," *AIAA journal* **55**, 322–326 (2017).
- ³³R. Alviani, *Assessment of Wilcox $k-\omega$ turbulence model in regions of shock-wave turbulent boundary-layer interaction*, Master's thesis, Rutgers The State University of New Jersey, School of Graduate Studies (2018).
- ³⁴G. Shoev, G. Oblapenko, O. Kunova, M. Mekhonoshina, and E. Kustova, "Validation of vibration-dissociation coupling models in hypersonic non-equilibrium separated flows," *Acta Astronautica* **144**, 147–159 (2018).
- ³⁵P. Cross and M. West, "Simulation of hypersonic flowfields using starccm+," Tech. Rep. (Naval Air Warfare Center Weapons Division, 2019).
- ³⁶A. Kennedy, R. T. Penty G, C. James, M. Thompson, R. Morgan, J. M. Austin, F. Zander, and M. McGilvray, "Measurements of hypersonic double cone flows with shock wave/boundary layer interactions in the X3 expansion tunnel," in *AIAA SCITECH 2023 Forum* (2023) p. 0271.
- ³⁷S. Tissera, D. Drikakis, and T. Birch, "Computational fluid dynamics methods for hypersonic flow around blunted-cone-cylinder-flare," *Journal of Spacecraft and Rockets* **47**, 563–570 (2010).
- ³⁸S. Tissera, V. Titarev, and D. Drikakis, "Chemically reacting flows around a double-cone, including ablation effects," in *48th AIAA Aerospace Sciences Meeting Including the New Horizons Forum and Aerospace Exposition* (2010).
- ³⁹D. Knight, N. Kianvashrad, and M. Youssefi, "Simulation of hypersonic shock wave laminar boundary layer interactions," in *11th Ankara International Aerospace Conference* (2021).
- ⁴⁰D. Knight, H. Yan, A. Panaras, and A. Zheltovodov, "RTO WG 10-CFD validation for shock wave turbulent boundary layer interactions," in *40th AIAA Aerospace Sciences Meeting and Exhibit* (2002) p. 437.
- ⁴¹R. Alviani, *Assessment of Wilcox $k-\omega$ Turbulence Model in Regions of Shock Wave Turbulent Boundary Layer Interaction*, Master's thesis, Rutgers The State University of New Jersey, New Brunswick, NJ (2018).
- ⁴²The half-cone angle for shock detachment at Mach 5 is 54.5°.
- ⁴³C. Horstman, "Hypersonic shock-wave turbulent-boundary-layer interaction flows-experiment and computation," in *22nd Fluid Dynamics, Plasma Dynamics and Lasers Conference* (1991) p. 1760.
- ⁴⁴M. Wright, G. Candler, and D. Bose, "Data-parallel line relaxation method for the Navier-Stokes equations," *AIAA Journal* **36**, 1603–1609 (1998).
- ⁴⁵M. Wright, T. White, and N. Mangini, "Data Parallel Line Relaxation (DPLR) Code User Manual: Acadia-Version 4.01. 1," Tech. Rep. (2009).
- ⁴⁶F. Menter, "Two-equation eddy-viscosity turbulence models for engineer-

- ing applications,” AIAA Journal **32**, 1598–1605 (1994).
- ⁴⁷D. Wilcox, *Turbulence Modeling for CFD, 3rd edition* (DCW Industries, 2006).
- ⁴⁸A. Mazaheri, P. Gnoffo, C. Johnston, and B. Kleb, “LAURA Users Manual: 5.3-48528,” Tech. Rep. (NASA, 2010).
- ⁴⁹P. Gnoffo, “An upwind-biased, point-implicit relaxation algorithm for viscous, compressible perfect-gas flows,” Tech. Rep. (1990).
- ⁵⁰P. Gnoffo, S. Berry, and J. Van Norman, “Uncertainty assessments of 2d and axisymmetric hypersonic shock wave-turbulent boundary layer interaction simulations at compression corners,” in *42nd AIAA Thermophysics Conference* (2011) p. 3142.
- ⁵¹N. Georgiadis and D. Yoder, “Recalibration of the shear stress transport model to improve calculation of shock separated flows,” in *51st AIAA Aerospace Sciences Meeting Including the New Horizons Forum and Aerospace Exposition* (2013) p. 685.
- ⁵²P. Spalart, “Strategies for turbulence modelling and simulations,” International Journal of Heat and Fluid Flow **21**, 252–263 (2000).
- ⁵³M. Holden, “Experimental research and analysis in supersonic and hyper-velocity flows in the LENS shock tunnels and expansion tunnel,” in *20th AIAA International Space Planes and Hypersonic Systems and Technologies conference* (2015) p. 3660.
- ⁵⁴T. Wadhams, M. Holden, and M. MacLean, “Comparison of experimental and computational results from blind turbulent shock wave interaction study over cone flare and hollow cylinder flare configuration,” AIAA Aviation, Atlanta, GA (2014).
- ⁵⁵S. Roy and K. Sinha, “Variable turbulent Prandtl number model applied to hypersonic shock/boundary-layer interactions,” in *2018 Fluid Dynamics Conference* (2018) p. 3728.
- ⁵⁶S. Roy and K. Sinha, “Turbulent heat flux model for hypersonic shock-boundary layer interaction,” AIAA Journal **57**, 3624–3629 (2019).
- ⁵⁷K. Sinha, K. Mahesh, and G. Candler, “Modeling shock unsteadiness in shock/turbulence interaction,” Physics of fluids **15**, 2290–2297 (2003).
- ⁵⁸K. Sinha, K. Mahesh, and G. Candler, “Modeling the effect of shock unsteadiness in shock/turbulent boundary-layer interactions,” AIAA journal **43**, 586–594 (2005).
- ⁵⁹D. Prabhu, “Shock Wave Interactions: A CFD Study of CUBRC LENS-II Turbulent Experiments,” in *AIAA Aviation and Aeronautics Forum and Exposition*, ARC-E-DAA-TN15585 (2014).
- ⁶⁰A. Ali Pasha, K. Juhany, and M. Khalid, “Numerical prediction of shock/boundary-layer interactions at high Mach numbers using a modified Spalart–Allmaras model,” Engineering Applications of Computational Fluid Mechanics **12**, 459–472 (2018).
- ⁶¹D. Knight, H. Yan, A. Panaras, and A. Zheltovodov, “Advances in CFD prediction of shock wave turbulent boundary layer interactions,” Progress in Aerospace Sciences **39**, 121–184 (2003).
- ⁶²W. Chan, P. Jacobs, and D. Mee, “Suitability of the $k - \omega$ turbulence model for scramjet flowfield simulations,” International Journal for Numerical Methods in Fluids **70**, 493–514 (2012).
- ⁶³H. Zhang, T. Craft, and H. Iacovides, “The formulation of the RANS equations for supersonic and hypersonic turbulent flows,” The Aeronautical Journal **125**, 525–555 (2021).
- ⁶⁴P. Raje and K. Sinha, “Anisotropic SST turbulence model for shock-boundary layer interaction,” Computers & Fluids **228**, 105072 (2021).
- ⁶⁵A. Wagner, J. Schramm, K. Hannemann, R. Whitside, and J. Hickey, “Hypersonic Shock Wave Boundary Layer Interaction Studies on a Flat Plate at Elevated Surface Temperature,” in *Shock Wave Interactions*, edited by K. Kontis (Springer International Publishing, Cham, 2018) pp. 231–243.
- ⁶⁶C. Prasad and D. Gaitonde, “Turbulence modeling of 3D high-speed flows with upstream-informed corrections,” Shock Waves **33**, 99–115 (2023).
- ⁶⁷X. Xiao, H. Hassan, J. Edwards, and R. Gaffney, “Role of Turbulent Prandtl Numbers on Heat Flux at Hypersonic Mach Numbers,” AIAA Journal **45**, 806–813 (2007).
- ⁶⁸S. Roy, U. Pathak, and K. Sinha, “Variable turbulent prandtl number model for shock/boundary-layer interaction,” AIAA Journal **56**, 342–355 (2018).
- ⁶⁹T. Coakley and P. Huang, “Turbulence modeling for high speed flows,” in *30th Aerospace Sciences Meeting and Exhibit* (1992) p. 436.
- ⁷⁰C. Rumsey, “Compressibility considerations for kw turbulence models in hypersonic boundary-layer applications,” Journal of Spacecraft and Rockets **47**, 11–20 (2010).
- ⁷¹G. Tu, X. Deng, and M. Mao, “Assessment of two turbulence models and some compressibility corrections for hypersonic compression corners by high-order difference schemes,” Chinese Journal of Aeronautics **25**, 25–32 (2012).
- ⁷²T. Coakley, C. Horstman, J. Marvin, J. Viegas, J. Bardina, P. Huang, and M. Kussoy, “Turbulence compressibility corrections,” Tech. Rep. (1994).
- ⁷³J. Hoste, “Assessment of scale resolving turbulence models in the TAU code for canonical shock-turbulence interaction,” Tech. Rep. DLR-FB-2020-28. 169 S (DLR, 2023).
- ⁷⁴F. Menter, M. Kuntz, and R. Langtry, “Ten years of industrial experience with the SST turbulence model,” Turbulence, heat and mass transfer **4**, 625–632 (2003).
- ⁷⁵R. Baurle, “Modeling of high speed reacting flows: established practices and future challenges,” in *42nd AIAA Aerospace Sciences Meeting and Exhibit* (2004) p. 267.
- ⁷⁶F. Génin and S. Menon, “Studies of shock/turbulent shear layer interaction using large-eddy simulation,” Computers and Fluids **39**, 800–819 (2010).
- ⁷⁷R. Quadros, K. Sinha, and J. Larsson, “Turbulent energy flux generated by shock/homogeneous-turbulence interaction,” Journal of Fluid Mechanics **796**, 113–157 (2016).
- ⁷⁸A. Pasha and K. Juhany, “Numerical simulation of compression corner flows at Mach number 9,” Chinese Journal of Aeronautics **33**, 1611–1624 (2020).
- ⁷⁹J. Vemula and K. Sinha, “Reynolds stress models applied to canonical shock-turbulence interaction,” Journal of Turbulence **18**, 653–687 (2017).
- ⁸⁰S. Karl, J. Hickey, and F. Lacombe, “Reynolds stress models for shock-turbulence interaction,” in *31st International Symposium on Shock Waves 1: Fundamentals 31* (Springer, 2019) pp. 511–517.
- ⁸¹J. Vemula and K. Sinha, “Explicit algebraic reynolds stress model for shock-dominated flows,” International Journal of Heat and Fluid Flow **85**, 108680 (2020).
- ⁸²G. Gerolymos, E. Sauret, and I. Vallet, “Oblique-shock-wave/boundary-layer interaction using near-wall reynolds-stress models,” AIAA journal **42**, 1089–1100 (2004).
- ⁸³J. Slater, “WIND-US simulations of the nasa 1507 inlet test case,” in *AIAA SCITECH 2024 Forum* (2024) p. 0981.
- ⁸⁴Siemens Digital Industries Software, “Simcenter STAR-CCM+, version 2210,” <https://www.plm.automation.siemens.com/global/en/products/simcenter/STAR-CCM.html> (Siemens 2022).
- ⁸⁵P. Spalart and C. Rumsey, “Effective inflow conditions for turbulence models in aerodynamic calculations,” AIAA journal **45**, 2544–2553 (2007).
- ⁸⁶P. Durbin, “On the $k - \epsilon$ stagnation point anomaly,” International Journal of Heat and Fluid Flow **17**, 89–90 (1996).
- ⁸⁷“Turbulence Modeling Resource,” <https://turbmodels.larc.nasa.gov/sst.html>, accessed: 2024-08-10, Last Updated: 2023-09-10 by Christopher Rumsey.
- ⁸⁸N. Gibbons, K. Damm, P. Jacobs, and R. Gollan, “Eilmr: An open-source multi-physics hypersonic flow solver,” Computer Physics Communications **282** (2023), doi.org/10.1016/j.cpc.2022.108551.
- ⁸⁹J. dwards, “A low-diffusion flux-splitting scheme for Navier-Stokes calculations,” Computers and Fluids **26**, 635–658 (1997).
- ⁹⁰K. Damm, N. Gibbons, and R. Gollan, “Application of a Jacobian-Free Newton-Krylov Method to the Simulation of Hypersonic Flows,” in *AIAA SCITECH 2023 Forum*, 2023-2295 (National Harbor, MD & Online, 2023).
- ⁹¹B. McBride, M. Zehe, and S. Gordon, “NASA Glenn Coefficients for Calculating Thermodynamic Properties of Individual Species,” Tech. Rep. 211556 (National Aeronautics and Space Administration, 2002).
- ⁹²S. Langer, A. Schwöppe, and N. Kroll, “The dlr flow solver tau - status and recent algorithmic developments,” (2014), 10.2514/6.2014-0080.
- ⁹³D. Schwamborn, T. Gerhold, and R. Heinrich, “The dlr tau-code: recent applications in research and industry,” in *ECCOMAS CFD 2006: Proceedings of the European Conference on Computational Fluid Dynamics, Egmond aan Zee, The Netherlands, September 5–8, 2006* (Delft University of Technology; European Community on Computational Methods, 2006).
- ⁹⁴D. Schwamborn, T. Gerhold, and V. Hannemann, “On the validation of the dlr-tau code,” in *New Results in Numerical and Experimental Fluid Mechanics II: Contributions to the 11th AG STAB/DGLR Symposium Berlin, Germany 1998*, edited by W. Nitsche, H.-J. Heinemann, and R. Hilbig (Vieweg+Teubner Verlag, Wiesbaden, 1999) pp. 426–433.

- ⁹⁵L. Cambier and N. Kroll, "Miracle – a joint dlr/onera effort on harmonization and development of industrial and research aerodynamic computational environment," *Aerospace Science and Technology* **12**, 555–566 (2008).
- ⁹⁶T. Knopp, "Validation of the turbulence models in the dlr tau code for transonic flows. a best practice guide," (2006).
- ⁹⁷A. Mack and V. Hannemann, "Validation of the unstructured dlr-tau-code for hypersonic flows," in *32nd AIAA Fluid Dynamics Conference and Exhibit*, <https://arc.aiaa.org/doi/pdf/10.2514/6.2002-3111>.
- ⁹⁸Y. Wada and M.-S. Liou, "An accurate and robust flux splitting scheme for shock and contact discontinuities," *SIAM Journal on Scientific Computing* **18**, 633–657 (1997), <https://doi.org/10.1137/S1064827595287626>.
- ⁹⁹B. van Leer, "Towards the ultimate conservative difference scheme. v. a second-order sequel to godunov's method," *Journal of Computational Physics* **32**, 101–136 (1979).
- ¹⁰⁰T. Horchler, S. Fechter, and K. Hannemann, "Validation of the dlr tau code for scale-resolving combustion simulations," in *Space Propulsion 2018* (2018).
- ¹⁰¹V. Hannemann, "Numerical simulation of shock-shock-interactions considering chemical and thermal nonequilibrium," in *DLR-Forschungsbericht 97-07* (1997).
- ¹⁰²B. Thornber, A. Mosedale, D. Drikakis, D. Youngs, and R. Williams, "An improved reconstruction method for compressible flows with low Mach number features," *Journal of Computational Physics* **227**, 4873–4894 (2008).
- ¹⁰³S. Wallin and A. Johansson, "An explicit algebraic reynolds stress model for incompressible and compressible turbulent flows," *Journal of Fluid Mechanics* **403**, 89–132 (2000).
- ¹⁰⁴J. C. Kok, "Resolving the dependence on freestream values for the k-turbulence model," *AIAA journal* **38**, 1292–1295 (2000).
- ¹⁰⁵A. Hellsten, "New advanced k-w turbulence model for high-lift aerodynamics," *AIAA Journal* **43**, 1857–1869 (2005), <https://doi.org/10.2514/1.13754>.
- ¹⁰⁶T. Knopp, N. Reuther, M. Novara, D. Schanz, E. Schülein, A. Schröder, and C. J. Kähler, "Modification of the SSG/LRR-Omega model for turbulent boundary layer flows in an adverse pressure gradient," *Flow, Turbulence and Combustion* **111**, 409–423 (2023).
- ¹⁰⁷I. Huismann, S. Fechter, and T. Leicht, "HyperCODA—Extension of Flow Solver CODA to Hypersonic Flows," *HyperCODA—Extension of Flow Solver CODA Towards Hypersonic Flows* **13** (2020).
- ¹⁰⁸I. Huismann, S. Fechter, and T. Leicht, "HyperCODA—extension of flow solver CODA towards hypersonic flows," in *New Results in Numerical and Experimental Fluid Mechanics XIII: Contributions to the 22nd STAB/DGLR Symposium* (Springer, 2021) pp. 99–109.
- ¹⁰⁹S. Fechter and I. Huismann, "HyperCODA – Extension of Flow Solver CODA Towards Rocket Flows," in *2022 9th European Conference for Aerospace Sciences (EUCASS)* (2022).
- ¹¹⁰S. Görtz, T. Leicht, V. Couaillier, M. Méheut, P. Larrieu, and S. Champagnoux, "CODA: A european perspective for a next-generation CFD, analysis and design platform," (2022).
- ¹¹¹S. Allmaras and F. Johnson, "Modifications and clarifications for the implementation of the Spalart-Allmaras turbulence model," in *Seventh international conference on computational fluid dynamics (ICCFD7)*, Vol. 1902 (Big Island, HI, 2012).
- ¹¹²S. Chen, F. Cai, H. Xue, N. Wang, and C. Yan, "An improved AUSM-family scheme with robustness and accuracy for all mach number flows," *Applied Mathematical Modelling* **77**, 1065–1081 (2020).
- ¹¹³Aerosoft Inc., "Gaspex," https://www.aerosoftinc.com/gasp_main.php (2018).
- ¹¹⁴B. Mallol, M. Boogaard, N. Delsate, and C. Hirsch, "New meshing methods for ship propellers and hydrofoils," in *24th Numerical Towing Tank Symposium Proceedings* (2022) pp. 77–82.
- ¹¹⁵S. Monté, L. Temmerman, B. Tartinville, B. Léonard, and C. Hirsch, "Towards a Separation Sensitive Explicit Algebraic Reynolds Stress RANS Model," in *Ercofac Bulletin 121* (ERCOFTAC, 2019) pp. 61–66.
- ¹¹⁶V. Driest, "The Problem of Aerodynamic Heating," in *Aerodynamic Heating: Aerodynamic Aspects Session Proceedings* (1956) pp. 26–41.
- ¹¹⁷E. Lemmon, R. Jacobsen, S. Penoncello, and D. Friend, "Thermodynamic Properties of Air and Mixtures of Nitrogen, Argon, and Oxygen From 60 to 2000 K at Pressures to 2000 MPa," *Journal of Physical and Chemical Reference Data* **29**, 331–385 (2000).
- ¹¹⁸R. Gupta, K.-P. Lee, R. Thompson, and J. Yos, "Calculations and curve fits of thermodynamic and transport properties for equilibrium air to 30000 k," Tech. Rep. (NASA Langley Research Center, 1991).
- ¹¹⁹Y. Li, F. Ries, W. Leudesdorff, K. Nishad, A. Pati, C. Hasse, J. Janicka, S. Jakirlić, and A. Sadiki, "Non-equilibrium wall functions for large eddy simulations of complex turbulent flows and heat transfer," *International Journal of Heat and Fluid Flow* **88**, 108758 (2021).
- ¹²⁰J. Hoste, T. Ecker, C. Amato, N. Gibbons, D. Knight, F. Hizir, T. Köktürk, A. Sattarov, O. Thiry, J. Hickey, S. Qiang, J. Coder, N. Castelino, and V. Viti, "A code-to-code comparison of turbulent hypersonic sharp cone-flares," in *HiSST 2024, 3rd International Conference on High-Speed Vehicle Science and Technology* (2024).
- ¹²¹T. Economou, F. Palacios, S. Copeland, T. Lukaczyk, and J. Alonso, "SU2: An Open-Source Suite for Multiphysics Simulation and Design," *AIAA Journal* **54**, 828–846 (2016), <https://doi.org/10.2514/1.J053813>.
- ¹²²W. Maier, J. Needels, C. Garbacz, F. Morgado, J. Alonso, and M. Fossati, "SU2-NEMO: An Open-Source Framework for High-Mach Nonequilibrium Multi-Species Flows," *Aerospace* **8** (2021), 10.3390/aerospace8070193.
- ¹²³L. Eça, M. Hoekstra, A. Hay, and D. Pelletier, "A manufactured solution for a two-dimensional steady wall-bounded incompressible turbulent flow," *International Journal of Computational Fluid Dynamics* **21**, 175–188 (2007).
- ¹²⁴B. Aupoix and P. Spalart, "Extensions of the Spalart-Allmaras turbulence model to account for wall roughness," *International Journal of Heat and Fluid Flow* **24**, 454–462 (2003).
- ¹²⁵P. Spalart, "A One-Equation Turbulence Model for Aerodynamic Flows," (1992), 10.2514/6.1992-439.
- ¹²⁶P. Gnozzo, R. Gupta, and J. Shinn, "Conservation equations and physical models for hypersonic air flows in thermal and chemical nonequilibrium," Tech. Rep. NASA TP 2867 (NASA, 1989).
- ¹²⁷L. Scalabrin, *Numerical simulation of weakly ionized hypersonic flow over reentry capsules*, Ph.D. thesis, University of Michigan, Ann Arbor, Michigan (2007).
- ¹²⁸S. Kim, S. Mathur, J. Murthy, and D. Choudhury, "A Reynolds-averaged Navier-Stokes solver using unstructured mesh-based finite-volume scheme," in *36th AIAA Aerospace Sciences Meeting and Exhibit* (1998) p. 231.
- ¹²⁹S. Kim and B. Makarov, "An implicit fractional-step method for efficient transient simulation of incompressible flows," in *17th AIAA Computational Fluid Dynamics Conference* (2005) p. 5253.
- ¹³⁰J. Weiss, J. Maruszewski, and W. Smith, "Implicit solution of preconditioned navier-stokes equations using algebraic multigrid," *AIAA Journal* **37**, 29–36 (1999).
- ¹³¹J. Weiss and W. Smith, "Preconditioning applied to variable and constant density flows," *AIAA Journal* **33**, 2050–2057 (1995).
- ¹³²F. Menter, A. Matyushenko, and R. Lechner, in *New Results in Numerical and Experimental Fluid Mechanics XII: Contributions to the 21st STAB/DGLR Symposium, Darmstadt, Germany*, 2018.
- ¹³³T. Pulliam and J. Steger, "Implicit Finite-Difference Simulations of Three-Dimensional Compressible Flow," *AIAA Journal* **18**, 159–167 (1980), <https://doi.org/10.2514/3.50745>.
- ¹³⁴William M. Chan, Shishir A. Pandya, Stuart E. Rogers, James C. Henson, Henry C. Lee, David L. Kao, Pieter G. Buning, Robert L. Meakin, David A. Boger, Steven M. Nash, *Chimera Grid Tools User's Manual*, National Aeronautics and Space Administration, available at <https://www.nasa.gov/publications/software/docs/chimera/index.html>.
- ¹³⁵R. Tramel, R. Nichols, and P. Buning, "Addition of improved shock-capturing schemes to overflow 2.1," (19th AIAA Computational Fluid Dynamics, 2009) <https://arc.aiaa.org/doi/pdf/10.2514/6.2009-3988>.
- ¹³⁶S. Yoon, *An LU-SSOR scheme for the Euler and Navier-Stokes equations* (American Institute of Aeronautics and Astronautics, 1986).
- ¹³⁷"POINTWISE," www.pointwise.com (2024).
- ¹³⁸Lau, K. Y., "Hypersonic Boundary-Layer Transition: Application to High-Speed Vehicle Design," *Journal of Spacecraft and Rockets* **45**, 176–183 (2008).
- ¹³⁹Kara, K., Balakumar, P., and Kandil, O. A., "Effects of Nose Bluntness on Hypersonic Boundary-Layer Receptivity and Stability over Cones," *AIAA Journal* **49**, 2593–2606 (2012).

- ¹⁴⁰Edwards, J. R. and Liou, M.-S., “Low Diffusion Flux-Splitting Methods for Flows at all Speeds,” *AIAA Journal* **36**, 1610–1617 (1998).
- ¹⁴¹Venkatakrishnan, V., “Convergence to Steady-State Solutions of the Euler Equations on Unstructured Grids with Limiters,” *Journal of Computational Physics* **118**, 120–130 (1995).
- ¹⁴²S. Cao, J. Hao, I. Klioutchnikov, H. Olivier, K. A. Heufer, and C.-Y. Wen,

- “Leading-edge bluntness effects on hypersonic three-dimensional flows over a compression ramp,” *Journal of Fluid Mechanics* **923**, A27 (2021).
- ¹⁴³C. Rumsey, D. Allison, T. Biedron, P. Buning, T. Gainer, J. Morrison, M. Rivers, S. Mysko, and D. Witkowski, “CFD sensitivity analysis of a modern civil transport near buffet-onset conditions,” Tech. Rep. (NASA Langley Research Center, 2001).